



# Toward a Comprehensive Grid of Cepheid Models with MESA. I. Uncertainties of the Evolutionary Tracks of Intermediate-mass Stars

O. Ziółkowska<sup>1</sup> , R. Smolec<sup>1</sup> , A. Thoul<sup>2</sup> , E. Farrell<sup>3</sup>, R. Singh Rathour<sup>1</sup> , and V. Hodge<sup>1</sup>

<sup>1</sup> Nicolaus Copernicus Astronomical Centre, Polish Academy of Sciences, Bartycka 18, 00-716 Warszawa, Poland; [oliwiakz@camk.edu.pl](mailto:oliwiakz@camk.edu.pl)

<sup>2</sup> Space sciences, Technologies and Astrophysics Research (STAR) Institute, Université de Liège, Allée du 6 Août 19C, Bat. B5C, B-4000 Liège, Belgium

<sup>3</sup> Department of Astronomy, University of Geneva, Chemin Pegasi 51, 1290 Versoix, Switzerland

Received 2024 April 24; revised 2024 July 5; accepted 2024 July 8; published 2024 September 23

## Abstract

Helium-burning stars, in particular Cepheids, are especially difficult to model, as the choice of free parameters can greatly impact the shape of the blue loops—the part of the evolutionary track at which the instability strip is crossed. Contemporary one-dimensional stellar evolution codes, like Modules for Experiments in Stellar Astrophysics (MESA), come with a large number of free parameters that allow us to model the physical processes in stellar interiors under many assumptions. The uncertainties that arise from this freedom are rarely discussed in the literature despite their impact on the evolution of the model. We calculate a grid of evolutionary models with MESA, varying several controls, like solar mixture of heavy elements, mixing-length theory prescription, nuclear reaction rates, the scheme to determine convective boundaries, atmosphere model, and temporal and spatial resolution, and quantify their impact on age and location of the evolutionary track on the H-R diagram from the main sequence until the end of core helium burning. Our investigation was conducted for a full range of masses and metallicities expected for classical Cepheids. The uncertainties are significant, especially during core helium burning, reaching or exceeding the observational uncertainties of  $\log T_{\text{eff}}$  and  $\log L$  for detached eclipsing binary systems. For  $\geq 9 M_{\odot}$  models, thin convective shells develop and evolve erratically, not allowing the models to converge. A careful inspection of Kippenhahn diagrams and convergence study is advised for a given mass and metallicity, to assess how severe this problem is and to what extent it may affect the evolution.

*Unified Astronomy Thesaurus concepts:* Cepheid variable stars (218); Stellar evolutionary models (2046); Stellar evolution (1599); Stellar evolutionary tracks (1600); Blue loop (167)

## 1. Introduction

Stellar evolution modeling is the backbone of modern stellar astrophysics. Given the input parameters, primarily mass and metal content, stellar evolution tools predict the evolution of the model on the Hertzsprung–Russell (H-R) diagram, providing insight into the internal structure of the model at any time during evolution. This, in turn, can be confronted and tested with various observational constraints, e.g., asteroseismic inferences (e.g., Kervella et al. 2004; Daszyńska-Daszkiewicz et al. 2023b; Sánchez Arias et al. 2023), including Cepheid pulsations (e.g., Moskalik & Dziembowski 2005; Bono et al. 2006), observations of eclipsing binaries (e.g., Stassun et al. 2009; Southworth 2015; Higl & Weiss 2017), or data on stellar clusters (e.g., Renzini & Fusi Pecci 1988; Schaller et al. 1992).

The currently available stellar evolution tools, which allow us to trace all evolutionary phases, from pre-main sequence until depletion of available nuclear reservoirs, are one-dimensional. This imposes the use of a series of simplifying models and assumptions to describe the complex processes taking place inside stars, such as convection, rotation, or internal transport processes. A well-known example is the mixing-length theory (MLT; Böhm-Vitense 1958) used to describe the stratification of convective layers of the model. The description of material properties, such as nuclear reaction rates, opacity, and equation of state (EOS), is an active and dynamic area of research, leaving

several options for stellar evolution tools (e.g., Morel et al. 2010; Xu et al. 2013; Colgan et al. 2016; Jermyn et al. 2021). Due to the models used and the tables of material properties, each evolution code contains dozens of options and parameters. Many of these are free parameters, for which there are no strong theoretical constraints. Similarly, it is sometimes difficult to identify the best option among many possible ones, e.g., for the source of nuclear reaction rates used or a variant of the MLT. In addition, each evolutionary code contains tens of parameters that control the numerical solution, the precision of the solvers, the way in which tables of material properties are interpolated, and spatial and temporal resolution of the models. All these *secondary* parameters and choices may affect the evolutionary path in the H-R diagram, some to a negligible degree, while others may lead to qualitatively different paths.

A common practice used in evolutionary modeling is to explore the effects of a few key *primary* parameters on the evolution of a star. In addition to mass and metallicity, these could be the helium content, mass-loss rate, rotation rate, or the extent of convective overshooting; see, e.g., BaSTI (Pietrinferni et al. 2021), DSEP (Dotter et al. 2008), Victoria-Regina (VandenBerg et al. 2014), Yale-Potsdam (Spada et al. 2017), PARSEC (Bressan et al. 2012), or MIST (Choi et al. 2016). While the numerical parameters are usually chosen to ensure convergence of the models, the choice of some secondary parameters, such as the MLT version, the choice of solar composition, and the choice of atmospheric model, is usually fixed and sometimes depends on authors' preference.

In this work, we follow a similar approach. First, we select and justify the choice of parameters for a reference. However, we assume that we could have made a different choice for



Original content from this work may be used under the terms of the [Creative Commons Attribution 4.0 licence](https://creativecommons.org/licenses/by/4.0/). Any further distribution of this work must maintain attribution to the author(s) and the title of the work, journal citation and DOI.

many of the secondary parameters, which could have led to a slightly different evolutionary path. By considering, for a given mass and metallicity, a grid of models with different choices of secondary parameter values, we obtain a family of paths in the H-R diagram. On this basis, for the established characteristic, benchmark points on the evolutionary track, we determine the uncertainty of the track.

In this study we use a publicly available, one-dimensional, open-source stellar evolution code, Modules for Experiments in Stellar Astrophysics (MESA; Paxton et al. 2011, 2013, 2015, 2018, 2019; Jermyn et al. 2023). It offers the user tens of choices for the abovementioned secondary options and allows us to fully control numerical aspects of the solution. In particular, we will examine the impact of the following aspects of stellar evolution modeling: variant of the atmospheric boundary condition, different relative distributions of heavy elements (solar mixtures), method of interpolation in the opacity tables, variant of the MLT theory, scheme to determine the convective boundaries, different nets of nuclear reactions and different rates of specific reactions, atomic diffusion, and spatial and temporal resolution of the model. We investigated two cases: without convective core overshooting and with moderate overshooting from the hydrogen-burning convective core. Rotation and mass loss are neglected in this study. These effects will be investigated in the forthcoming paper R. Smolec et al. (2024, in preparation). The effects of the input model parameters on the elemental abundances will be presented in O. Ziółkowska et al. (2024, in preparation). A limited sample of evolutionary tracks for Cepheids with MESA have been published by, e.g., Espinoza-Arancibia et al. (2022) and Guzik et al. (2021), but lacking the detailed discussion of the uncertainties.

We focus our attention on intermediate-mass stars,  $2\text{--}15 M_{\odot}$ , and a moderate range of metallicities, from low to solar ( $[\text{Fe}/\text{H}] = -1.0, -0.5, 0.0$ ), which covers the extent of classical Cepheids' parameters. This choice is motivated by our further goals. This is the first paper in a series in which we plan to address several problems related to Cepheid modeling. These intermediate-mass stars develop radial pulsations as they cross the classical instability strip (IS; see, e.g., Sandage & Tamman 1969; Catelan & Smith 2015). This happens either during a short-lived transition toward the red giant branch (RGB; first crossing of the IS) or during a core helium-burning (CHeB) phase, while an evolutionary track performs a blue loop in the H-R diagram (second and third crossings). Evolutionary calculations predict masses of classical Cepheids that are too high as compared to pulsation theory predictions and observations (e.g., Stobie 1969; Wood et al. 1997; Bono et al. 2002; Caputo et al. 2005; Keller & Wood 2006; Natale et al. 2008; Pietrzyński et al. 2010; Neilson & Blinn 2021). This is one of the most severe problems in the modeling of classical Cepheids. While we will address this problem in forthcoming publications, in this study our goal is to provide a foundation for evolutionary calculations, in particular, to estimate how various secondary choices and parameters affect evolutionary tracks in the H-R diagram.

The structure of the paper is the following. In Section 2 we describe evolutionary calculations and their ingredients, in particular for the reference model. We also explain how the computed models are compared. Results are presented in Section 3 with the division into low- and high-mass models. A discussion, in which we provide our estimate for the

**Table 1**  
Adopted Mass Fractions,  $X$ ,  $Y$ , and  $Z$ , and Metallicity,  $[\text{Fe}/\text{H}]$ , of the Models for Three Different Solar Abundance Mixtures, **A09**, **GS98**, and **GN93**

$X$	$Y$	$Z$	$[\text{Fe}/\text{H}]$
<b>A09; <math>(Z/X)_{\odot} = 0.0181</math></b>			
0.7165	0.2695	0.0140	0.033
0.7415	0.2545	0.0040	−0.526
0.7480	0.2506	0.0014	−0.985
<b>GS98; <math>(Z/X)_{\odot} = 0.0231</math></b>			
0.70742	0.27495	0.01763	0.033
0.73880	0.25612	0.00508	−0.526
0.74703	0.25118	0.00179	−0.985
<b>GN93; <math>(Z/X)_{\odot} = 0.0244</math></b>			
0.70510	0.27634	0.01856	0.033
0.73809	0.25655	0.00536	−0.526
0.74678	0.25133	0.00189	−0.985

uncertainty on evolutionary tracks, is presented in Section 4, and we conclude in Section 5.

## 2. Methods

### 2.1. Evolutionary Calculations

We use MESA (Paxton et al. 2011, 2013, 2015, 2018, 2019; Jermyn et al. 2023), version r21.12.1. Masses of our models span from  $2$  to  $15 M_{\odot}$ , with a step of  $1 M_{\odot}$ , with three different metallicities corresponding roughly to  $[\text{Fe}/\text{H}] = 0, -0.5$ , and  $-1.0$  (exact values are collected in Table 1). Evolutionary phases, from zero-age main sequence (ZAMS) until the end of CHeB, are calculated. Mass loss and rotation are neglected.

In the reference model we do not consider convective core overshooting, although we discuss its effects in Section 3.2.

### 2.2. Reference Model—Adopted Physics

Here we describe the choice of adopted physics of the reference model, as well as the varied options. For the complete inlist (input parameter file for MESA) of the reference model we refer the reader to Appendix A.

#### 2.2.1. Opacities and Scaled Solar Abundance

Opacity is given in a tabular form for a wide range of temperatures and densities ( $T, \rho$ ) and for different chemical mixtures and different hydrogen,  $X$ , and metal,  $Z$ , mass fractions. In MESA's `kap` module, opacity is interpolated between tables calculated for different  $X$  and  $Z$  with either linear or cubic interpolation in  $X/Z$ . We choose cubic interpolation in the reference model, and we investigate linear interpolation as an option. The set of models adopting different opacity interpolation schemes is referred to in the following as INT (see Table 2).

In this work, we use OPAL opacity tables (Iglesias & Rogers 1993, 1996), supplemented with opacity tables from Ferguson et al. (2005) at lower temperatures. Type 2 opacity tables take into account enhanced C and O abundances during and after CHeB. Opacity tables are calculated assuming the abundance of specific metals corresponding to solar composition, scaled to a given total mass fraction of metals,  $Z$ . The basis for calculating the solar-scaled abundances is the work of

**Table 2**

Characteristics of Various Sets of Models Considered in This Paper: INT, MIX, DIFF, NET, ATM, MLT, CONV, and RES

Set	Varied Options
<b>INT_A</b>	cubic $X/Z$ interpolation of opacity tables
INT_B	linear $X/Z$ interpolation of opacity tables
<b>MIX_A</b>	scaled solar mixture based on Asplund et al. (2009)
MIX_B	scaled solar mixture based on Grevesse & Sauval (1998)
MIX_C	scaled solar mixture based on Grevesse & Noels (1993)
<b>DIFF_A</b>	atomic diffusion neglected
DIFF_B	atomic diffusion included
<b>NET_A</b>	$^{12}\text{C}(\alpha, \gamma)^{16}\text{O}$ from Kunz et al. (2002) + $^{14}\text{N}(\alpha, \gamma)^{15}\text{O}$ from Cyburt et al. (2010) + pp_and_cno_extras.net
NET_B	$^{12}\text{C}(\alpha, \gamma)^{16}\text{O}$ from Kunz et al. (2002) + $^{14}\text{N}(\alpha, \gamma)^{15}\text{O}$ from Cyburt et al. (2010) + MESA49.net
NET_C	$^{12}\text{C}(\alpha, \gamma)^{16}\text{O}$ from Angulo et al. (1999) + $^{14}\text{N}(\alpha, \gamma)^{15}\text{O}$ from Cyburt et al. (2010) + pp_and_cno_extras.net
NET_D	$^{12}\text{C}(\alpha, \gamma)^{16}\text{O}$ from Kunz et al. (2002) + $^{14}\text{N}(\alpha, \gamma)^{15}\text{O}$ from Angulo et al. (1999) + pp_and_cno_extras.net
NET_E	$^{12}\text{C}(\alpha, \gamma)^{16}\text{O}$ from Angulo et al. (1999) + $^{14}\text{N}(\alpha, \gamma)^{15}\text{O}$ from Angulo et al. (1999) + pp_and_cno_extras.net
<b>ATM_A</b>	model atmosphere tables (Hauschildt et al. 1999a, 1999b; Castelli & Kurucz 2003)
ATM_B	$T$ - $\tau$ relation Eddington
ATM_C	$T$ - $\tau$ relation Krishna_Swamy (Krishna Swamy 1966)
ATM_D	$T$ - $\tau$ relation solar_Hopf (Paxton et al. 2013)
ATM_E	$T$ - $\tau$ relation Trampedach_solar (Ball 2021; Trampedach et al. 2014)
<b>MLT_A</b>	Heney (Heney et al. 1965)
MLT_B	ML1 (Böhm-Vitense 1958)
MLT_C	Cox (Cox & Giuli 1968)
MLT_D	Mihalas (Mihalas 1978)
<b>CONV_A</b>	predictive mixing + Schwarzschild criterion
CONV_B	predictive mixing + Ledoux criterion
CONV_C	sign change algorithm + Schwarzschild criterion
CONV_D	predictive mixing + Schwarzschild criterion + including predictive mixing in the envelope
<b>RES_A</b>	time_delta_coeff=0.50+ mesh_delta_coeff=0.50
RES_B	time_delta_coeff=0.25+ mesh_delta_coeff=0.50
RES_C	time_delta_coeff=0.50+ mesh_delta_coeff=0.25
RES_D	time_delta_coeff=0.25+ mesh_delta_coeff=0.25
RES_E	time_delta_coeff=1.00+ mesh_delta_coeff=1.00 + default MESA resolution controls

**Note.** The reference model is highlighted with bold font and is always labeled with “A.” In a given set, its relevant controls are varied only (e.g., controls related to atmospheric boundary conditions in ATM), while all other controls are set to their reference values.

Asplund et al. (2009, hereafter A09), who built the solar chemical composition model using meteoritic data and 3D non-local thermodynamic equilibrium (NLTE) models. A similar choice for scaled solar abundances was adopted, e.g., in Choi et al. (2016).

The metallicity,  $[\text{Fe}/\text{H}]$ , is calculated using the following equations:

$$[\text{Fe}/\text{H}] = \log\left(\frac{Z}{X}\right) - \log\left(\frac{Z}{X}\right)_{\odot}, \quad (1)$$

$$Z = 1 - X - Y, \quad (2)$$

$$Y = Y_p + \frac{\Delta Y}{\Delta Z} Z, \quad (3)$$

with primordial helium abundance  $Y_p = 0.2485$  (Komatsu et al. 2011). For helium enrichment,  $\Delta Y/\Delta Z$ , a range of values are considered in the literature (from 1.257 in Anderson et al. 2016 to 5 in Tognelli et al. 2011). In principle, this quantity may be determined from the calibration of the solar model. Here we arbitrarily assume  $\Delta Y/\Delta Z = 1.5$ , which is close to the value expected for the A09 solar mixture. We calculate  $X$ ,  $Y$ , and  $[\text{Fe}/\text{H}]$  based on  $Z$  and present them in Table 1. For the adopted  $Z$  values of 0.014, 0.004, and 0.0014, the corresponding metallicities,  $[\text{Fe}/\text{H}]$ , are approximately 0.0,  $-0.5$ , and  $-1.0$ , respectively.

We note that A09 composition leads to a solar abundance problem, discussed, e.g., in Section 4.3 of Asplund et al. (2009) and in Serenelli et al. (2009). The sound-speed profile, surface helium abundance, and depth of the envelope convection zone resulting from solar calibration are in a much worse agreement with helioseismic constraints as compared to the older solar mixtures by Grevesse & Noels (1993) and Grevesse & Sauval (1998). According to Serenelli et al. (2009), one possible solution to this problem would be an increase of opacities by  $\sim 15\%$ . We note that there exist newer solar mixtures, like Magg et al. (2022), for which the solar model is consistent with helioseismic observations. However, it was recently concluded by Buldgen et al. (2023, 2024) that the new mixture proposed by Magg et al. (2022) does not solve the solar problem and that helioseismic determination of the solar metal mass fraction favors the lower value of A09. The solar mixture of Magg et al. (2022) and corresponding opacities are not yet implemented in MESA.

In addition to A09 in the reference model, we investigate two already mentioned scaled solar mixtures, namely, Grevesse & Sauval (1998, hereafter GS98) and Grevesse & Noels (1993, hereafter GN93). We keep the value of  $[\text{Fe}/\text{H}]$  fixed to that from the reference model and recalculate  $X$ ,  $Y$ , and  $Z$  as given in Table 1. In the following, models adopting different scaled solar abundances are referred to as MIX (see Table 2).

### 2.2.2. Atomic Diffusion

In the reference model, atomic diffusion is not included. To test the effects of atomic diffusion on evolutionary tracks, we consider a model set in which diffusion is enabled. All MESA controls relevant to atomic diffusion are fixed to their default values. Models computed with atomic diffusion enabled are referred to as DIFF (see Table 2).

### 2.2.3. Equation of State

The EOS in MESA has a tabular form and is derived by the eos module. This module defines regions in the parameter space of temperature, density, and composition where EOS tables from different sources, or their blends, are used. The EOS tables used are OPAL (Rogers & Nayfonov 2002), SCVH (Saumon et al. 1995), HELM (Timmer & Swesty 2000), PC (Potekhin & Chabrier 2010), and Skye (Jermyn et al. 2021). For detailed ranges where specific references are used to calculate EOS, see figures in the documentation of MESA.<sup>4</sup>

<sup>4</sup> <https://docs.mesastar.org/en/release-r21.12.1/eos/overview.html>



### 2.2.4. Nuclear Reaction Network

In the reference model, we use a nuclear reaction net called `pp_and_cno_extras.net` that explicitly tracks 25 species ( $^1\text{H}$ ,  $^2\text{H}$ ,  $^3\text{He}$ ,  $^4\text{He}$ ,  $^7\text{Li}$ ,  $^7\text{Be}$ ,  $^8\text{B}$ ,  $^{12}\text{C}$ ,  $^{13}\text{C}$ ,  $^{13}\text{N}$ ,  $^{14}\text{N}$ ,  $^{15}\text{N}$ ,  $^{14}\text{O}$ ,  $^{15}\text{O}$ ,  $^{16}\text{O}$ ,  $^{17}\text{O}$ ,  $^{18}\text{O}$ ,  $^{17}\text{F}$ ,  $^{18}\text{F}$ ,  $^{19}\text{F}$ ,  $^{18}\text{Ne}$ ,  $^{19}\text{Ne}$ ,  $^{20}\text{Ne}$ ,  $^{22}\text{Mg}$ ,  $^{24}\text{Mg}$ ) that includes reactions of the pp and CNO cycles, as well as helium and heavier-element burning. The nuclear reaction rates come from NACRE (Angulo et al. 1999) except for the rate of  $^{12}\text{C}(\alpha, \gamma)^{16}\text{O}$ , a dominant reaction of the  $3\alpha$  chain, for which we use Kunz et al. (2002), and  $^{14}\text{N}(\text{p}, \gamma)^{15}\text{O}$ , the slowest reaction of the CNO cycle, for which we use the JINA REACLIB rate (Cyburt et al. 2010).

We also investigate other reactions and reaction rates, which include changing the net to `mesa_49.net`, which tracks 49 species and their reactions, and changing the two individual reaction rates mentioned above,  $^{12}\text{C}(\alpha, \gamma)^{16}\text{O}$  and  $^{14}\text{N}(\text{p}, \gamma)^{15}\text{O}$ , to NACRE rates.

In the following, models with varied nuclear net and specific reaction rate options are referred to as NET (see Table 2).

### 2.2.5. Model Atmosphere

Surface temperature and surface pressure of a model are calculated in the `atm` module by either interpolating atmosphere tables or applying a user-specified  $T(\tau)$  relation. Our reference model uses PHOENIX tables from the Hauschildt et al. (1999a, 1999b) and Castelli & Kurucz (2003) models. We also investigated  $T(\tau)$  relations of Eddington, Krishna Swamy (Krishna Swamy 1966), Trampedach\_solar option (Trampedach et al. 2014; Ball 2021), and solar\_Hopf option (see Section A.5 of Paxton et al. 2013 for details). In the following, we refer to this set of models by ATM (see Table 2).

### 2.2.6. MLT and Convective Boundaries

In MESA, convective mixing is treated as a time-dependent diffusive process described by the MLT. Different implementations of MLT can be specified by the user. For the reference model, we use the formulation by Henyey et al. (1965), which allows convective efficiency to vary with opacity. Later we investigate MLT versions from Böhm-Vitense (1958), Cox & Giuli (1968), and Mihalas (1978). In the following, models adopting different MLT formulations are referred to as MLT (see Table 2).

Boundaries of convective regions are determined by the Schwarzschild criterion

$$\nabla_{\text{rad}} > \nabla_{\text{ad}}. \quad (4)$$

The alternative is the Ledoux criterion, which takes into account possible composition gradients

$$\nabla_{\text{rad}} > \nabla_{\text{ad}} - \frac{\varphi}{\delta} \nabla_{\mu}, \quad (5)$$

where  $\nabla_{\mu}$  is a gradient of mean molecular weight and

$$\varphi = \left( \frac{\partial \ln \rho}{\partial \ln \mu} \right), \quad \delta = \left( \frac{\partial \ln \rho}{\partial \ln T} \right).$$

There are three algorithms for calculating convective boundaries in MESA: the classic sign change algorithm described in Paxton et al. (2013), predictive mixing (PM) introduced in Paxton et al. (2018), and convective premixing

(CPM) introduced in Paxton et al. (2019). The last scheme is broken in r21.12.1.<sup>5</sup> Consequently, the CPM scheme was not used in the present investigation. We note that CPM also leads to breathing pulses at the end of CHeB. Their nature is still disputed (Caputo et al. 1989; Dorman & Rood 1993; Cassisi et al. 2001, 2003; Constantino et al. 2016, 2017); they may be a numerical artifact of the modeling.

All algorithms look for a cell at which the quantity  $y = \nabla_{\text{rad}} - \nabla_{\text{ad}}$  changes its sign. In the case of a chemical composition discontinuity, the classic sign change algorithm may return a boundary where  $y > 0$  at the convective side, which is unphysical and retards the growth of the convective core. PM was implemented to solve this issue via modifying diffusivities at the boundary, effectively introducing a small amount of mixing until  $y = 0$  at the convective boundary. This algorithm may still fail, e.g., applied to a shell of a high-mass star on the main sequence or to a helium-burning core of a solar-mass star.

In the reference model, we use the PM scheme with the Schwarzschild criterion in the core (see, e.g., Anders et al. 2022b, for support of that choice) and the classic sign change algorithm with the Schwarzschild criterion in the envelope (a model referred to as PMS). Later we investigate PM in the core and sign change in the envelope but with the Ledoux criterion (PML); PM both in the core and in the envelope, with the Schwarzschild criterion (PMSenv); and finally the classic sign change algorithm with the Schwarzschild criterion in the core and in the envelope (SCS). We refer to these models as CONV (see Table 2).

We note that, by design, the PM algorithm should give exactly the same boundary location, regardless of the convective stability criterion used. Nevertheless, the PML and PMS models may differ, as a simple sign change algorithm is used to determine the boundaries of the convective envelope (which is justified by the much smaller composition gradients expected in the envelope).

## 2.3. Solar Calibration

An important aspect of the MLT is the mixing efficiency, characterized by the  $\alpha_{\text{MLT}}$  parameter. It is defined as the distance  $l$ , expressed in pressure scale heights  $H_p$ , that a convective element travels before it blends with its surroundings,  $l = \alpha_{\text{MLT}} H_p$ . There is no theoretical constraint for  $\alpha_{\text{MLT}}$ ; rather, it is a common practice to calibrate it with respect to the Sun. For this purpose, we used a test suite provided in MESA, `simplex_solar_calibration`. The procedure evolves the model from the pre-main sequence, past the solar age, with atomic diffusion enabled. The algorithm varies initial metal and helium content,  $Z_{\text{ini}}$  and  $Y_{\text{ini}}$ , and  $\alpha_{\text{MLT}}$  to reproduce the solar luminosity, effective temperature ( $T_{\text{eff}} = 5772 \pm 0.8$  K from Prša et al. 2016), surface abundance of metals, and surface-metals-to-hydrogen ratio ( $Z_{\text{surf}} = 0.0134$ ,  $(Z/X)_{\text{surf}} = 0.0181$  from Asplund et al. 2009) at the current solar age (4.57 Gyr from Connelly et al. 2012). We do not take surface helium abundance, the depth of the convection zone, or the sound speed profile as constraints because the adopted solar composition does not allow us to reproduce these helioseismic observables; see Section 2.2.1.

We made separate calibrations for the reference model and the ATM, MLT, and MIX sets, as varying the underlying

<sup>5</sup> <https://github.com/MESAHub/mesa/issues/425>

**Table 3**

Solar Calibration Results for the Reference Set and for Varied Atmosphere, MLT, and Solar Mixture Options

	$\alpha_{\text{MLT}}$	$Y_{\text{ini}}$	$Z_{\text{ini}}$
Reference set	1.77	0.2649	0.01497
Atmosphere Variants			
Krishna Swamy	2.07	0.2648	0.01497
Solar Hopf	1.98	0.2649	0.01497
Eddington	1.77	0.2649	0.01497
Trampedach_solar	1.88	0.2647	0.01498
MLT Version			
Cox	1.77	0.2649	0.01498
ML1	1.77	0.2649	0.01497
Mihalas	1.74	0.2649	0.01497
Solar Mixture Variants			
GN93	1.87	0.2718	0.01971
GS98	1.86	0.2723	0.01869

parameters may influence  $\alpha_{\text{MLT}}$ . Results of the calibration are presented in Table 3. For each set of models and variants included therein, the corresponding  $\alpha_{\text{MLT}}$  and initial helium and metal abundances are given.

#### 2.4. Numerical Convergence

MESA offers a variety of parameters controlling spatial and temporal resolution of the model. In all our model sets, except one in which we use MESA default settings, we use controls that limit the relative change of parameters ( $\log T_{\text{eff}}$ ,  $\log L$ ) at the surface and at the center ( $\log T$  and  $\log \rho$ ).

Additionally, we limit the maximum time step possible to  $10^6$  yr. Relative variation in the structure variables from one model to the next is limited to  $10^{-4}$  (with `varcontrol_target=1d-4`). See the `inlist` in Appendix A for details.

While there are numerous controls that allow us to adjust spatial and temporal resolution at specific conditions, there are two controls that allow for an overall adjustment. These are `mesh_delta_coeff` for spatial resolution and `time_delta_coeff` for temporal resolution. Cutting `mesh_delta_coeff` in half will roughly double the number of grid points. Using smaller values of `time_delta_coeff` results in shorter time steps and better temporal resolution, with the cost of extending the computation time. By default, both of these controls are equal to 1, while in our reference model we set these controls to 0.5 using higher spatial and temporal resolution approximately by a factor of 2.

We consider five variants of resolution controls as detailed in Table 2. The set of models computed with different resolutions is referred to as RES. For this set, in Figure 18 in Appendix B, we show H-R diagrams for 2–8  $M_{\odot}$  and for three different metallicities. Overall we see a very satisfactory agreement for tracks computed with different resolution controls for a range of considered masses and metallicities. Except for a few cases, differences between tracks are barely noticeable. For lower masses, some sensitivity is visible for solar metallicity and 5  $M_{\odot}$ . The H-R diagram for this particular case is plotted in the top panel of Figure 1. Details of the loop, in particular its extent, do depend on resolution controls. The track computed with the lowest resolution (RES\_E) shows the shortest loop.

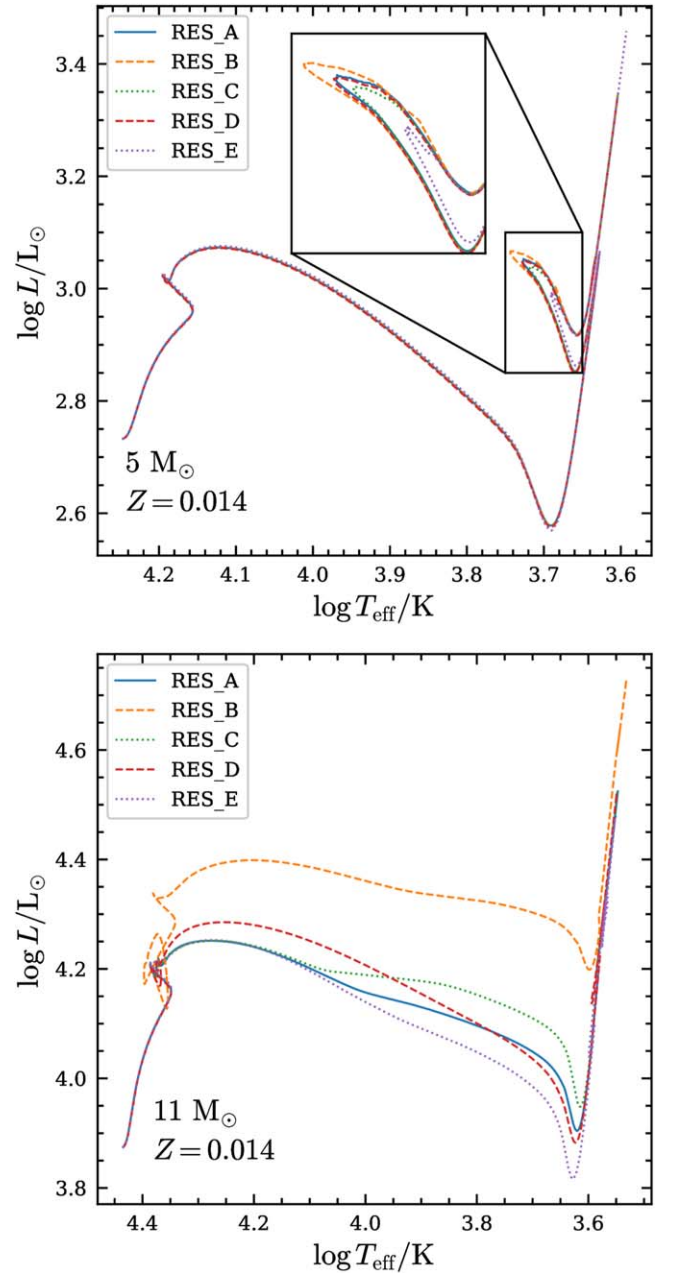


**Figure 1.** Tracks with different numerical resolution controls for 5 and 11  $M_{\odot}$  and solar metallicity. Labels are defined in Table 2.

We note, however, that RES\_A (reference model) and RES\_D (highest resolution) agree very well. The differences are visible for 8  $M_{\odot}$  models, including qualitative differences for the largest metallicity ( $Z=0.014$ ). RES\_A and RES\_B models do develop a loop, while others do not. For the lowest metallicity ( $Z=0.0014$ ) and 8  $M_{\odot}$ , helium burning starts on the way to the RGB for all considered models. However, the location in the H-R diagram at helium ignition and the luminosity of the track at helium burning depend on resolution controls.

In the following, the resolution controls of RES\_A are adopted for our reference model. These controls assure convergence across the considered masses and metallicities and lead to very reasonable computing time.

The situation is qualitatively different for higher masses. For the considered resolution controls, in Figure 27 in Appendix B, we show the H-R diagrams for 9–15  $M_{\odot}$  and for three different

metallicities. For nearly all combinations of mass and metallicity, the tracks strongly depend on the adopted resolution controls, and for no set can we claim overall numerical convergence. While convergence is present for the main-sequence phase—for all masses and metallicities tracks nicely overlap—strong differences arise as soon as hydrogen is depleted in the core. We highlight this point with  $11 M_{\odot}$  and  $Z = 0.014$  tracks displayed in the bottom panel of Figure 1. The track with increased temporal resolution (RES\_B) shows several turnoffs after the main sequence and is significantly more luminous at later stages of evolution. Other tracks also show peculiar behavior at the main-sequence hook. As we study later in Section 3.3, all high-mass tracks are affected by the development of thin convective shells, at a location corresponding to the maximum extent of the convective core during main-sequence evolution. These shells seem to evolve in an erratic manner, and while they finally disappear before helium is ignited in the core, they strongly affect the abundance profiles across the model, which in turn affects the helium-burning phase. Consequently, for the remainder of our paper, we decide that models spanning  $2\text{--}8 M_{\odot}$  and  $9\text{--}15 M_{\odot}$  should be analyzed separately.

### 2.5. Convective Core Overshooting

Concerning convective core overshooting during the main-sequence phase, we consider two cases: without and with moderate overshooting. We use an exponential prescription for overshooting, as introduced in Herwig (2000; see also Paxton et al. 2011), with  $f = 0.02$ . All model sets discussed so far (i.e., INT, MIX, NET, etc.) are computed without and with convective core overshooting, and results are discussed separately for these two cases.

In all calculations, we neglect overshooting from the convective envelope and from the helium-burning core. Similar to rotation and mass loss, the extent of overshooting from the convective envelope may be regarded as a primary parameter, in particular, when the CHeB phase and problems related to Cepheid evolution are considered. The extent of envelope overshooting may strongly affect the extent of the blue loop (see, e.g., Alongi et al. 1991; Bressan et al. 2012). In our following model survey, the extent of the envelope overshooting will be one of the parameters varied in the grid. On the other hand, test calculations we have conducted show that the extent of overshooting from the helium-burning convective core has a small effect on the blue loops, while its inclusion may lead to numerical issues as analyzed by Ostrowski et al. (2021).

### 2.6. Quantifying Differences between the Models

We compare the models calculated with different sets of parameters, INT, MIX, DIFF, NET, ATM, MLT, CONV, and RES, at specific benchmark points on the evolutionary tracks, for which we initially chose the middle of the main sequence (mMS), the terminal-age main sequence (TAMS), the base of the RGB (bRGB), the tip of the RGB (tRGB), the beginning of core helium burning (bCHeB), when half of the helium in the core is exhausted (mCHeB), and the end of core helium burning (eCHeB). Definitions of these benchmark points are summarized in Table 4.

In addition, we also consider the middle point of the classical IS (mIS). To get the mIS point, we use the radial stellar

**Table 4**  
Definitions of Benchmark Points

Point	Definition
mMS	$X_c = 0.5$
TAMS	$X_c = 0.00001$
bRGB	$L_{\min}$ between TAMS and mCHeB
tRGB	$L_{\max}$ between bRGB and mCHeB
bCHeB	$Y_c = 0.95Y_{c,\text{TAMS}}$
mCHeB	$Y_c = 0.5$
eCHeB	$Y_c = 0.00001$
mIS	interpolated on the second crossing of the IS

pulsation (RSP) tool available in MESA (Smolec & Moskalik 2008; Paxton et al. 2019) to determine the boundaries of the IS. To this aim, RSP models are computed along the blueward evolution during CHeB. Growth rates for the fundamental mode,  $\gamma_F$ , are computed, and the location of the boundary is interpolated to satisfy  $\gamma_F = 0$ . We stress that the RSP calculation, whenever possible, uses the same settings of microphysical data as evolutionary tracks. Details of the pulsation calculations will be given in a separate paper (R. S. Rathour et al. 2024, in preparation).

When analyzing the results, we noticed that recorded differences are similar for mMS, TAMS, and bRGB and for TAMS and bCHeB. Consequently, when presenting the detailed results in figures, we focus on TAMS, tRGB, mCHeB, eCHeB, and mIS points. All points are included in the summary plots accompanying the discussion in Section 4.

The quantities that we compare at benchmark points are logarithm of luminosity  $\log L$ , logarithm of effective temperature  $\log T_{\text{eff}}$ , and logarithm of age. We interpolate these quantities at the precise location of a given benchmark point on the evolutionary track. Then, for each quantity and for each benchmark point along each evolutionary track, we compute a relative difference with respect to a corresponding quantity in the reference (“A”) model. For example, for luminosity at mMS and some evolutionary model  $i$ , we compute

$$\delta L = (L_{\text{mMS}, i} - L_{\text{mMS}, A}) / L_{\text{mMS}, A}, \quad (6)$$

where  $L_{\text{mMS}, A}$  is the luminosity of the reference model at mMS. We record the maximum and minimum relative difference for each considered set of models (i.e., for INT, MIX, NET, etc.).

We decided to analyze the uncertainty of the age, together with the fundamental parameters, since one of our future goals is to derive the period–age relations for classical Cepheids.

## 3. Results

To give an overview of results, in Figure 2 we show evolutionary tracks for  $2, 5$ , and  $8 M_{\odot}$  and metal contents of  $Z = 0.014, 0.004$ , and  $0.0014$  for all computed evolutionary tracks (all sets; altogether 23 tracks in each panel; see Table 2) plotted in gray, with a reference track plotted in blue. A remarkable overlap of tracks during the main-sequence phase is apparent. Then, tracks follow a similar path toward the RGB, at which some dispersion in effective temperature may be noticed. Finally, while luminosity levels at CHeB are quite similar in all tracks, the extents and shapes of the blue loops may vary significantly.

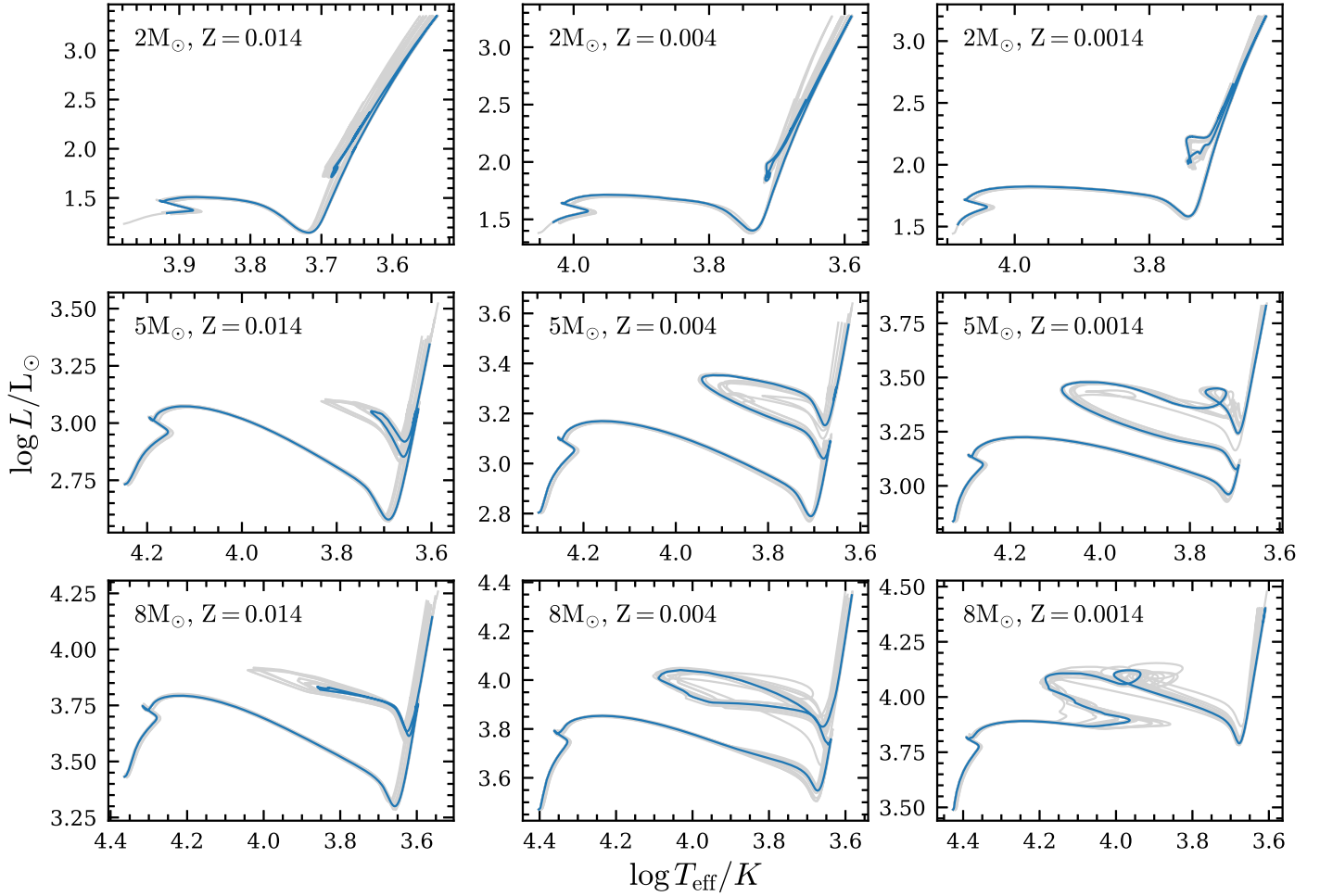


**Figure 2.** Evolutionary tracks for 2, 5, and 8  $M_{\odot}$  and metal contents  $Z = 0.014$ , 0.004, and 0.0014. Reference tracks are shown in blue and all other ones in gray.

A collection of H-R diagrams for all considered masses and metallicities and comparing the reference tracks with those of a given set of models is included in a series of figures in Appendix B, Figures 11–28. In each figure, mass changes in rows, metallicity changes in columns, and models within a given model set are plotted with different colors and line styles. The evolutionary tracks may be downloaded from Zenodo under an open-source Creative Commons Attribution license at doi:[10.5281/zenodo.12550758](https://doi.org/10.5281/zenodo.12550758).

In Tables 8–17 in Appendix C we give the maximum and minimum relative differences of  $\log$  age,  $\log T_{\text{eff}}$ , and  $\log L$  with respect to a reference model, taking into account all computed 2–8  $M_{\odot}$  models (from all sets of models considered in the paper). Tables 8–12 present the results for TAMS, tRGB, mChEB, eChEB, and mIS, respectively, and models without convective core overshooting, while Tables 13–17 present the results for models computed with convective core overshooting. Part of such a table for TAMS is illustrated as Table 5.

As already noted, results for mMS and TAMS, TAMS and bRGB, and tRGB and bChEB are quite similar. Consequently, while we discuss all benchmark points in the discussion, in this section, for clarity of figures, we present results for just five benchmark points, TAMS, tRGB, mChEB, eChEB, and mIS.

We note that mIS is specific, as it has a very well-defined effective temperature, resulting from crossing of the nearly

vertical line, defining the center of the IS, with evolutionary tracks. As a consequence, while luminosities may significantly differ at mIS, the relative differences in effective temperature are always very small.

### 3.1. Low-mass Models, 2–8 $M_{\odot}$ , without Convective Core Overshooting

The H-R diagrams for 2–8  $M_{\odot}$  models without convective core overshooting, presenting evolutionary tracks within a given set of models, are presented in Appendix B, in Figures 11 (INT), 12 (MIX), 13 (DIFF), 14 (NET), 15 (ATM), 16 (MLT), 17 (CONV), and 18 (RES). Information on the recorded maximum and minimum relative differences with respect to a reference model, for five benchmark points, is visualized in Figure 3. Each panel corresponds to one evolutionary point with the recorded maximum and minimum relative differences for  $\log$  age,  $\log T_{\text{eff}}$ , and  $\log L$  against mass. The shape of a marker indicates the metal content, and the color indicates the model set that gives rise to the extreme difference, according to the key in the upper right corner.

We notice that for 8  $M_{\odot}$  and  $Z = 0.0014$  tracks do not go through a standard RGB evolution, as helium is ignited earlier, on the way toward the RGB; see the bottom right panel of Figure 2. For this reason and this specific  $M/Z$  data for the tRGB are missing in Figure 3.



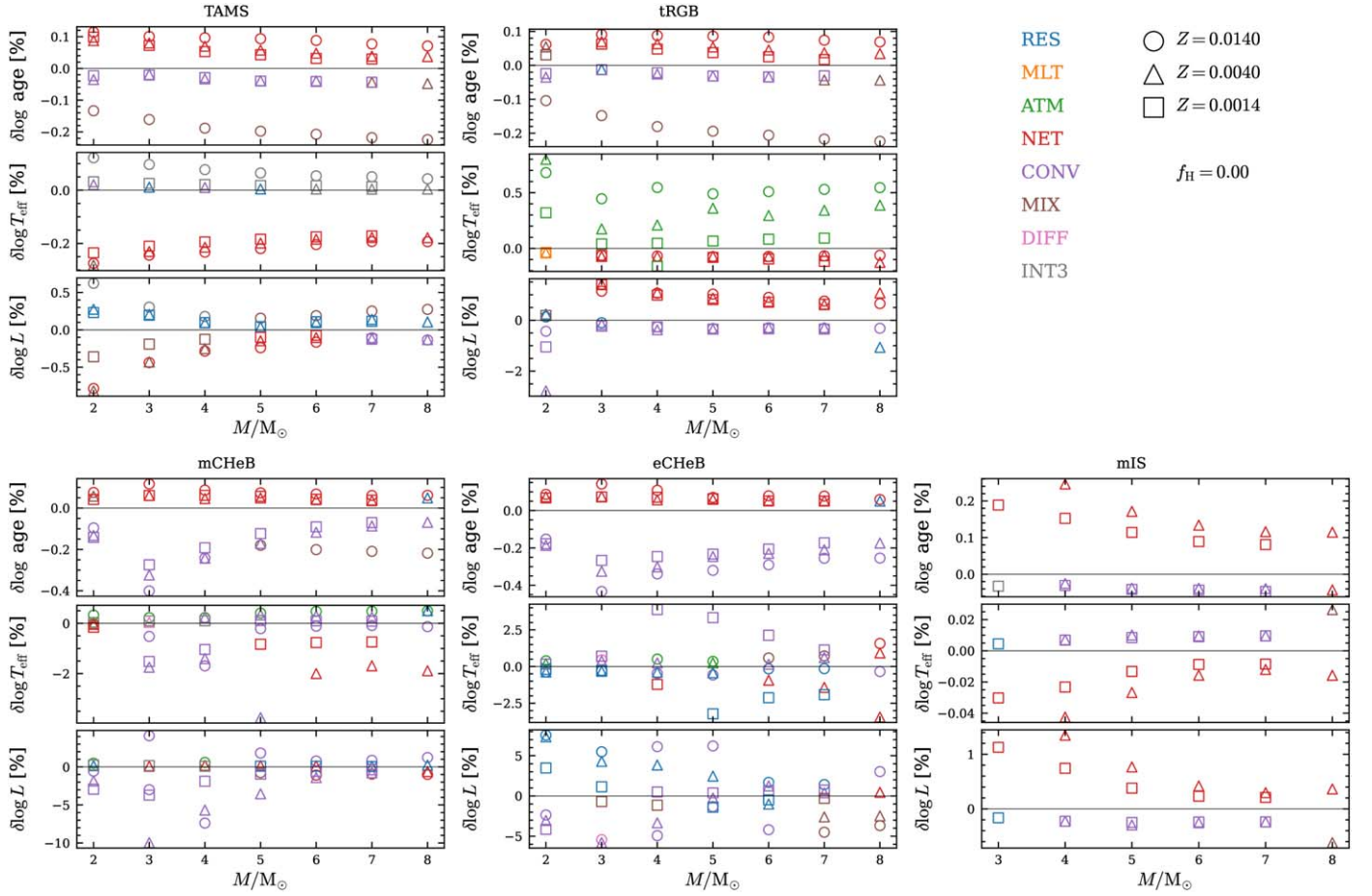


**Figure 3.** A maximum relative difference with respect to the reference evolutionary model for log age, effective temperature, and luminosity at TAMS, tRGB, mChEB, eChEB, and mIS (see Table 4) as a function of mass. Metal content changes accordingly with shape of the marker. The color of the symbol indicates the model set that gives rise to the maximum relative difference for a given  $M$  and  $Z$ .

**Table 5**  
Comparison of Physical Quantities (Ages, Effective Temperatures, Luminosities; All in Logarithms) of Models 2–8  $M_{\odot}$  at TAMS

Mass	$Z$	$\log \text{age}^{\text{ref}}$	$\log \text{age}^{\text{max}}$	$\log \text{age}^{\text{min}}$	$\log T_{\text{eff}}^{\text{ref}}$	$\log T_{\text{eff}}^{\text{max}}$	$\log T_{\text{eff}}^{\text{min}}$	$\log L^{\text{ref}}$	$\log L^{\text{max}}$	$\log L^{\text{min}}$
2.0	0.0014	8.76151	8.77015	8.75952	4.06721	4.0685	4.05764	1.73978	1.74381	1.73351
			NET_E	CONV_B		INT_B	NET_E		RES_E	MIX_C
2.0	0.004	8.82421	8.83195	8.82112	4.00795	4.00878	3.99665	1.66051	1.66508	1.64696
			NET_E	CONV_B		CONV_B	MIX_C		RES_E	MIX_C
2.0	0.014	8.95149	8.96172	8.93954	3.91538	3.92016	3.90461	1.48295	1.49218	1.47131
			NET_D	MIX_C		INT_B	NET_D		INT_B	NET_E
3.0	0.0014	8.33653	8.34257	8.3348	4.16385	4.16492	4.1551	2.39126	2.39596	2.38668
			NET_E	CONV_B		INT_B	NET_E		RES_E	MIX_B
3.0	0.004	8.38258	8.38929	8.38097	4.11289	4.11335	4.10341	2.32897	2.33377	2.31896
			NET_E	CONV_B		RES_D	NET_D		RES_E	MIX_C
3.0	0.014	8.4783	8.48683	8.46465	4.03285	4.03675	4.023	2.19327	2.19994	2.18364

**Note.** Columns mark mass, initial metal abundance, age of the reference model, maximal and minimal values of age for a given mass and  $Z$  with the corresponding set in the subrow, effective temperature of the reference model, maximal and minimal values of effective temperature for a given mass and  $Z$  with the corresponding set in the subrow, log of luminosity ( $\log L$ ) of the reference model, and maximal and minimal values of  $\log L$  for a given mass and  $Z$  with the corresponding set in the subrow.

Considering location in the H-R diagram ( $\log T_{\text{eff}}$ ,  $\log L$ ), the relative differences are usually very small, typically well below 1%. Only for later evolutionary stages can they become larger, but still at a level of a few percent only. During the main-sequence evolution, all tracks nearly overlap for all masses and metallicities. The recorded differences for mMS and TAMS are always very small, never exceeding 1%. The largest differences

are recorded for 2  $M_{\odot}$  models. Most of the extreme differences arise as a result of different nuclear reaction rates as discussed in more detail below. At later evolutionary stages, the treatment of convective boundaries also contributes to the recorded extreme differences.

For ages, the extreme differences are recorded mostly for NET and MIX models. We note, however, that these maximum



differences are always very low, never exceeding 0.5%, and typically are much smaller.

We note that for several cases we record the largest relative differences, on the order of a few percent, at eCHeB, which is related to mixing events at this evolutionary phase, the breathing pulses. While these are strongly reduced when the PM scheme is used, they may still occur in the models. Larger events are accompanied by secondary loops in the H-R diagram, and smaller ones may be traced by analyzing abundance profiles. Whether the event has occurred or not may strongly affect the location and model properties of our benchmark point, eCHeB, in particular its luminosity. Since the nature of breathing pulses is likely numerical (see Section 2.2.6), the larger sensitivity at eCHeB may be a numerical issue.

We now elaborate on the differences recorded within specific sets of models.

### 3.1.1. Interpolation in Opacity Tables, INT

Evolutionary tracks for this set of models are presented in Figure 11 in Appendix B. While in general evolutionary tracks computed with cubic and linear interpolation in opacity tables do overlap, some differences are clear, in particular at solar metallicity. The main sequence is noticeably brighter and hotter when linear interpolation is used;  $\log L$  differs by up to 0.63% for mMS and  $2 M_{\odot}$  at solar metallicity (the largest recorded difference at this  $M/Z$  across all considered models) as compared to the reference track computed with cubic interpolation. The difference decreases with increasing mass. Interestingly, at the TAMS (see Figure 3), the largest relative difference of effective temperature across all considered model sets is recorded for models with linear interpolation in opacity tables. This difference is the largest at solar metallicity and decreases with increasing mass, from 0.12% (at  $2 M_{\odot}$ ) to 0.04% (at  $8 M_{\odot}$ ). Differences are also clear during CHeB, with the largest qualitative discrepancy for  $8 M_{\odot}$ : when linear interpolation is used, the blue loop does not develop. For the lower metallicities, the differences are noticeably smaller.

### 3.1.2. Scaled Solar Abundance, MIX

In Figure 12 in Appendix B we show evolutionary tracks computed for different solar mixtures of heavy elements, A09, GS98, and GN93. The overall agreement of tracks is good; tracks for GN93 and GS98 nearly overlap and are slightly shifted with respect to the reference A09 tracks. For all masses and metallicities, the reference solar mixture A09 produces tracks that are slightly more luminous and a bit hotter on the main sequence and with the RGB shifted a bit toward cooler temperatures. Differences are the largest during CHeB, in particular at solar metallicity. For masses above  $5 M_{\odot}$  the loops are much longer for GN93 and GS98, easily reaching the IS, while for A09 and 6 and  $7 M_{\odot}$  the loops do not develop at all. Interestingly, for two lower metallicities, all tracks with  $M > 2 M_{\odot}$  do develop loops that are slightly longer for A09.

For log age, the use of GN93 at solar metallicity leads to the shortest possible log age across all considered model sets for mMS, TAMS, and tRGB (see Figure 3). The relative difference (at TAMS) is increasing with increasing mass from 0.13% ( $2 M_{\odot}$ ) to 0.22% ( $8 M_{\odot}$ ).

### 3.1.3. Diffusion, DIFF

In Figure 13 in Appendix B we compared evolutionary tracks with and without atomic diffusion. The two types of tracks overlap almost perfectly; however, when the diffusion is included, the blue loops are not smooth—small fluctuations appear on tracks (which are not visible in the scale of Figure 13), and some of the models fail to converge after helium is depleted in the core and thus evolution is terminated earlier. Considering location on the H-R diagram, typical relative differences are less than 0.1%, with a maximum difference of around 5% (for  $\log L$ ) for the  $3 M_{\odot}$  model at solar metallicity at eCHeB.

### 3.1.4. Nuclear Reactions, NET

Evolutionary tracks for NET models are shown in Figure 14 in Appendix B. First, we note that changing the nuclear net to a more extensive one, with 49 elements and their reactions, mesa\_49.net, labeled as NET\_B, does not affect evolutionary tracks in any essential way.

We can distinguish two groups of tracks that differ qualitatively. In NET\_A, NET\_B, and NET\_C the reaction rate of  $^{14}\text{N}(p, \gamma)^{15}\text{O}$  comes from Cyburt et al. (2010), and in NET\_D and NET\_E it comes from Angulo et al. (1999). This reaction is the slowest one in the hot CNO cycle, setting the rate of the whole cycle. The reaction rate from Cyburt et al. (2010) is significantly lower (for  $T_9 < 0.2$ ; for  $0.2 < T_9 < 2$  it is in good agreement with Angulo et al. 1999), which results in brighter MS and shorter loops, as seen in Figure 14 for the solar metallicity, which is in agreement with results of, e.g., Weiss et al. (2005). For the lower metallicities, however, the loops with the lower rate are longer.

The use of the Angulo et al. (1999) rate for  $^{14}\text{N}(p, \gamma)^{15}\text{O}$  (NET\_D and NET\_E) results in the largest log age values at almost all benchmark points, masses, and metallicities and across all considered model sets, which is a consequence of a longer main-sequence phase; see Figure 3. The relative difference in log age with respect to the reference track is on the order of 0.1%.

The rate for  $^{12}\text{C}(\alpha, \gamma)^{16}\text{O}$  reaction matters only during and after CHeB. For the lower metallicities the blue loops computed with the two reaction rates we study, Kunz et al. (2002) (NET\_A) and Angulo et al. (1999) (NET\_C), are very similar, with no noticeable differences. At solar metallicity the blue loops for models adopting the Kunz et al. (2002) rate may be shorter. The C/O core composition at the end of CHeB is significantly affected, with the use of the Kunz et al. (2002) reaction rate leading to higher  $^{12}\text{C}$  and lower  $^{16}\text{O}$  content. As a consequence, at solar metallicity, the  $^{12}\text{C}/^{16}\text{O}$  ratio at the center of the core at the end of CHeB is about 17%–26% lower when using the Angulo et al. (1999) rate, depending on the mass.

### 3.1.5. Atmospheres, ATM

Evolutionary tracks for the ATM set are plotted in Figure 15 in Appendix B. The differences among tracks are clear at the RGB and later at the asymptotic giant branch (AGB), at which the tracks are parallel and shifted toward a higher effective temperature as compared to the reference track. The largest differences are recorded at solar metallicity for the Krishna Swamy (ATM\_C) model and are on the order of 0.5%–0.7%. The relative differences in  $\log T_{\text{eff}}$  decrease with decreasing

metallicity and are typically on the order of 0.2%–0.3% at  $Z=0.004$  and on the order of 0.1% at the lowest metallicity. The (positive) relative differences arising in the ATM set in  $\log T_{\text{eff}}$  at the tRGB and bChEB are the largest across all computed models.

The extent of the blue loops is generally not affected. The reference model (which uses atmosphere tables) at  $8 M_{\odot}$  and at solar metallicity has a significantly extended blue loop compared to models with  $T-\tau$  relations that all have a short loop for this mass and metallicity. The small differences at blue loops decrease with decreasing metallicity.

### 3.1.6. MLT

The choice of MLT seems not to affect the lower-mass tracks (Figure 16 in Appendix B) except for the barely noticeable change in the shape of the loop for the  $8 M_{\odot}$  track at solar metallicity when using the Mihalas (1978) MLT. The typical relative differences in location on the H-R diagram are below 0.1%. The highest difference of roughly 4.5% was recorded for  $\log L$  at eChEB for the  $3 M_{\odot}$  model at solar metallicity when applying Cox’s MLT. Comparing with the reference model, we noticed that this difference appears to be due to a small mixing event at the end of ChEB, which extended this evolutionary phase when Cox’s MLT was used.

### 3.1.7. Boundaries of Convective Regions, CONV

Evolutionary tracks for the CONV set are plotted in Figure 17 in Appendix B. The differences between tracks computed with the sign change algorithm and adopting PM are the most apparent across all masses and metallicities. At solar metallicities and for tracks adopting PM, differences are also present for models using Schwarzschild and Ledoux criteria. For 4, 5, and  $8 M_{\odot}$  at  $Z=0.014$  the tracks with a long loop are those in which the Schwarzschild criterion has been implemented, either in the core or in the core and the envelope. Tracks with the Ledoux criterion or classic sign change algorithm have a short loop. In general, for other masses and lower metallicities, the differences between tracks with Schwarzschild versus Ledoux (adopting PM scheme) are not significant. The largest relative differences are recorded when applying the classic sign change algorithm (CONV\_C) versus PM in the core in the reference models. For this case and  $Z=0.004$  and  $0.0014$  the blue loops have a more irregular shape and their second half is noticeably dimmer.

As evidenced in Figure 3, models from the CONV set most often give rise to the largest recorded relative differences in  $\log$  age and in the location on the H-R diagram across all computed models and evolutionary phases. The largest differences arise as a result of the model adopting the sign change algorithm (CONV\_C) during the blue loop phase (up to a few percent in the location on the H-R diagram) and as a result of the model adopting the PM scheme and Ledoux criterion (CONV\_B) at other evolutionary phases. Although the PM scheme was designed to yield the same result whether the Ledoux or Schwarzschild criterion is used, in our case the differences are present because in the envelope we use the classic sign change algorithm. Still, the differences are very small, typically on the order of 0.1% or below.

### 3.1.8. Spatial and Temporal Resolution, RES

Evolutionary tracks for the RES set are plotted in Figure 18 in Appendix B. The solar-metallicity models have short blue loops. This is especially visible for 6 and  $7 M_{\odot}$ , which lack blue loops. For  $5 M_{\odot}$  the loop is sensitive to resolution as discussed in Section 2.4 (see also Figure 1), and for  $8 M_{\odot}$  the loop is extremely affected by the change of the resolution controls: RES\_A and RES\_B models developing the loop, others not. We note that  $8 M_{\odot}$  is the only model at solar metallicity that enters the IS with an “inverted” blue loop, i.e., the second crossing is more luminous than the third.

For the lower metallicities, the problem of short loops is diminished. The lowest mass for entering the IS is  $3 M_{\odot}$ . Tracks with  $8 M_{\odot}$  and  $Z=0.004$  are slightly sensitive to spatial and temporal resolution on the RGB and on the blue loop.

In the case of the lowest metallicity,  $Z=0.0014$ , the loops are the longest, and secondary loops appear in tracks with masses above  $4 M_{\odot}$ . Once again, the models with  $8 M_{\odot}$  are the most sensitive to resolution, especially temporal resolution, which is increased for RES\_B and RES\_D.

In general, the relative differences in the location on the H-R diagram do not exceed 1% and are typically well below 0.1%. The highest relative differences, reaching about 8%, stem from the models that use the default (coarse) numerical resolution (RES\_E). The relative differences in  $\log$  age are well below 0.05%.

### 3.2. Low-mass Models, 2–8 $M_{\odot}$ , with Main-sequence Convective Core Overshooting

In Figure 4 we compare the reference tracks computed without and with convective core overshooting ( $f=0.02$ ; see Section 2.5) during the main-sequence phase. The effects of this moderate core overshoot are strong at all evolutionary phases. The main-sequence phase is brighter and longer; TAMS extends toward larger luminosity and lower effective temperatures. The overall evolution proceeds at higher luminosities. We note that at solar metallicity the short-loop problem is largely eliminated. Blue loops start to enter the IS for  $5 M_{\odot}$ , and the loop is well developed at higher masses. For the lower metallicities, the loops are brighter and in general significantly shorter than in the case without convective core overshooting. For  $Z=0.004$  and convective core overshoot, the loops are significantly reduced. They enter the IS only for 7 and  $8 M_{\odot}$ , and for these models they are very thin, with nearly the same luminosity for the second and third crossings. For the lowest metallicity,  $Z=0.0014$ , and models with convective core overshooting, the loops are regular and enter the IS for  $3 M_{\odot}$  and above. Their luminosity extent is lower than that of models without convective core overshooting.

H-R diagrams for 2–8  $M_{\odot}$  models with convective core overshooting during the main-sequence phase, showing evolutionary tracks within a given set of models, are presented in Figures 19 (INT), 20 (MIX), 21 (DIFF), 22 (NET), 23 (ATM), 24 (MLT), 25 (CONV), and 26 (RES) in Appendix B. Looking at these figures, we note that the development of loops for a given mass and metallicity is much less dependent on the properties of the model than in the case without overshooting. Only for the MIX and CONV sets do we notice qualitative differences in loop development for some masses and metallicities.

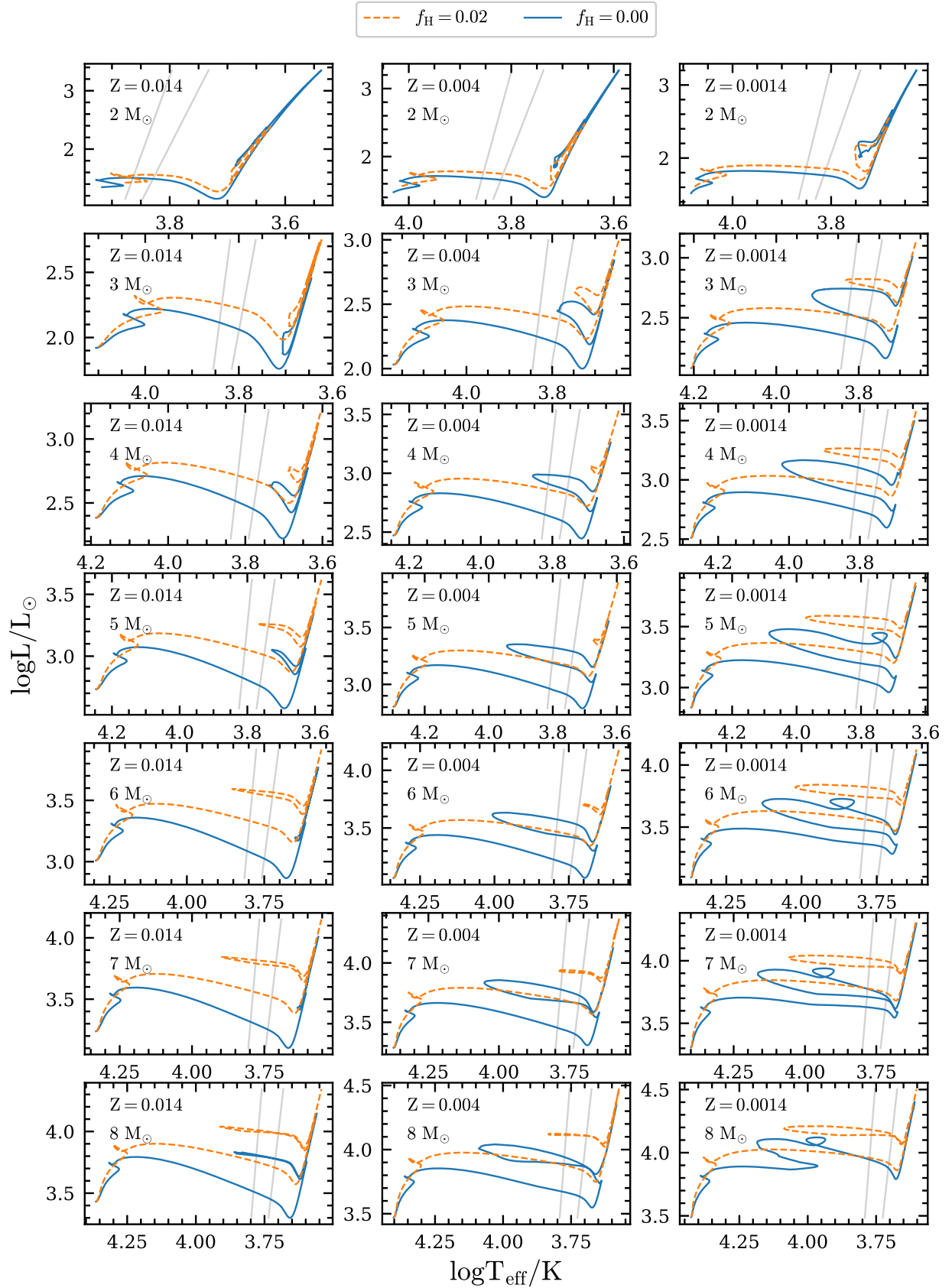


**Figure 4.** Evolutionary tracks of the reference models without convective core overshooting (blue) and with convective core overshooting during the main-sequence phase (orange). Mass and metal contents change in rows and columns, respectively.



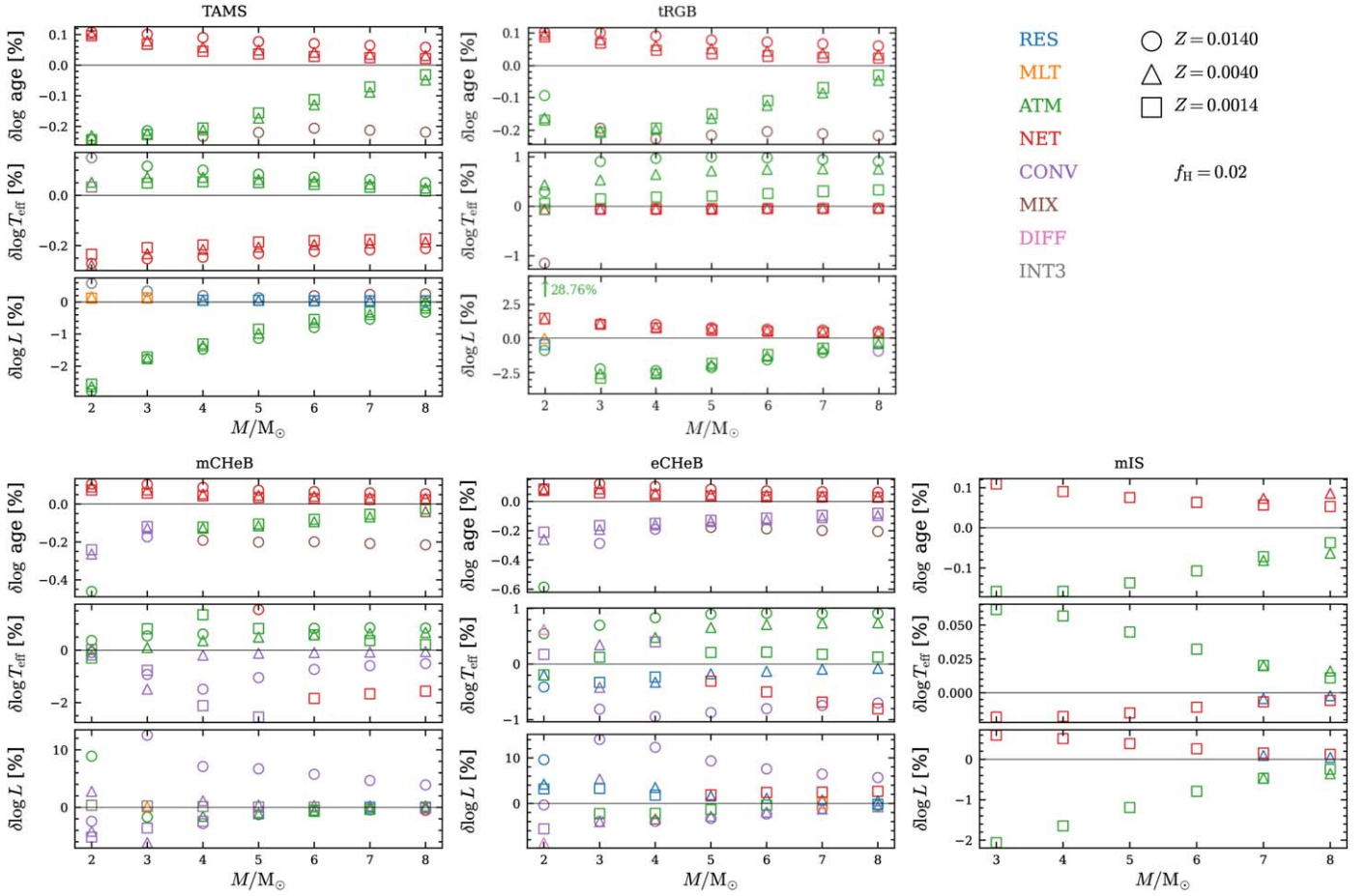


**Figure 5.** Similar to Figure 3, but for models with convective core overshooting during the main-sequence phase. At the tRGB, the  $2 M_{\odot}$ , solar-metallicity model is an outlier, with the value of  $\delta \log L$  noted next to the arrow.

Information on the recorded maximum and minimum relative differences with respect to a reference model, for five benchmark points, is visualized in Figure 5, which is an analog of Figure 3.

In Tables 13–17 in Appendix C (exemplary content illustrated in Table 5) we give the maximum and minimum relative differences of  $\log$  age,  $\log T_{\text{eff}}$ , and  $\log T_{\text{eff}}^{\text{ref}}$  with respect to a reference model taking into account all computed models (from all sets of models considered in the paper including convective core overshooting during the main sequence). The five tables correspond to TAMS, tRGB, mChEB, eChEB, and mIS benchmark points.

Considering all computed models with convective overshooting, typical relative differences for the location on the H-R diagram are around 0.1%–1%, with higher values for later evolutionary phases. The highest relative difference of  $\sim 28\%$  is noted for the luminosity at the tRGB for a  $2 M_{\odot}$ , solar-metallicity model, using the Krishna Swamy  $T$ – $\tau$  relation for the atmosphere model (similarly, significantly brighter tRGB is recorded for solar Hopf and Eddington  $T$ – $\tau$  relations). Log age is not changing by more than  $\sim 0.3\%$  (except for  $2 M_{\odot}$  and solar metallicity, where the change reaches 0.56% for eChEB). What seems to have the largest effect on the tracks, both on age and on location on the H-R diagram, are atmosphere model and nuclear reaction rates during the early evolutionary phases and convective boundary criteria during the later evolutionary phases.

Below we elaborate on the differences recorded within specific sets of models.

### 3.2.1. Interpolation in Opacity Tables, INT

Evolutionary tracks for the INT set with convective core overshooting are plotted in Figure 19 in Appendix B. For all masses and metallicities, the tracks are qualitatively the same. The only noticeable differences are recorded at solar metallicity, just as in the case without core overshoot: the tracks computed with linear interpolation in opacity tables are slightly hotter (up to 0.1% in  $\log T_{\text{eff}}$ ) and more luminous (up to 1.3% in  $\log L$ ), the difference decreasing with increasing mass. The age differences are below  $\sim 0.1\%$ , and they decrease with increasing mass. For the lower metallicities, they are almost negligible.

### 3.2.2. Scaled Solar Abundance, MIX

Evolutionary tracks for models adopting different scaled solar abundances and including convective core overshooting are presented in Figure 20 in Appendix B. Just as for the case without overshoot, for all masses and metallicities the reference solar mixture A09 produces tracks that are slightly more luminous and a bit hotter on the main sequence and with the RGB shifted a bit toward cooler temperatures. For  $2 M_{\odot}$  at solar metallicity the tRGB is significantly brighter for GN93 and GS98; the relative difference with respect to the reference A09 track reaches nearly 24% (GS98). This is the only model



with such a large difference at the tRGB in the MIX set; the relative difference for other models is typically well below 1%. The blue loops seem to be less sensitive to the scaled solar mixture when overshooting is enabled, except for  $Z=0.004$  and higher ( $M \geq 6 M_{\odot}$ ) masses, where loops do not develop for GN93 and GS98 compositions, while they do develop for A09.

Just as for the no-overshooting case, for the log age at solar metallicity (see Figure 5) the use of GN93 leads to the shortest possible log age across all considered models for all evolutionary phases. At TAMS the relative difference with respect to the reference track increases from 0.18% ( $2 M_{\odot}$ ) to 0.22% ( $8 M_{\odot}$ ). This difference remains approximately constant at later evolutionary stages.

### 3.2.3. Diffusion, DIFF

Evolutionary tracks for models computed with and without diffusion and with convective core overshooting are presented in Figure 21 in Appendix B. We note that we were not able to run the  $2 M_{\odot}$ , solar-metallicity model past the initial relaxation phase, due to a problem with the diffusion solver. Just as for the case without overshooting, the tracks nearly perfectly overlap for all masses and metallicities. Maximum relative differences for the location in the H-R diagram never exceed 1% and in nearly all cases are well below 0.1%. The difference in log age is 0.03% at most, and typically it is lower than 0.01%.

### 3.2.4. Nuclear Reactions, NET

Evolutionary tracks for the NET models including convective core overshooting are shown in Figure 22 in Appendix B. Just as for the case without overshoot, the use of `mesa_49.net` does not affect the evolutionary tracks. The tracks divide into two families, with the lower  $^{14}\text{N}(\text{p}, \gamma)^{15}\text{O}$  reaction rate from Cyburt et al. (2010) (NET\_A, NET\_B, and NET\_C) and the higher reaction rate from Angulo et al. (1999) (NET\_D and NET\_E), with the same systematic differences as described for the no-overshooting case. We note, however, that overall the tracks are less sensitive to nuclear reaction rates when overshooting is turned on.

Again, similarly, as for the no-overshooting case, the use of the Angulo et al. (1999) reaction rate leads to the largest values of log age across all computed models and benchmark points (see Figure 5), a consequence of a longer main-sequence evolution. The relative difference in log age is typically around 0.1%. Similarly, for the lowest metallicity,  $Z=0.0014$ , the NET set (specifically the NET\_D model) gives rise to the largest relative differences in the location on the H-R diagram. The tracks are overluminous by up to 2.7% ( $8 M_{\odot}$ ) and a bit cooler (by up to 2.2%) as compared to the reference track. For solar metallicity, the highest difference in log  $L$  appears for  $5 M_{\odot}$ , namely  $\sim 4\%$ . For the mIS, due to the well-constrained effective temperature of this benchmark point, the differences are much smaller. The tracks are overluminous by up to 0.56% ( $3 M_{\odot}$ , difference decreasing with increasing mass) and a bit cooler (but only by up to 0.02%) as compared to the reference track.

### 3.2.5. Atmospheres, ATM

Evolutionary tracks for the ATM set and convective core overshooting are plotted in Figure 23 in Appendix B. We note that for all masses and metallicities the tracks are qualitatively the same, in particular, the occurrence, shape, and extent of the

blue loops are all similar. The noticeable exception is the luminosity of the tRGB for a  $2 M_{\odot}$ , solar-metallicity model, as described at the end of Section 3.2. Systematic differences between tracks increase with the evolutionary stage. Just as for the case without overshooting, we note a significant spread in the location of the RGB in effective temperature, even larger (by a factor of about 2) than for the case without overshooting.

The ATM set frequently gives rise to the extreme differences across all computed models with convective core overshooting for log age and location in the H-R diagram (Figure 5). For log age we record the shortest ages at TAMS, tRGB, and mIS, and for lower-mass models the relative differences are up to  $\sim 0.2\%$ . For nearly all models the benchmark points are the hottest, most often for ATM\_D (solar Hopf). The relative differences vary with mass and metallicity and are on the order of 0.1% at TAMS, up to 1% at the tRGB and CHeB (for solar metallicity; the differences decreasing with decreasing metallicity). For log  $L$  the ATM models are the most underluminous as compared to the reference track, in particular at TAMS and tRGB (the relative differences up to  $\sim 2\%$ , the difference decreasing with increasing mass). At mIS the relative difference decreases from 2% ( $3 M_{\odot}$ ) to  $\sim 0.5\%$  ( $8 M_{\odot}$ ).

### 3.2.6. MLT

Evolutionary tracks for the MLT set and convective core overshooting are plotted in Figure 24 in Appendix B. We note that for all considered masses and metallicities the tracks for various MLT options nearly perfectly overlap. The age is insensitive to the MLT option. At nearly all analyzed benchmark points the relative differences in the location on the H-R diagram are significantly below 0.1%.

### 3.2.7. Boundaries of Convective Regions, CONV

Evolutionary tracks for the CONV set and convective core overshoot are plotted in Figure 25 in Appendix B. In the H-R diagram, we observe qualitatively the same differences between models as for the no-overshooting case. Tracks adopting the sign change algorithm (CONV\_C) differ qualitatively from those adopting PM, in particular, the blue loops either do not develop or are significantly shorter and narrower in luminosity. Differences are also apparent when comparing models adopting PM at the core, although they are much less pronounced and develop only after tRGB. Still, for a few cases, in particular at solar metallicity, whether the loop develops depends on what specific criterion, Schwarzschild or Ledoux, was applied in the model. Again we stress that this difference arises as a result of the sign change algorithm used at the convective envelope boundary.

As evidenced in Figure 5, models from the CONV set often give rise to the largest recorded differences in the location on the H-R diagram during CHeB. At solar metallicity, the differences in log  $L$  may reach more than 10% but result from a qualitative difference between tracks (loop vs. no loop). The differences decrease with decreasing metallicity.

### 3.2.8. Spatial and Temporal Resolution, RES

Evolutionary tracks for the RES set and convective core overshoot are plotted in Figure 26 in Appendix B. For all masses and metallicities, the tracks nearly overlap: the differences are much smaller than for the no-overshooting

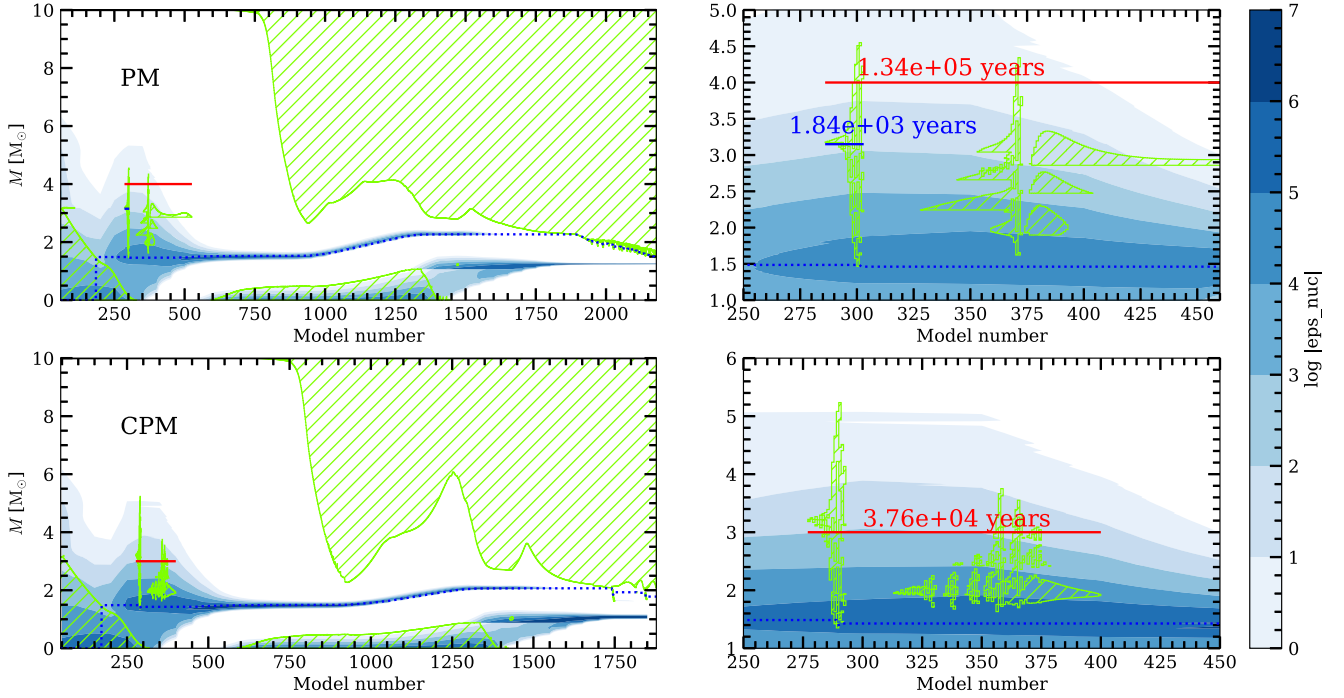


**Figure 6.** The Kippenhahn diagrams for  $10 M_{\odot}$ ,  $Z = 0.014$  models with convective boundaries computed using PM (top) and CPM schemes (bottom panel). The left panels illustrate full evolution, from ZAMS until AGB ascent, while the right panels show zoomed-in views illustrating the development of thin convective shells at the end of main-sequence evolution. Convective regions are marked with green hatched areas. Blue shaded areas indicate regions of strong nuclear burning, with efficiency color coded (scale on the right side).

case. In the majority of cases and benchmark points, relative differences in log age are on the order of 0.01%, and for the location in the H-R diagram they are typically well below 0.1%. Larger differences, on the order of 1% for log  $L$ , are only recorded at eChEB.

### 3.3. Dealing with Thin Convective Shells in High-mass Models, 9–15 $M_{\odot}$

The results for higher-mass models, 9–15  $M_{\odot}$ , are qualitatively different than for the low-mass models. This is best illustrated with H-R diagrams presented in Figure 27 in Appendix B for the RES set. We do not include H-R diagrams of the remaining sets; instead, we store them in an online archive. In most of the cases, tracks computed for a given mass and metallicity, and under different assumptions comprising our model sets, diverge as soon as hydrogen is depleted in the core. While for the main-sequence phase we observe a good convergence of all tracks, for the subsequent evolutionary phases the model may follow very different paths, with different luminosity levels on the way to the RGB and with different scenarios during CHeB (helium ignition on the way to the RGB, blue-loop and no-loop evolution). Figure 27, exploring various spatial and temporal resolution controls, clearly shows that the models are not converged. Even when going to a very fine spatial and temporal resolution (e.g., with `mesh_delta_coeff` and `time_delta_coeff` set to 0.1; see Figure 7), convergence is not reached. The computed tracks clearly indicate that the issue arises at the very end of the main sequence, at the Henyey hook, where most massive models develop peculiar, erratic tracks.

Inspection of the internal structure of the massive models ( $M \geq 9 M_{\odot}$ ) shows that as soon as hydrogen gets depleted in the core, thin convective shells start to develop at a mass coordinate that corresponds to the maximum extent of the convective core during the main-sequence evolution, a location at which the radiative temperature gradient develops a local maximum. This is also a location at which nuclear burning of hydrogen occurs, initially over a relatively large mass extent, to finally narrow to a thin shell over the helium-burning core at later stages of evolution—see the Kippenhahn diagram in Figure 6. At the end of the main-sequence evolution, for masses above  $9 M_{\odot}$ , the cusplike maximum of  $\nabla_{\text{rad}}$  pierces above  $\nabla_{\text{ad}}$  and the first thin shell develops. In the following, shells develop over a much larger mass range in an apparently erratic manner (see the zoomed-in view in the right panel of the Kippenhahn diagram in Figure 6). Still, the whole mass extent covered with the shells is typically well below  $1H_p$ , the extent of individual shells, and with gaps in between being a small fraction of  $H_p$ . The appearance of shells during the evolution is robust, i.e., it is not a consequence of too coarse spatial/temporal resolution. The overall phase at which shells are present is very short ( $1.34 \times 10^5$  yr for the case illustrated in the top panel of Figure 6).

The erratic nature of shells implies that their appearance and temporal evolution are extremely sensitive to the numerical setup of the models: spatial and temporal resolution, convective stability criterion adopted (Ledoux vs. Schwarzschild), or numerical treatment of the convective shells. In fact, getting converged models (by which we mean models for which the position and size of the shells do not change with further increasing resolution) may not be possible by just increasing spatial and temporal resolution. As a consequence, the chemical

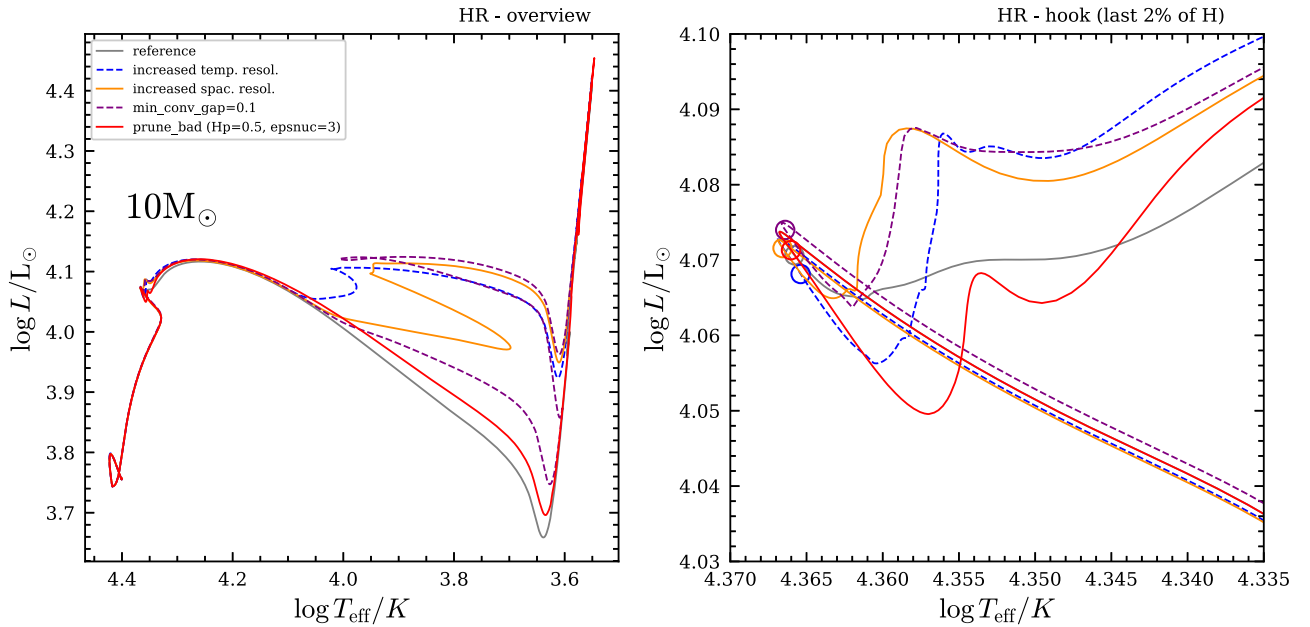


**Figure 7.** Left panel: the H-R diagram with evolutionary tracks for the  $10 M_{\odot}$ ,  $Z = 0.014$  model computed under various assumptions as given in the key. Right panel: zoomed in around the Henyey hook, with circles marking the appearance of the first thin convective shell.

profile left, once the shells cease to exist, may be vastly different, which in turn affects the following evolution. We illustrate the point with the H-R diagram in Figure 7 showing evolutionary tracks for  $10 M_{\odot}$ , solar-metallicity models under different numerical settings. While for all setups main-sequence evolution follows the same track, as soon as shells develop, tracks start to diverge, which is well visible at the Henyey hook (right panel of Figure 7). Noticeably, the post-main-sequence evolution may be entirely different, with differences as drastic as having an extended blue loop during CHeB, no loop at all, or starting CHeB on the way to the RGB.

Most of these high-mass models do not form a blue loop, which would correspond to long-period Cepheids having predominantly positive period change rates. Csörnyei et al. (2022) show a relation between period change rate and position on the color–magnitude diagram but only for stars with short periods (2–5 days). Rodríguez-Segovia et al. (2022) found a similar number of negative (572) and positive (696) period change rates. Looking at their Figure 3, there is no clear indication that the high-mass, long-period models favor the redward evolution.

We considered three approaches to make evolution more robust (for corresponding tracks for the  $10 M_{\odot}$ ,  $Z = 0.014$  model see Figure 7). In the first approach, we tried to eliminate the convective shells (considering that they are a transient phenomenon in which convective energy transfer and mixing cannot be efficient). The controls that are implemented in MESA for that purpose (`prune_bad_cz_min_Hp_height` and `prune_bad_cz_min_log_eps_nuc`), with reasonable values, only delay the appearance of the shells, however, and lead to an unpleasant scenario with a large radiative but convectively unstable region.

In the second approach, it is desirable to obtain a single large convective shell. For this purpose, the control to close small gaps in between adjacent convective regions seems promising (`min_convective_gap`). By closing small convective gaps, the problem may only be reduced, however. By increasing the `min_convective_gap` (above  $0.1H_p$ – $0.2H_p$ ), the shells ultimately merge with the vanishing core, producing a

sequence of breathing pulses, with hydrogen injected into the core (in analogy to abrupt convective core extensions at the end of CHeB). Similarly, adding overshooting at the shell boundaries does not cause the shells to merge. Overshooting at the edge of the hydrogen-burning core, on the other hand, reduces the radial extent of the region occupied with shells, but their erratic nature is preserved.

In the third approach, we employed the CPM scheme to determine the boundaries of convective regions. CPM has the advantage of correctly setting  $\nabla_{\text{rad}} = \nabla_{\text{ad}}$  on the convective side of the boundary, also for convective shells; see Paxton et al. (2019). As mentioned in Section 2.2.6, CPM is broken in version r21.12.1 that we use. It was fixed, however, with r-22.05.1, and we used that version to apply CPM to our shell problem. Unfortunately, using CPM is not a solution—thin shells do develop in an erratic manner, just as for other schemes of setting the convective boundaries. This is illustrated with the Kippenhahn diagram in the bottom panel of Figure 6.

Just as for the lower masses, we repeated all calculations with moderate convective core overshooting ( $f = 0.02$ ) during the main-sequence phase. As already mentioned, this does not solve the thin-shell problem but reduces the radial extent of the shell region. The H-R diagrams for the RES set and with main-sequence core overshooting are presented in Figure 28 in Appendix B. We notice a significant improvement in convergence as compared to the no-overshooting case, in particular for the 9–11  $M_{\odot}$  models, for which various tracks follow, with several exceptions, qualitatively the same evolutionary scenario. For larger masses,  $M \geq 12 M_{\odot}$ , qualitatively different evolution (e.g., helium ignition on the way to the RGB vs. at the tRGB, loop vs. no-loop evolution) is much more frequent, which is a consequence of the thin-shell episode at the end of the main sequence.

In practice, whether overshooting is included or not, for  $M \geq 9 M_{\odot}$  a careful inspection of Kippenhahn diagrams and convergence study is needed to assess how severe the thin-shell problem is for a given mass and metallicity, as well as to what extent it may affect the subsequent evolution. For this reason, we do not discuss the relative differences between tracks at

benchmark points, as in the majority of cases these may arise as a result of the thin-shell problem and thus are not robust.

The problem described above has not been discussed in the literature before. Anderson et al. (2016) and Miller et al. (2020) present Cepheid models computed with the Geneva code (Ekström et al. 2012; Georgy et al. 2013) and the BEC code (Yoon & Langer 2005), respectively; however, they do not raise the issue of the high-mass tracks. In addition, they do not present and study the internal structure of the models. Similarly, Morel et al. (2010) studied the effect that an enhanced triple- $\alpha$  reaction rate had on Cepheid models computed with the CESAM code. While some of their tracks show similar post-main-sequence evolution to that of most of our high-mass tracks (i.e., show no blue loop), their models are less massive, and specific evolution is due to the enhanced triple- $\alpha$  rate. The authors do not mention any problems related to the development of thin shells. It would be interesting to compare the tracks produced by different evolutionary codes, but this is beyond the scope of this paper.

#### 4. Discussion

Most of the work on stellar evolution explores the effects of macrophysical phenomena on evolution, such as overshooting from the convective regions, mass loss, or rotation, across a grid of stellar masses and compositions. Indeed, these phenomena have a large impact on stellar evolution and may affect age, luminosity, and effective temperature by some tens of percent. Still, tens of other assumptions and choices underlie every evolutionary calculation. They concern numerical convergence, material properties, or supplementary relations. We have investigated several options that MESA offers for some of these key yet *secondary* components of the evolutionary model, such as the choice of the mixing-length prescription or atmospheric boundary condition. There are several possible options in the literature. However, for many of these model ingredients, there are no generally recognized, physically motivated choices; the choice of a particular option depends on authors' preference. It is generally assumed that the choice of a particular option for these components has a secondary effect on evolution, but this has rarely been verified. One of the goals of this work was to find out exactly whether and how much these choices affect the evolutionary tracks.

##### 4.1. Factors that Matter Little, Factors that Matter More

The choice of spatial and temporal resolution controls is one of the most important for stellar evolutionary calculations. The specific choice usually represents a trade-off between numerical cost and computational convergence. Our choice of resolution controls (Section 2.4) ensures the convergence of calculations and relatively fast computation time. In our case, convergence means that for the majority of masses and metallicities and through all considered evolutionary phases relative differences between the reference track and tracks with increased spatial and/or temporal resolution are on the order of 0.01% for log age and are typically well below 0.14% for the location in the H-R diagram.

While linear interpolation in opacity tables is numerically less expensive, it leads to noticeable differences in evolutionary tracks as compared to cubic interpolation, in particular at solar metallicity. Sometimes, these differences are the largest across all models we have computed. For the lower metallicities, the

differences are much smaller. We recommend using the more accurate cubic interpolation when using MESA, just as we have adopted in our reference models (note that this is not the default setting in MESA).

The choice of MLT option has the least impact on evolutionary tracks that nearly perfectly overlap whatever option is used. We remind, however, that calibration of  $\alpha_{\text{MLT}}$  for a specific option of choice is needed.

Whether diffusion is included in the model or not is not an arbitrary choice, but it depends on application. No doubt, including diffusion is crucial for all applications that focus on detailed chemical abundance evolution and for solar model calibration (Dotter et al. 2017). Since it is numerically very expensive, some studies (Miller et al. 2020; Hecdé et al. 2024) for which detailed abundances are of lower importance ignore it. Our calculations provide support for such an approach: evolutionary tracks in the H-R diagram nearly perfectly overlap, whether diffusion is included or not. Since chemical abundances are of lower importance for our further investigations, we have ignored the diffusion in our reference model.

There are several options available to treat most external model layers; either photosphere tables are used, based on more advanced numerical simulations, or one of a few  $T$ - $\tau$  relations is adopted. There is no common agreement on the best possible choice. We decided to use data for atmosphere tables (see Section 2.2.5). Our calculations show that as long as calibration of the mixing length is conducted the tracks in the H-R diagram are qualitatively similar, but with some noticeable shifts. We note strong sensitivity of the temperature location of the RGB, decreasing with decreasing metallicity. While the shapes of the loops are generally the same, luminosity levels may slightly differ (by up to 2% in log  $L$ ). Interestingly, the latter is most pronounced when overshooting from the main-sequence convective core is included in the model and is noticeable for all phases of evolution, starting from the main sequence.

The photospheric composition of the Sun, which is used as a reference to scale heavy-element abundances in evolutionary calculations, is still debated (see Section 2.2.1). Consequently, there is no commonly accepted option for solar composition, and different ones are used in the literature. We have adopted A09 for our reference model, which is the most recent solar mix implemented in the MESA version we use, and which is implemented consistently when it comes to opacity tables, including the low-temperature ones and type II opacities. The choice of solar composition has a significant impact on the computed tracks, noticeable already during main-sequence evolution but most pronounced during CHeB and at solar metallicity. Whether the blue loop develops or not may depend on the adopted option for solar composition. At lower metallicities, the extent of blue loops does depend on solar composition. These differences are not as pronounced when overshooting is used; however, they are still noticeable.

The determination and proper implementation of criteria to determine the convective boundary locations is one of the most challenging problems of stellar evolution (see, e.g., Gabriel et al. 2014; Paxton et al. 2018, 2019; Anders et al. 2022a). For our reference model, we have adopted the PM scheme at the core with the Schwarzschild criterion. The CPM scheme introduced later in MESA seems superior, but PM is much better at suppressing breathing pulses at the end of CHeB, which motivated our choice. While we have investigated the sign change algorithm for the core convection, we note that its use



leads to incorrect placement of the convective core boundary, as analyzed in Paxton et al. (2018). It also leads to qualitatively different blue loops as reported in Section 3. Neglecting this option and considering others we have tested (a different scheme at envelope convection boundary, Schwarzschild vs. Ledoux), the evolutionary tracks either agree very well or, for some specific mass and metallicity, may even differ qualitatively: whether the blue loop develops or not may depend on the scheme used. This is particularly true for solar-metallicity models and models with intermediate metallicity and convective core overshooting. We also note that the problem of correctly setting the boundaries of convective regions is crucial for high-mass models; see Section 3.3 and later in the discussion.

Finally, concerning the nuclear reaction network, we first note that changing the nuclear net to a more extensive one, with 49 elements and their reactions, `mesa_49.net`, labeled as `NET_B`, does not affect evolutionary tracks in any essential way. Taking into account the huge overhead of computation time, connected to following the evolution of more elements, the use of a limited network, `pp_and_cno_extras.net` with 25 elements, is well justified in particular for applications that do not require knowledge about many elements.

On the other hand, the specific reaction rates, in particular the  $^{14}\text{N}(p, \gamma)^{15}\text{O}$  reaction rate, matter a lot. This slowest reaction in the CNO chain not only affects the main-sequence evolution (ages and brightness of the tracks) but also significantly affects all subsequent phases including CHeB, having a strong impact on the development of blue loops, in particular at solar metallicity. The lower reaction rate from Cyburt et al. (2010) leads to brighter main-sequence evolution and shorter blue loops as compared to the reaction rate from Angulo et al. (1999). The differences in tracks computed with these two reaction rates are much less pronounced when moderate main-sequence core overshooting is used. Still, the choice of specific reaction rate may have a strong impact on the evolutionary properties of classical Cepheid models.

The rate for  $^{12}\text{C}(\alpha, \gamma)^{16}\text{O}$  reaction matters only during and after CHeB. At solar metallicity, the blue loops for tracks adopting the Kunz et al. (2002) reaction rate may be shorter than for tracks adopting the Angulo et al. (1999) rate. At lower metallicities, the blue loops computed with these two reaction rates closely follow each other, with no significant differences. Clearly, the C/O composition of the core is affected, with the Kunz et al. (2002) reaction rate leading to higher  $^{12}\text{C}$  and lower  $^{16}\text{O}$  content.

#### 4.2. Uncertainties of Evolutionary Tracks

Our overall goal is to quantify the uncertainties on evolutionary tracks due to the adopted choice of parameters we have called secondary. These include some numerical choices (interpolation in opacity tables, spatial and temporal resolution), microphysics choices (nuclear reaction rates, reference solar composition, diffusion), and auxiliary relations (atmosphere model, MLT version, scheme to determine convective boundaries). We note that there are other factors that we have not studied, which may lead to similar differences in the H-R diagram. These are in particular the source of opacity tables, the EOS, and various settings available for numerical solvers. For intermediate-mass stars, the source of opacity tables seems most important. In our calculations, we used OPAL opacities only, as these are consistently

implemented for type I and type II opacities and various reference solar compositions we have adopted. The calculation of opacity, however, is one of the most actively developing fields (e.g., Bailey et al. 2015; Iglesias 2015; Colgan et al. 2016), and several studies indicate a need for improvement in opacity tables (e.g., Christensen-Dalsgaard et al. 2009; Daszyńska-Daszkiewicz et al. 2023a).

Our study shows that the different choices we have adopted affect the evolutionary tracks to a different degree: from negligible to significant effect. The differences between 23 evolutionary tracks computed under different assumptions for each  $M/Z$  do depend on  $M$  and  $Z$  and whether convective core overshooting is included in the model or not. The recorded differences were sometimes qualitative (e.g., blue loop was developed or not), but in the majority of cases we observed small shifts. The maximum recorded relative differences, with respect to the reference model, we elaborated on in Section 2 were presented in Figure 3 (for the no-overshooting case) and in Figure 5 (for the case with moderate convective core overshooting included). Based on the recorded relative differences, we quantitatively assess the *uncertainty* of the evolutionary tracks at different evolutionary phases.

Since we rarely see clear and strong trends with mass (see Section 3), we decided to quantify the uncertainty of the evolutionary tracks (i) separately for each benchmark point; (ii) separately for the case without and with convective core overshooting; (iii) based on statistics of the recorded maximum differences for all 23 evolutionary tracks computed for a given  $M$  and  $Z$ ; (iv) ignoring the sign of the difference and just considering the maximum, which we motivate by the freedom to choose a different reference track than we did; (v) ignoring mass dependence and computing, at each benchmark point, the relative difference distribution for  $\log$  age,  $\log L$ , and  $\log T_{\text{eff}}$  for  $23 \times 7$  models (seven mass values); and finally (vi) choosing the median to give a quantitative assessment of the uncertainty.

The results are presented in Figure 8 for the case without convective core overshooting (left panel) and with moderate convective core overshooting (right panel). The median, plotted with a solid line, is enclosed with a shaded region indicating the 25th and 75th percentiles. Three different colors refer to three different metallicities. Note that the mIS benchmark point is not included along the horizontal axis, as this point remains undefined for cases that do not develop blue loops. Instead, results for mCheB may be regarded as indicative also for mIS.

We observe the following: (i) The metallicity dependence is clear. With small exceptions, the higher the metallicity, the larger the uncertainties of evolutionary tracks at all benchmark points. The exception is the CHeB phase (in the no-overshooting scenario), at which uncertainties for the location in the H-R diagram for  $Z=0.004$  (intermediate metallicity considered) are the largest. (ii) With the exception of  $\log$  age at the main sequence (uncertainties are the largest), the uncertainties increase with the evolutionary phase. (iii) Comparing models without and with moderate convective core overshooting (left and right panels of Figure 8, respectively), we notice a slightly increased overall level of uncertainty in the models with overshooting. (iv) For  $\log$  age, the uncertainty is the highest on the main sequence. Then, it decreases and either remains approximately constant (when overshooting is enabled) or increases during CHeB (no-overshooting case). (v) For the effective temperature, we see a clear increase by a

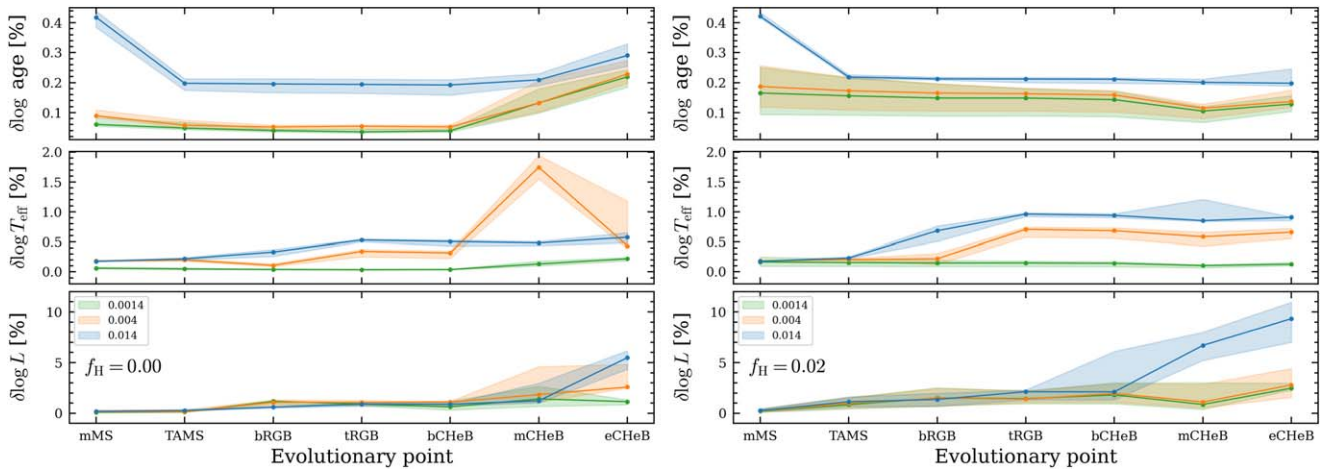


**Figure 8.** Median (solid line) along with 25th and 75th percentiles (colored regions) for the maximum recorded relative difference distributions for log age (top panels), log  $T_{\text{eff}}$  (middle panels), and log  $L$  (bottom panels) at progressing evolutionary phases (horizontal axis). The three colors correspond to three metallicities. The left panels correspond to models computed without convective core overshooting, while in the right panels we show results for models computed with convective core overshooting. At each benchmark point statistics are drawn from a set of 23 evolutionary models computed under different assumptions for seven mass values (2–8  $M_{\odot}$ ).

factor of 2–3 in the uncertainty after the main sequence for solar and intermediate metallicity. For the lowest metallicity, the uncertainty in log  $T_{\text{eff}}$  remains low and constant (for the case with overshooting) or slightly increases during CHeB (no-overshooting case). (vi) For the absolute luminosity, we observe an increase of the uncertainty after the main-sequence evolution and later during the CHeB.

If we further ignore the dependence on metallicity and compute the relative difference distributions for all models at a given benchmark point, dividing these only into two groups, without and with convective core overshooting, we arrive at Figure 9 (and Table 6). Just as in Figure 8, we plot the median with a region encompassing the 25th and 75th percentiles. The blue and orange regions correspond to models computed without and with convective core overshooting, respectively. We observe similar trends for the two cases as the evolutionary stage progresses. For log age, we observe the highest uncertainty at the main sequence and then a plateau and increase during CHeB. Uncertainty for both the effective temperature and absolute luminosity increases with the progressing evolutionary phase, with those for models with convective core overshooting being slightly larger than for the case without convective core overshooting.

Quantitative data are collected in Table 6, and the collected median values are our recommended estimates for uncertainties at different evolutionary stages.

For log age, the uncertainty is small, 0.1%–0.3% depending on the evolutionary phase (larger during the main sequence) and whether overshooting was included or not. For the location in the H-R diagram  $\delta \log T_{\text{eff}} / \delta \log L$  we get 0.2/0.2% for both mMS and TAMS, 0.2/0.8% for tRGB, and 0.8/1.6% for mCHeB, for the case without convective core overshooting. Corresponding numbers for the overshooting case are 0.2/0.2% (mMS), 0.2/1.0% (TAMS), 0.3/1.5% (tRGB), and 0.8/3.6% (mCHeB).

The uncertainty in the luminosity level at the mIS is significantly lower as compared to mCHeB and is 0.5% and 0.6% without and with overshooting, respectively. This is because this benchmark point is very well localized in the H-R diagram at the intersection of evolutionary tracks with a nearly vertical mIS line. In practice, this sets the effective temperature

of this point to a nearly constant value at a given  $M$  and  $Z$ , independent of the evolutionary track considered. At this very restricted range of effective temperatures, the differences in luminosity are significantly smaller than for mCHeB.

#### 4.3. Uncertainties for Detached Eclipsing Binaries

To estimate the observed position uncertainties in the H-R diagram, we use DEBCat (Southworth 2015), which is a catalog of detached eclipsing binary stars containing data for 195 systems, both from the Galaxy and from the Magellanic System. The catalog contains luminosity and effective temperature determinations with their uncertainties. We have selected systems containing stars in the 2–15  $M_{\odot}$  range. Metallicity estimates are available for half of this sample, and the average metallicity is  $[\text{Fe}/\text{H}] \approx -0.4$ . We plotted the stars on the H-R diagram in Figure 10 and divided them into two groups based on their effective temperature: hotter than  $\log T_{\text{eff}} = 3.85$  K (mostly main-sequence stars) and cooler helium-burning and RGB stars. We present the median uncertainties of luminosity, effective temperature, and mass in Table 7.

The theoretical uncertainties for log  $L$  estimated in this work, arising only as a result of *secondary* parameters, are either much smaller than the observed ones (for the main sequence) or of the same order as or even larger than the observational ones for later evolutionary stages (Table 7). Consequently, these uncertainties cannot be ignored when eclipsing binary systems are modeled with the goal to constrain *primary* parameters, such as the extent of convective core overshooting, and may significantly contribute to the error budget. The use of detached eclipsing binaries for the purpose of calibrating the extent of convective core overshooting and/or other parameters of the evolution theory is a difficult task and requires further strong reduction of observational errors and careful statistical analysis (see, e.g., Constantino & Baraffe 2018; Valle et al. 2018).

#### 4.4. High-mass ( $M \geq 9 M_{\odot}$ ) Models

As we have analyzed in Section 3.3, the set of controls in MESA (r21.12.1) does not allow us to properly treat the convective shells at the end of the main-sequence life of

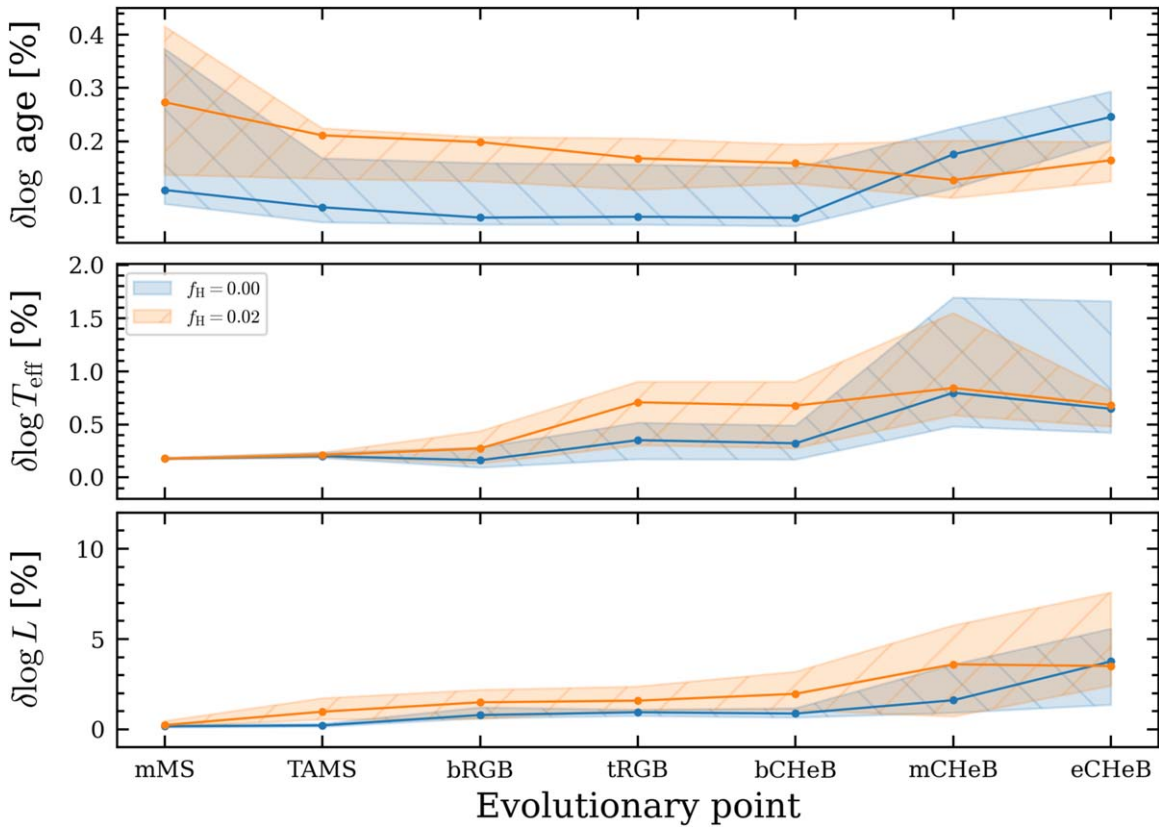


**Figure 9.** Similar to Figure 8, but here we present the median along with the 25th and 75th percentiles for  $2-8 M_{\odot}$  models and three metallicities. The two colors correspond to models with (orange right-slanted lines) and without convective core overshooting (blue left-slanted lines). Numerical data are collected in Table 6.

massive ( $M \geq 9 M_{\odot}$ ) stars. While these shells appear for a very short time, their erratic nature adds a random component for subsequent evolution. Tracks computed with slightly different settings (e.g., with altered spatial and temporal resolution) may significantly differ during subsequent evolutionary phases. Often we could not reach convergence. Still, the model's behavior may depend on specific mass, specific metallicity, and whether overshooting is included or not. For massive models, we stress the need to investigate the convective structure of the model (e.g., through Kippenhahn diagrams), its evolution, and effects on subsequent evolution. More detailed and careful convergence studies are also needed. In particular, convergence studies should be carefully conducted across a range of masses and metallicities. First of all, however, our results call for further improvement in the schemes used to determine convective boundaries.

The lack of robust high-mass models poses a difficulty for problems related to classical Cepheid evolution. Fortunately, the majority of classical Cepheids are expected to have much lower masses as indicated by the scarcity of very long period Cepheids (e.g., Ulaczyk et al. 2013; Soszyński 2024).

## 5. Summary and Conclusions

We have used MESA, version r21.12.1, to calculate a grid of stellar evolutionary models with  $2-15 M_{\odot}$  (step  $1 M_{\odot}$ ) and with three different metallicities,  $[\text{Fe}/\text{H}] = -1.0$ ,  $-0.5$ , and  $0.0$ . Rotation and mass loss were not considered, while convective overshooting was either disabled or included for hydrogen-burning core. We first defined a reference model, and then, for each mass and metallicity and for a case without and with

convective core overshooting, we have computed 22 additional models under different assumptions regarding opacity interpolation scheme, reference solar composition, atomic diffusion, nuclear reaction rates, atmospheric boundary condition, MLT, convective boundaries, and spatial and temporal resolution. While many options are usually available (e.g., for the MLT variant we considered four of the options available in MESA), the underlying parameters are typically fixed in most of the studies. Often, there are no solid physical arguments behind a specific option; selection depends on authors' preference. Our goal was to determine the impact of these parameters on evolutionary tracks. This impact is sometimes barely noticeable, but for some of the options significant shifts and even qualitative differences in evolutionary tracks were recorded. We consider that these shifts and differences build up an *uncertainty* of the evolutionary track that we have quantitatively assessed. Our main findings are the following:

1. Among factors that little affect evolutionary tracks we may list spatial and temporal resolution of the model, given that the convergence study is conducted first and corresponding numerical controls are set to ensure convergence. Similarly, the scheme to interpolate in opacity tables does not affect the tracks significantly; however, slight differences are noticed, and we recommend using more accurate cubic interpolation. The choice of the MLT variant seems to have the least impact on evolutionary tracks (given that calibration of the underlying  $\alpha_{\text{MLT}}$  parameter is conducted). While diffusion clearly matters for surface abundances, it little affects the actual run of the evolutionary tracks.



**Table 6**

25th, 50th (Median), and 75th Percentiles of the Maximum Relative Difference Distributions across All Models Computed in This Study (All Masses, Metallicities, and Parameter Sets) for the Case without Convective Core Overshooting and with Convective Core Overshooting for Eight Evolutionary Phases

Evolutionary Phase	No Overshooting			MS Core Overshooting		
	25th	Median	75th	25th	Median	75th
$\delta \log \text{age}$						
mMS	0.1	<b>0.1</b>	0.4	0.1	<b>0.3</b>	0.4
TAMS	0.0	<b>0.1</b>	0.2	0.1	<b>0.2</b>	0.2
tRGB	0.0	<b>0.1</b>	0.2	0.1	<b>0.2</b>	0.2
bRGB	0.0	<b>0.1</b>	0.2	0.1	<b>0.2</b>	0.2
bCHeB	0.0	<b>0.1</b>	0.1	0.1	<b>0.2</b>	0.2
mCHeB	0.1	<b>0.2</b>	0.2	0.1	<b>0.1</b>	0.2
eCHeB	0.2	<b>0.2</b>	0.3	0.1	<b>0.2</b>	0.2
mIS	0.1	<b>0.1</b>	0.2	0.1	<b>0.1</b>	0.1
$\delta \log T_{\text{eff}}$						
mMS	0.2	<b>0.2</b>	0.2	0.2	<b>0.2</b>	0.2
TAMS	0.2	<b>0.2</b>	0.2	0.2	<b>0.2</b>	0.2
tRGB	0.1	<b>0.2</b>	0.3	0.1	<b>0.3</b>	0.4
bRGB	0.2	<b>0.4</b>	0.5	0.3	<b>0.7</b>	0.9
bCHeB	0.2	<b>0.3</b>	0.5	0.3	<b>0.7</b>	0.9
mCHeB	0.5	<b>0.8</b>	1.7	0.6	<b>0.8</b>	1.5
eCHeB	0.4	<b>0.6</b>	1.7	0.5	<b>0.7</b>	0.8
mIS	0.0	<b>0.0</b>	0.0	0.0	<b>0.0</b>	0.0
$\delta \log L$						
mMS	0.1	<b>0.2</b>	0.3	0.1	<b>0.2</b>	0.5
TAMS	0.1	<b>0.2</b>	0.3	0.5	<b>1.0</b>	1.7
tRGB	0.6	<b>0.8</b>	1.2	0.6	<b>1.5</b>	2.2
bRGB	0.7	<b>0.9</b>	1.1	1.1	<b>1.6</b>	2.4
bCHeB	0.6	<b>0.9</b>	1.2	1.1	<b>2.0</b>	3.2
mCHeB	0.9	<b>1.6</b>	3.6	0.7	<b>3.6</b>	5.7
eCHeB	1.3	<b>3.8</b>	5.6	2.4	<b>3.5</b>	7.6
mIS	0.3	<b>0.5</b>	0.8	0.4	<b>0.6</b>	1.3

**Note.** Graphical visualization is presented in Figure 9. The medians are given in bold.

2. The choices for atmosphere model, reference solar composition, nuclear reaction rates, and scheme to determine convective boundaries can have a much stronger impact on evolutionary tracks. Various choices for underlying parameters lead to small but noticeable shifts between tracks. Qualitative differences are often recorded at solar metallicity. During earlier evolutionary phases, the choice for the atmosphere boundary condition impacts the temperature location of the RGB. For the nuclear reaction rates, we observe a strong dependence on the rate adopted for  $^{14}\text{N}(p, \gamma)^{15}\text{O}$ , the slowest reaction in the CNO cycle, which affects not only the main sequence but also subsequent evolution. In particular, the use of Cyburt et al. (2010) rate leads to a brighter main-sequence phase of shorter duration. The choice of criteria to determine convective boundaries does not affect main-sequence evolution but impacts the CHeB phase.
3. The abovementioned factors, atmosphere boundary condition, reference solar composition, nuclear reaction rates, and convective boundary scheme do affect the CHeB phase and properties of the blue loops. The choice for the atmosphere model may affect the luminosity level

of the blue loop by up to 2% (in  $\log L$ ). At solar metallicity, whether the blue loop develops or not may depend on the adopted reference solar composition, with older mixtures (Grevesse & Noels 1993; Grevesse & Sauval 1998) favoring longer loops. The use of the Cyburt et al. (2010) rate for  $^{14}\text{N}(p, \gamma)^{15}\text{O}$  leads to much shorter, reduced loops that do not enter the IS, as compared to the Angulo et al. (1999) rate. Also at solar metallicity, we observe some sensitivity to criteria setting the convective boundaries. Considering the PM scheme only, whether the loop develops or not may depend on whether the Schwarzschild or Ledoux criterion was used if one does not include PM in the envelope.

4. The largest differences among computed tracks are recorded at solar metallicity and get smaller as metallicity decreases. Consequently, the uncertainty of the evolutionary tracks depends on metallicity and decreases with decreasing metallicity. The inclusion of convective core overshooting during main-sequence evolution also contributes to magnifying the differences among computed tracks. Recorded differences and hence uncertainty of the tracks are slightly larger when overshooting is included.
5. To get a rough assessment of the tracks' uncertainty, we decided to ignore mass and metallicity dependence and use the distribution of the maximum recorded differences with respect to a reference track at a few defined evolutionary phases. These results are summarized in Figure 9 and in Table 6. Using the median to characterize the uncertainty, we note that uncertainty in  $\log \text{age}$  is small, 0.1%–0.3% depending on evolutionary phase and whether overshooting was included or not. For the location in the H-R diagram  $\delta \log T_{\text{eff}}/\delta \log L$  we get 0.2/0.2% for TAMS, 0.2/0.8% for tRGB, and 0.8/1.6% for mCHeB, for the case without convective core overshooting. Corresponding numbers for the overshooting case are 0.2/1.0% (TAMS), 0.3/1.5% (tRGB), and 0.8/3.6% (mCHeB). The uncertainty in the luminosity level at the mIS is much lower as compared to mCHeB and is 0.5% (without overshooting) and 0.6% (with overshooting). This is because this benchmark point is well localized in the H-R diagram at the intersection of evolutionary tracks with a nearly vertical mIS line, which in practice sets the effective temperature of this point to nearly constant at given  $M/Z$ , independent of evolutionary track considered.
6. For stars observed in detached eclipsing binaries from DEBCat (Table 7) the median uncertainties in  $\log T_{\text{eff}}/\log L$  are 0.3/2.2% for main sequence and 0.2/1.3% for helium-burning phase. While for main-sequence stars observed uncertainty in  $\log L$  is significantly larger than uncertainty in evolutionary tracks we have estimated in this study, for later evolutionary stages it is of the same order or even lower. Consequently, uncertainties due to secondary parameters cannot be disregarded in the error budget when one attempts to constrain primary parameters, such as the extent of convective core overshooting, through modeling of detached eclipsing binary systems.
7. For masses  $M \geq 9 M_{\odot}$  we no could longer assure convergence. Small differences in resolution controls or in other parameters that had no strong effect on tracks for lower-mass models led to significantly, often qualitatively



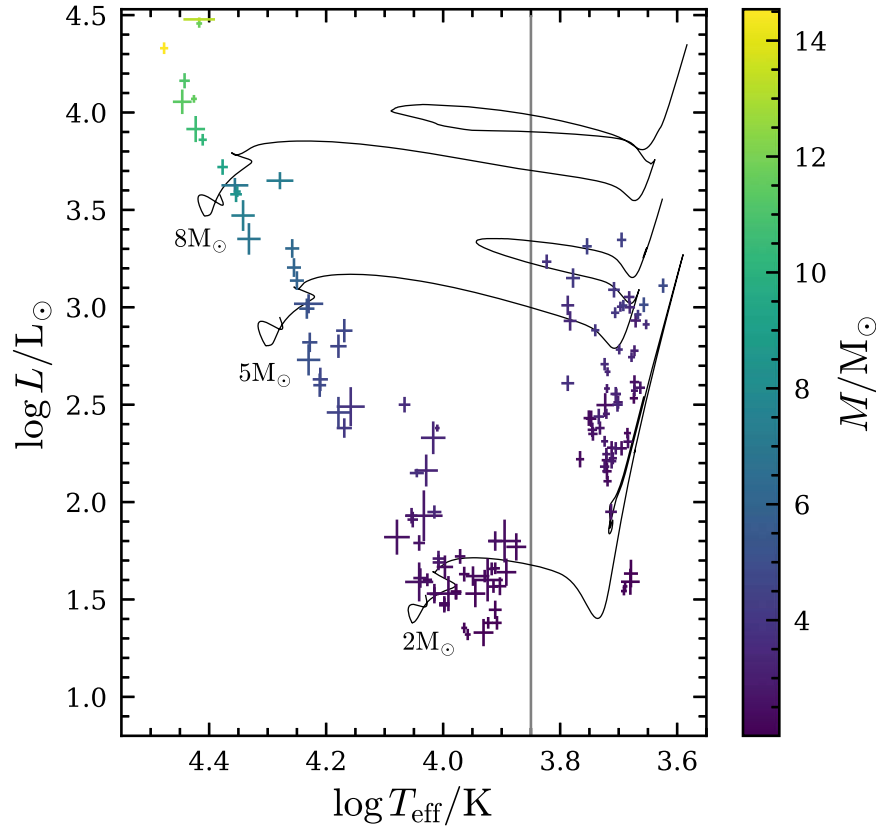


**Figure 10.** Location of the 2–15  $M_{\odot}$  components of the detached eclipsing binaries from DEBCat in the H-R diagram. Overplotted are the reference evolutionary tracks with  $Z = 0.004$  for 2, 5, and 8  $M_{\odot}$ . The vertical line marks  $\log T_{\text{eff}}/K = 3.85$ .

different tracks. We traced the origin of this problem to the development of thin (extent much smaller than  $1H_p$ ) convective shells at the end of core hydrogen burning and their erratic evolution. While these shells persist in a model for a very short time, the erratic changes they cause in chemical profiles may significantly alter subsequent evolution. With the controls available in MESA we could not diminish the problem, and we call for further improvement in convective boundary schemes.

This paper is the first one in a series of papers on the evolutionary and pulsation properties of classical Cepheids. In the follow-up paper, based on the same evolutionary tracks, we will analyze how the studied factors affect the surface and central elemental abundances (O. Ziółkowska et al. 2024, in preparation). The reference model we have defined and justified here will serve as a reference for further evolutionary calculations in which effects of overshooting, mass loss, and rotation will be explored in detail (R. Smolec et al. 2024, in preparation). The derived uncertainties of the evolutionary tracks will allow us to determine the uncertainties of relationships relevant to the study of Cepheids, such as the mass–luminosity relation.

### Acknowledgments

This research is supported by the National Science Center, Poland, Sonata BIS project 2018/30/E/ST9/00598. This research was supported in part by grant NSF PHY-1748958 to the Kavli Institute for Theoretical Physics (KITP). A.T. is a Research Associate at the Belgian Scientific Research Fund (F.R.S.-F.N.R.S.).

**Table 7**

Median Uncertainties (in Percent) of Luminosity, Effective Temperature, and Mass of Stars from DEBCat for Low-temperature (Helium-burning Stars), High-temperature (Main Sequence), and All Stars

	$\log T_{\text{eff}}/K < 3.85$	$\log T_{\text{eff}}/K > 3.85$	All
$\delta \log L/L_{\odot}$	1.3	2.2	1.6
$\delta \log T_{\text{eff}}/K$	0.2	0.3	0.2
$\delta M/M_{\odot}$	0.8	1.1	1.0

*Software:* PyMesaReader (Wolf & Schwab 2017), Mkip (Marchant 2019, 2020), MESA 21.12.1 (Paxton 2021), MESA SDK 22.6.1 (Townsend 2022), Numpy (Harris et al. 2020), Matplotlib (Hunter 2007), Pandas (The pandas development team 2022; McKinney 2010).

### Appendix A Inlist for an Exemplary Reference Model

In Appendix A we present the inlist for the reference model described in Section 2.2.

```
\begin{minted}{fortran}
&star_job
    history_columns_file='history_columns_cep.list'
    profile_columns_file='profile_columns_cep.list'

    save_model_when_terminate=.true.
    save_model_filename='final.mod'

! abundances
    initial_zfracs = 6 ! A09
```

```

! nuclear net
  change_net = .true.
  new_net_name = 'pp_and_cno_extras.net'

  set_rate_cl2ag = 'Kunz'
  set_rate_n14pg = 'jina reaclib'
  show_net_species_info = .false.
  show_net_reactions_info = .false.

! chemical composition for ZAMS model
  relax_y = .true.
  new_y = yyyy
  relax_z = .true.
  new_z = zzzz
/

&kap
  kap_file_prefix = 'a09'
  kap_lowT_prefix = 'lowT_fa05_a09p'
  kap_CO_prefix = 'a09_co'

  use_Zbase_for_Type1 = .true.
  use_Type2_opacities = .true.
  Zbase = zzzz

  cubic_interpolation_in_X = .true.
  cubic_interpolation_in_Z = .true.
/

&controls
  initial_mass = mmmm

  MLT_option = 'Henyey'
  mixing_length_alpha = 1.77

! convective boundaries
  use_Ledoux_criterion = .false.

  recalc_mix_info_after_evolve = .true.

  predictive_mix(1) = .true.
  predictive_zone_type(1) = 'any'
  predictive_zone_loc(1) = 'core'
  predictive_bdy_loc(1) = 'any'

  predictive_superad_thresh(1) = 0.005d0
  predictive_avoid_reversal(1) = 'he4'

! semiconvection
  alpha_semiconvection = 0

! atmosphere
  atm_option = 'table'
  atm_table = 'photosphere'
  atm_off_table_option = 'T_tau'

! diffusion
  do_element_diffusion = .false.

! convergence parameters
  mesh_delta_coeff = 0.5d0
  time_delta_coeff = 0.5d0
  max_years_for_timestep = 1d6

  varcontrol_target = 1d-4
  max_allowed_nz = 32000

  ! limit on magnitude of relative change at surface
  delta_HR_limit = 0.005d0
  delta_lgTeff_limit = 0.005d0
  delta_lgL_limit = 0.01

  ! limit on magnitude of relative change at center
  delta_lgT_cntr_limit = 0.005d0
  delta_lgRho_cntr_limit = 0.025d0

  ! when to stop
  max_age = 15d9

  ! output
  star_history_name = 'history.data'
  history_interval = 1
  terminal_interval = 1000
  write_header_frequency = 1000
  profile_interval = 50
  max_num_profile_models = 1000
  photo_interval = -1 !

  warn_when_large_rel_run_E_err = 99d0
  calculate_Brunt_N2 = .true.
/
\end{minted}

```

## Appendix B Tracks

In Appendix B we provide H-R diagrams, starting with the lower-mass models (Figures 11–26), first without and then with overshooting, followed by the higher-mass models without and with overshooting (Figures 27 and 28).

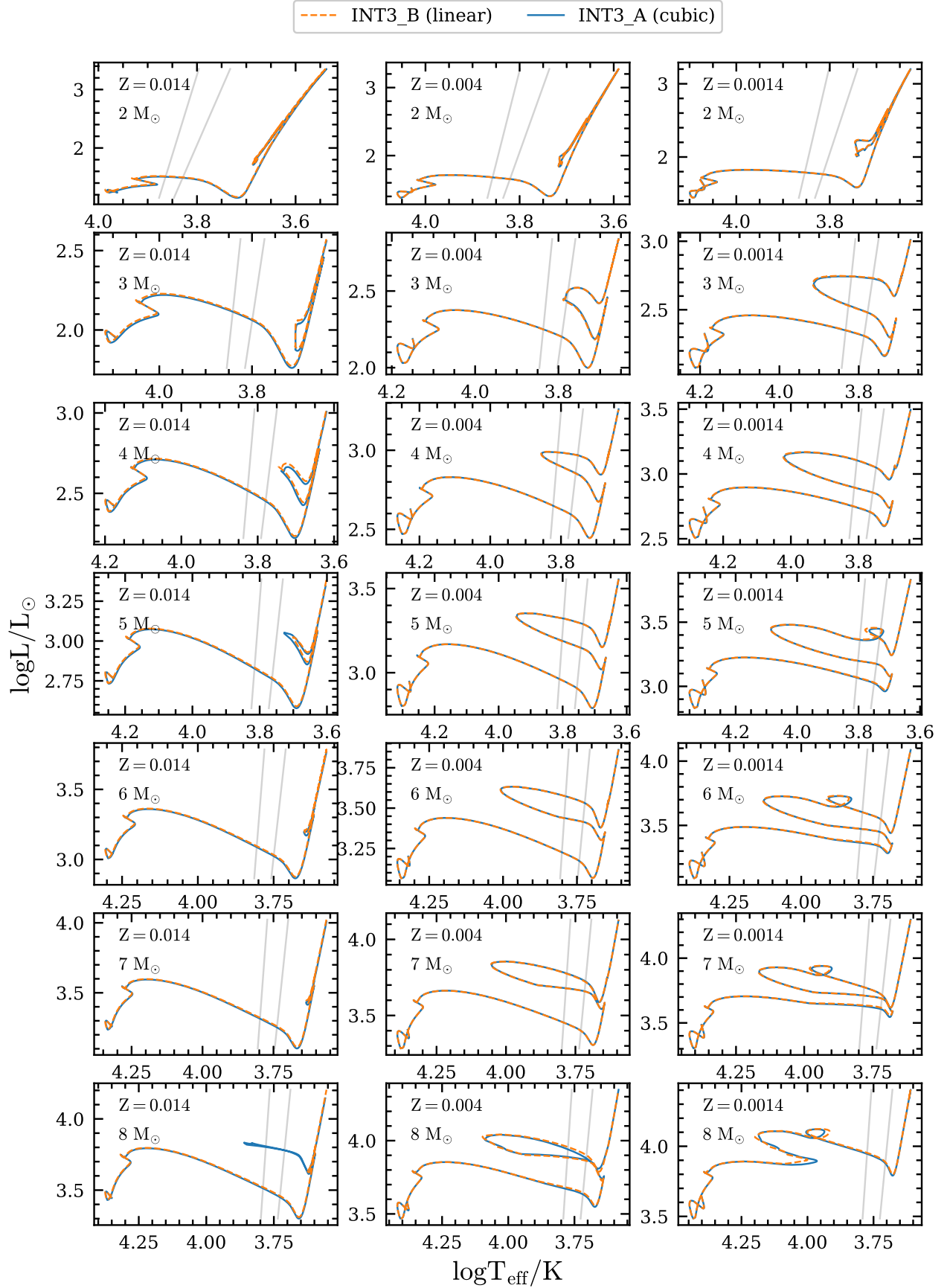


**Figure 11.** Tracks for 2–8  $M_{\odot}$  (rows) and  $Z = 0.014$ , 0.004, and 0.0014 (columns) and different methods for interpolating opacity tables (line style and color).

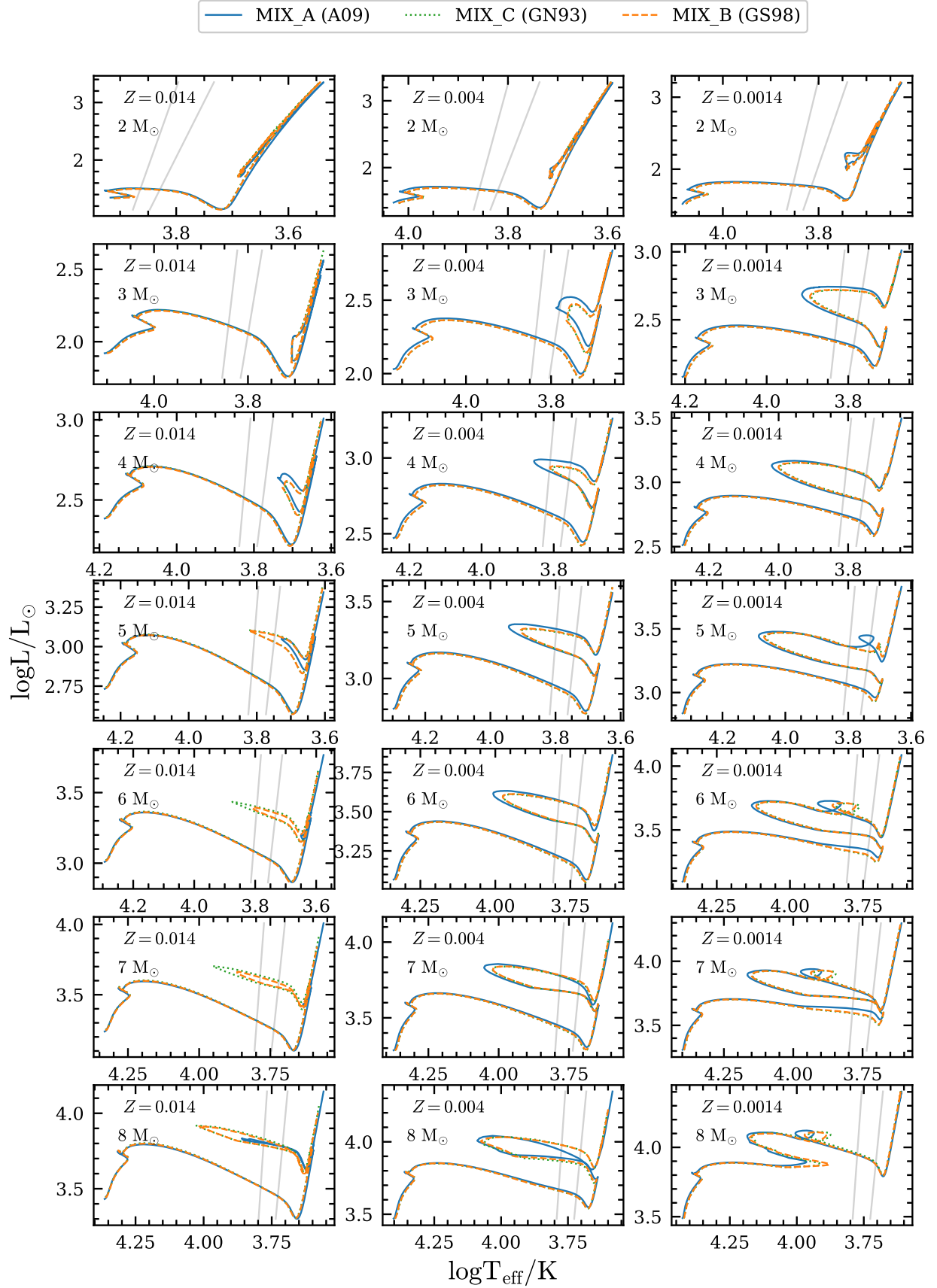


**Figure 12.** Tracks for  $2$ – $8 M_{\odot}$  (rows) and  $Z = 0.014$ ,  $0.004$ , and  $0.0014$  (columns) and different solar mixtures of heavy elements (line style and color).



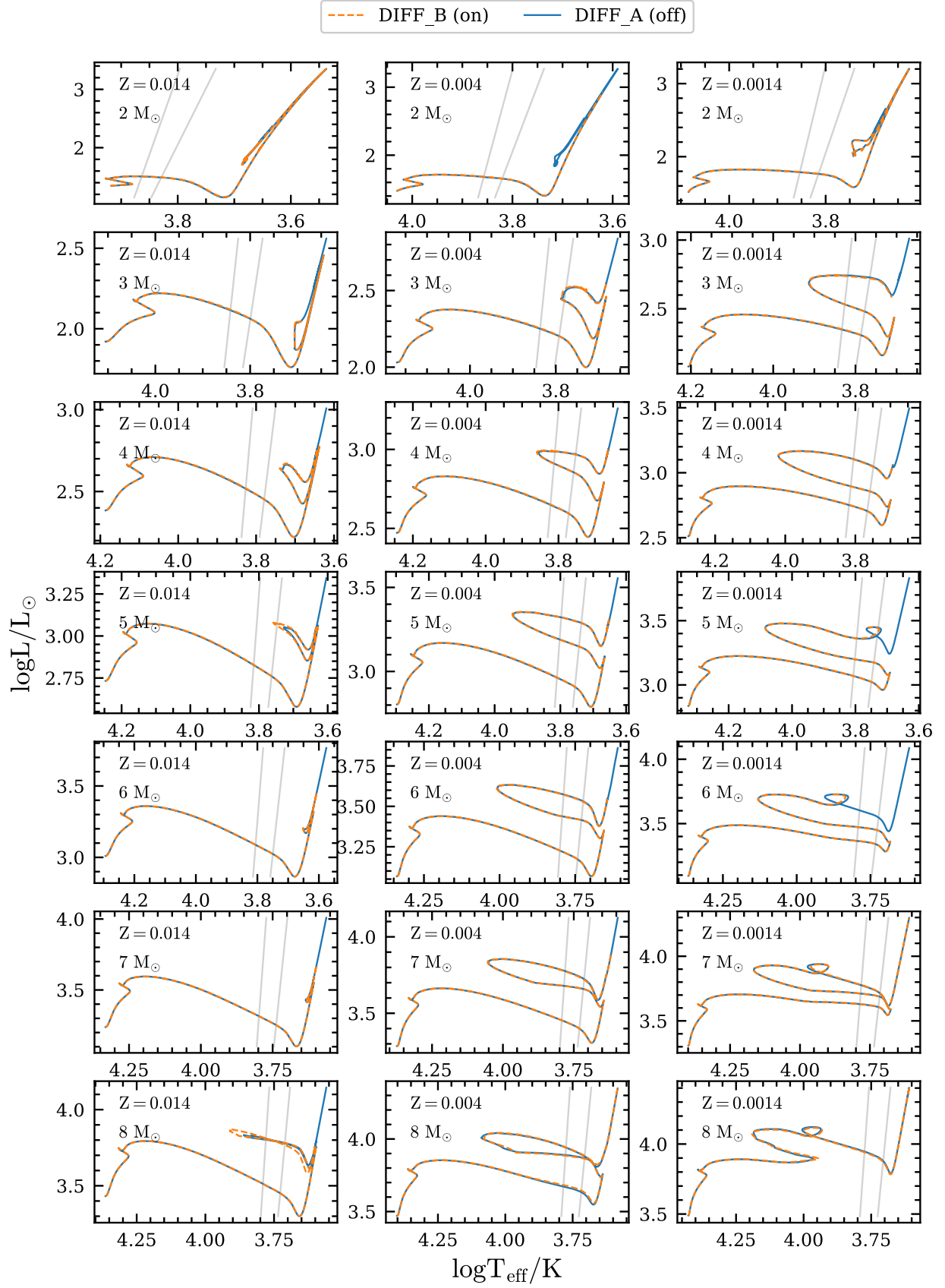


**Figure 13.** Tracks for  $2\text{--}8 M_{\odot}$  (rows) and  $Z = 0.014, 0.004$ , and  $0.0014$  (columns) and atomic diffusion included or not (line style and color).

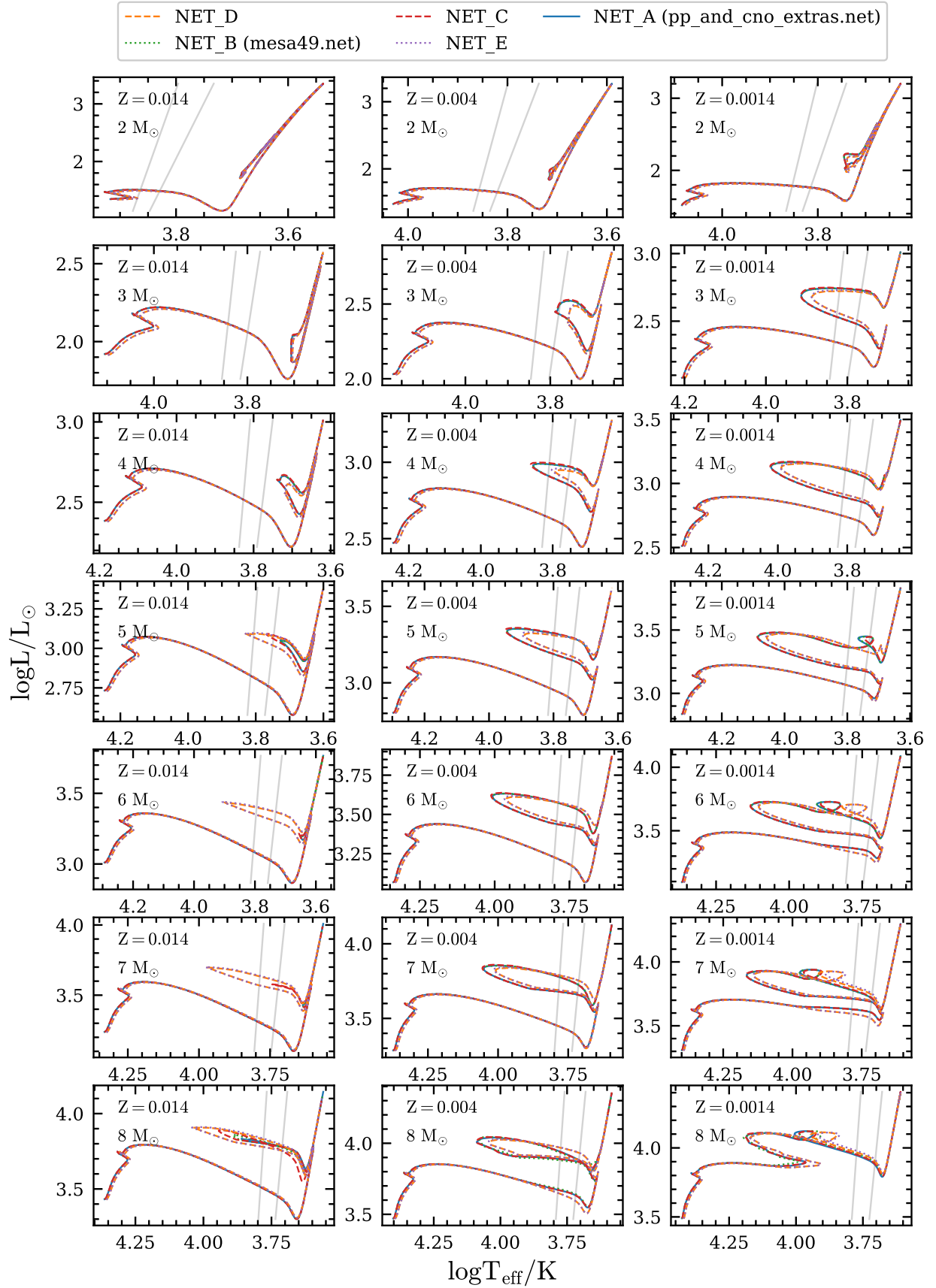


**Figure 14.** Tracks for 2–8  $M_{\odot}$  (rows) and  $Z = 0.014$ , 0.004, and 0.0014 (columns) and different nuclear reaction rates and nuclear net settings (line style and color).

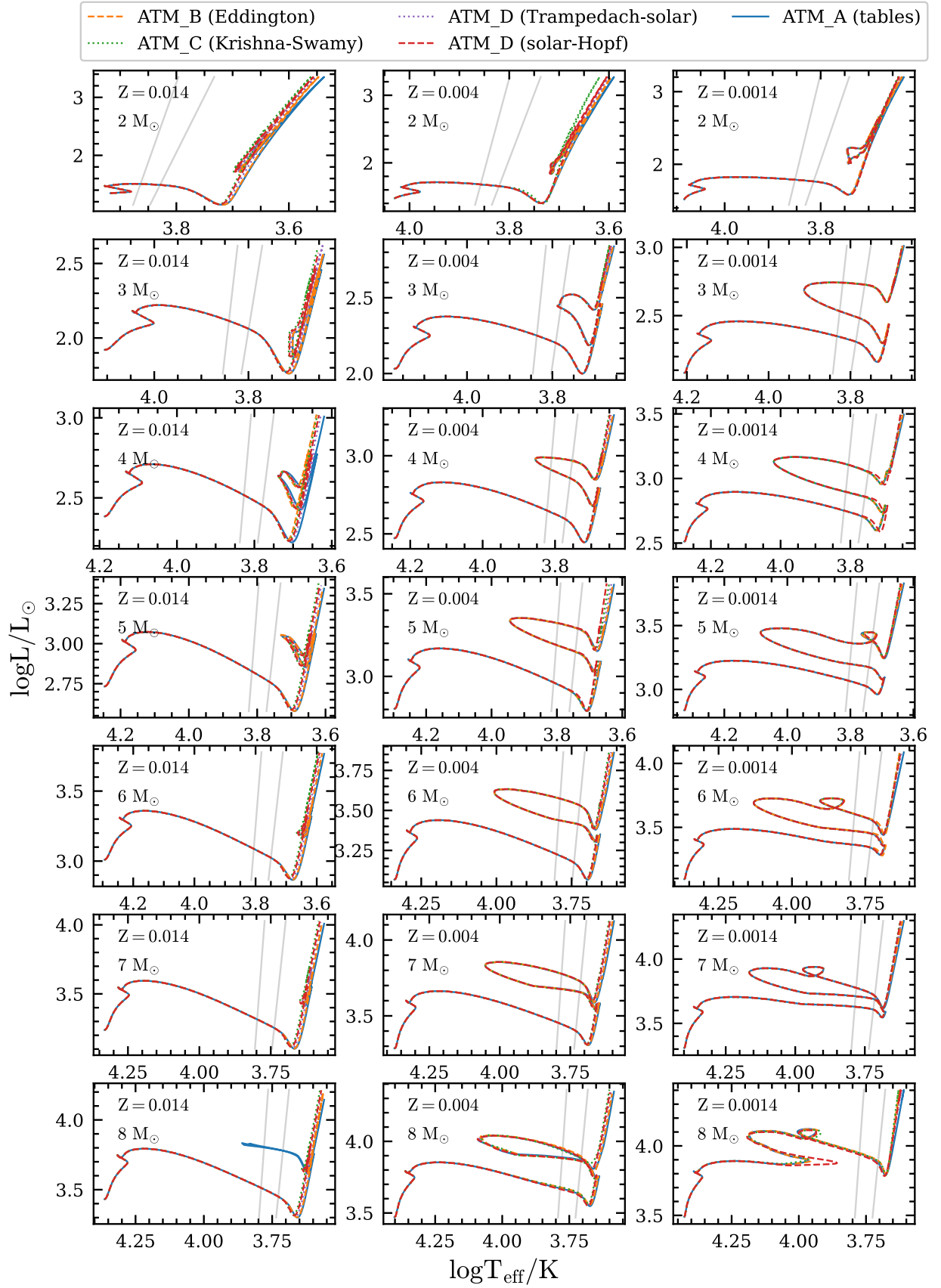


**Figure 15.** Tracks for 2–8  $M_{\odot}$  (rows) and  $Z = 0.014$ , 0.004, and 0.0014 (columns) and different atmosphere settings (line style and color).



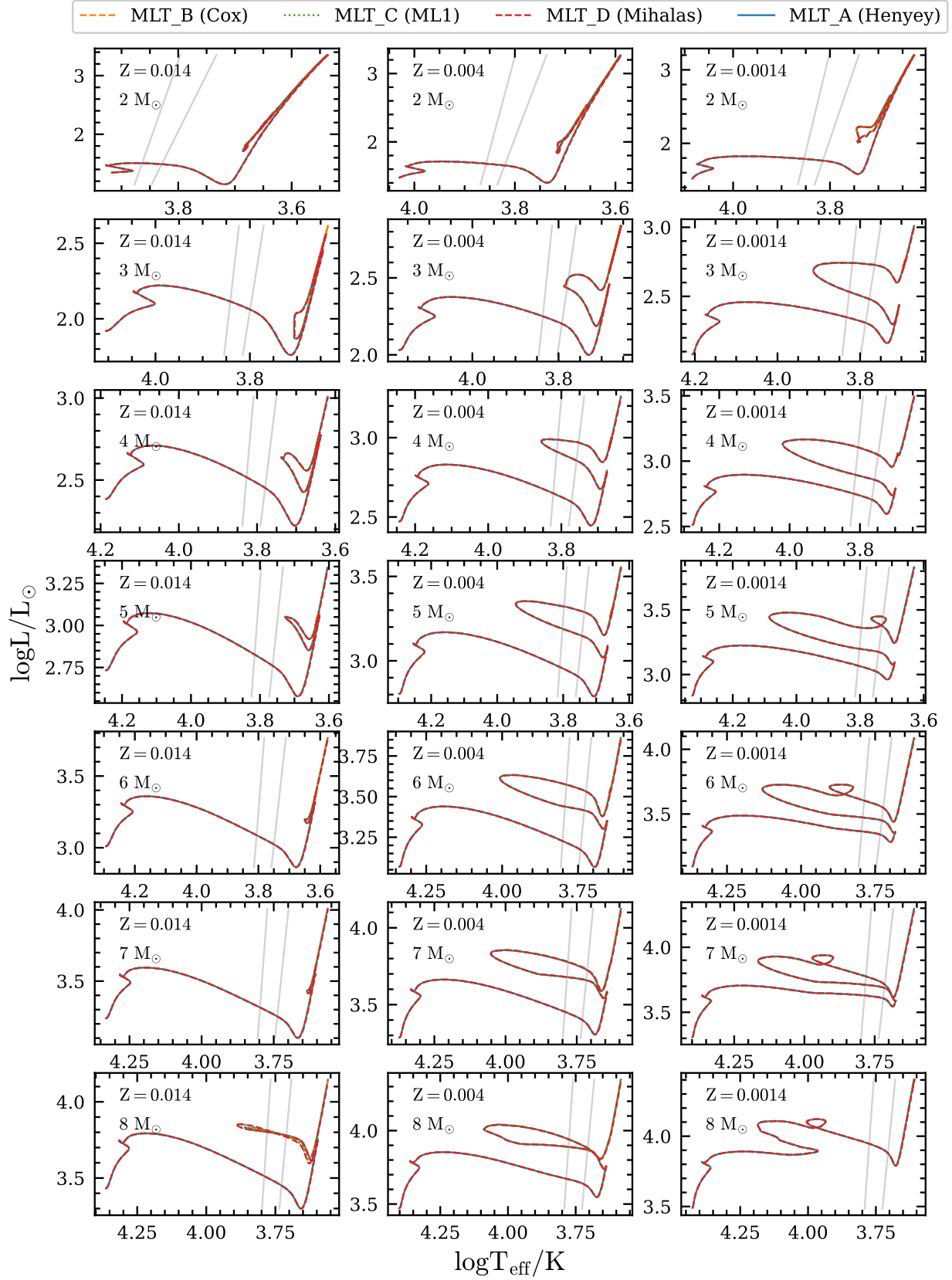


**Figure 16.** Tracks for  $2\text{--}8 M_{\odot}$  (rows) and  $Z = 0.014$ ,  $0.004$ , and  $0.0014$  (columns) and different MLT settings (line style and color).

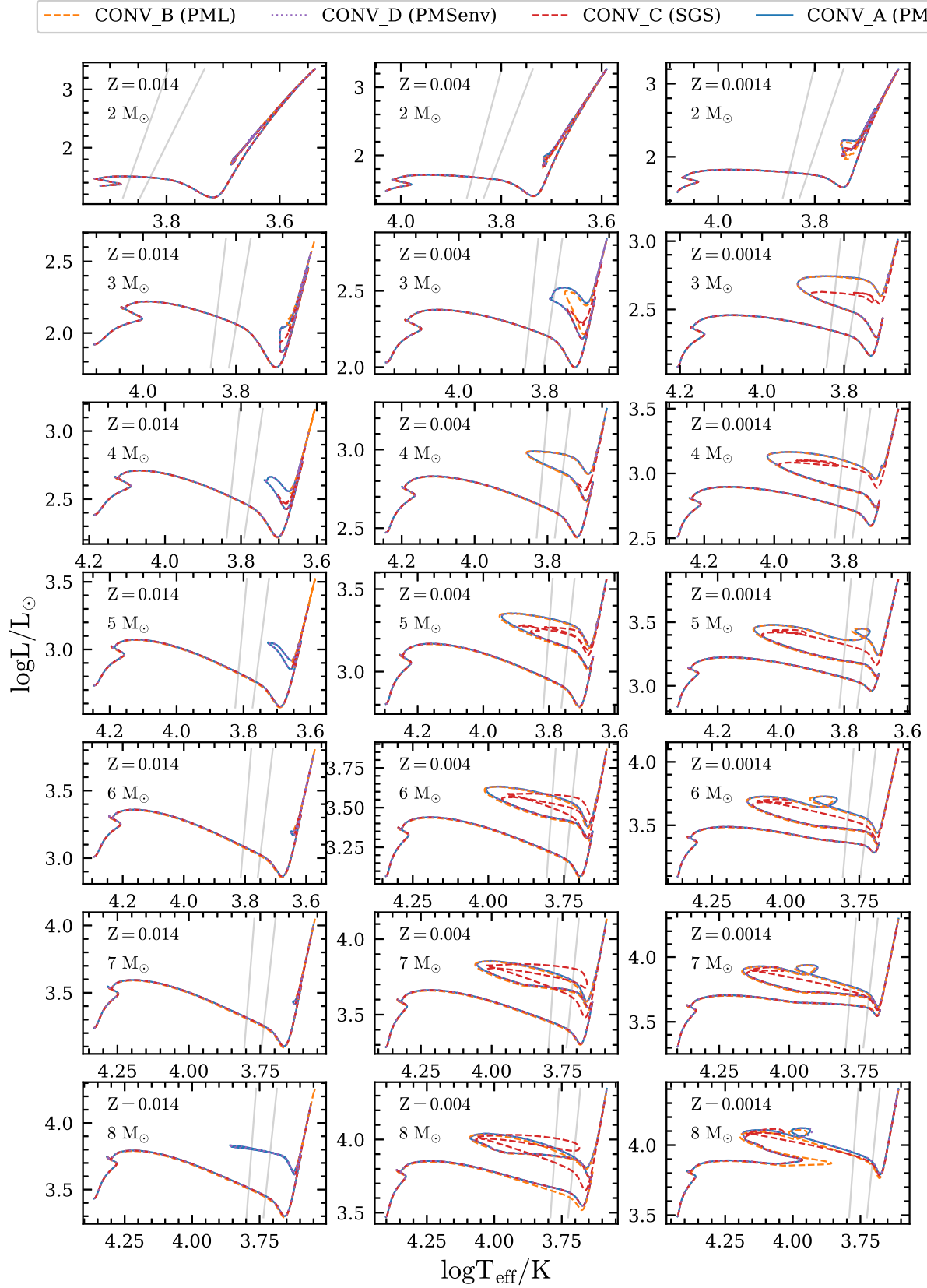


**Figure 17.** Tracks for  $2\text{--}8 M_{\odot}$  (rows) and  $Z = 0.014$ ,  $0.004$ , and  $0.0014$  (columns) and different schemes for calculating boundaries of convective regions (line style and color).

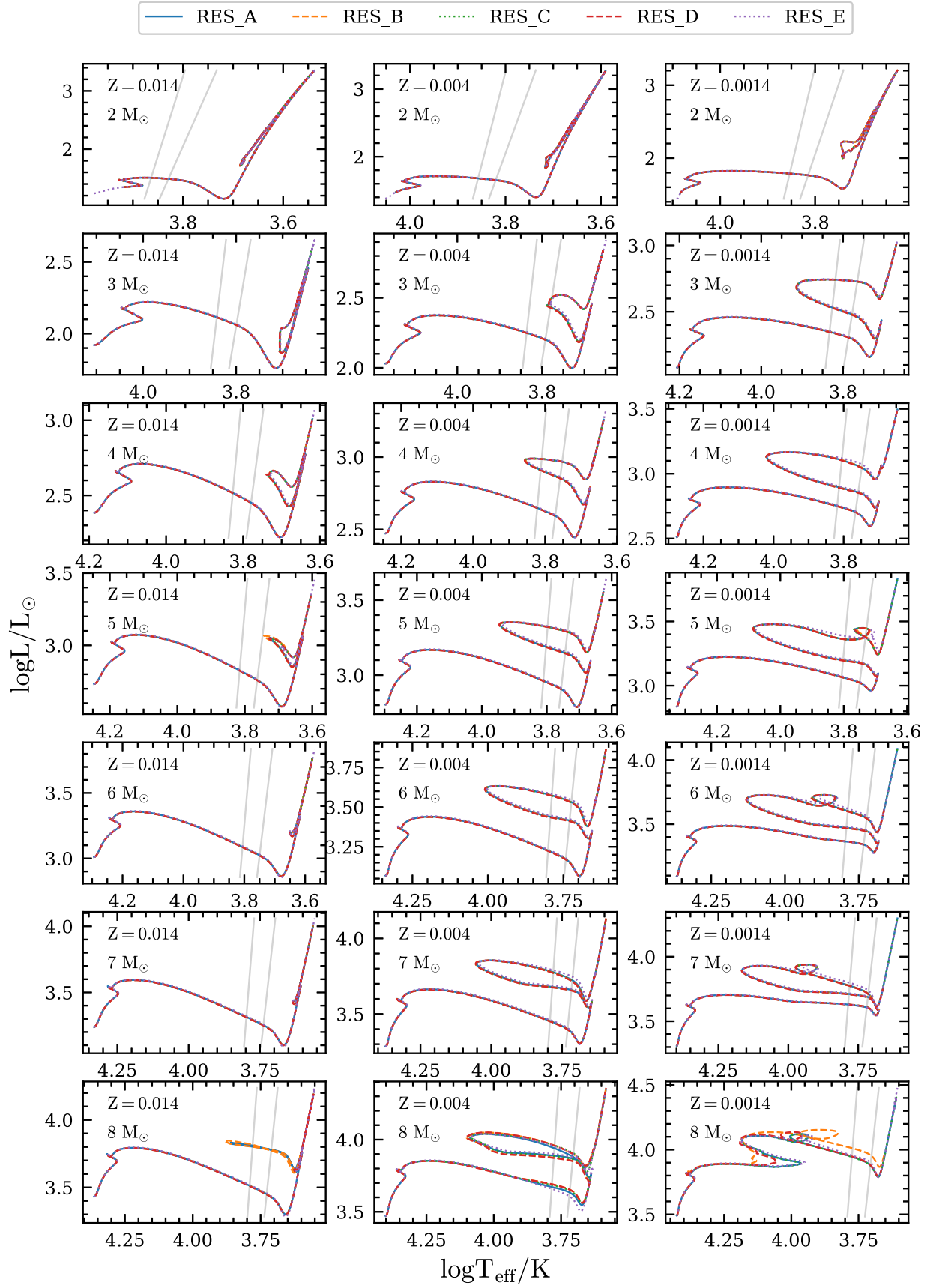


**Figure 18.** Tracks for 2–8  $M_{\odot}$  (rows) and  $Z = 0.014$ , 0.004, and 0.0014 (columns) and different resolution settings (line style and color) as in Table 2.



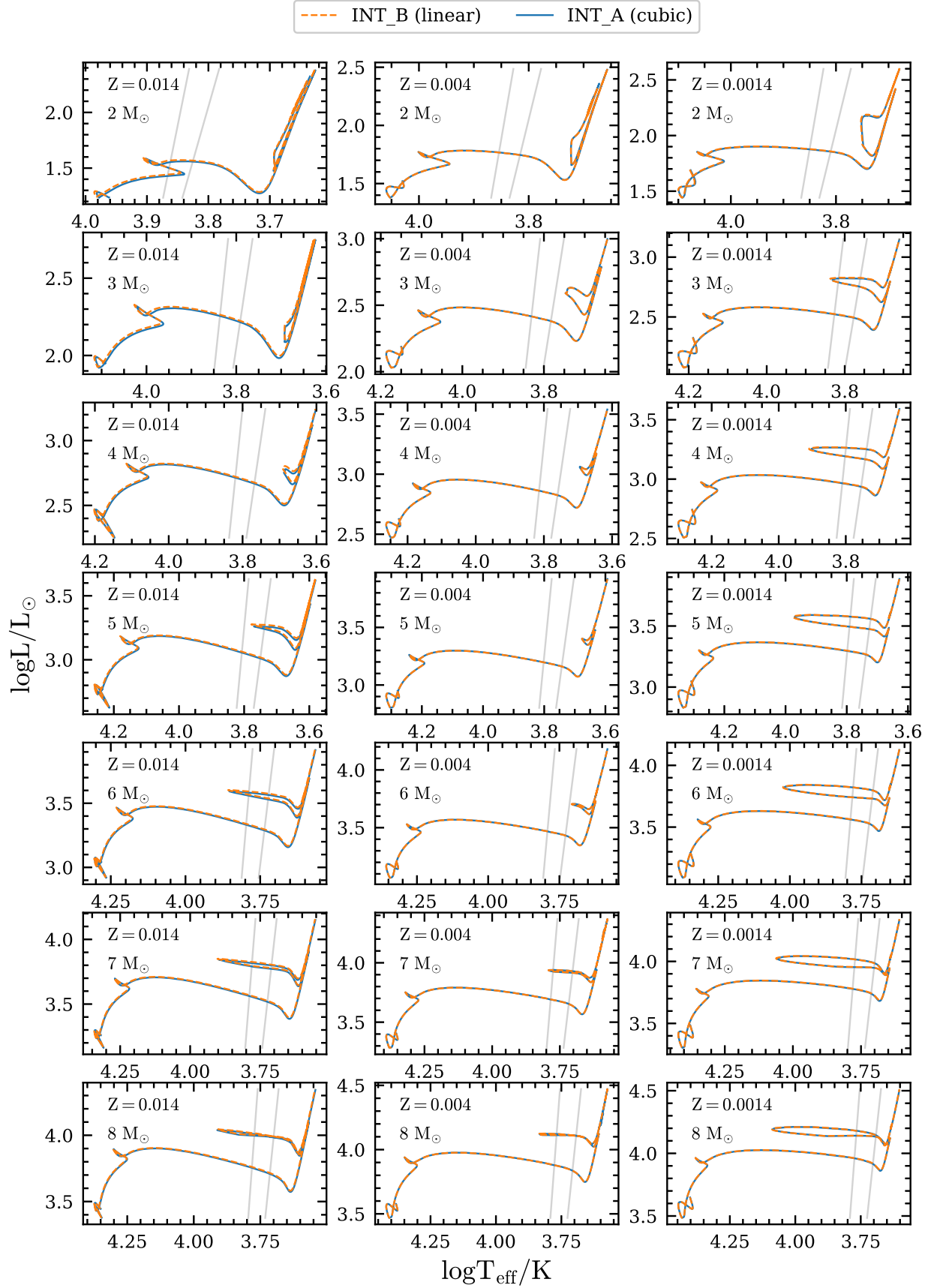


**Figure 19.** Tracks for  $2\text{--}8 M_{\odot}$  (rows) and  $Z = 0.014, 0.004$ , and  $0.0014$  (columns) and different methods for interpolating opacity tables (line style and color) with convective core overshooting.

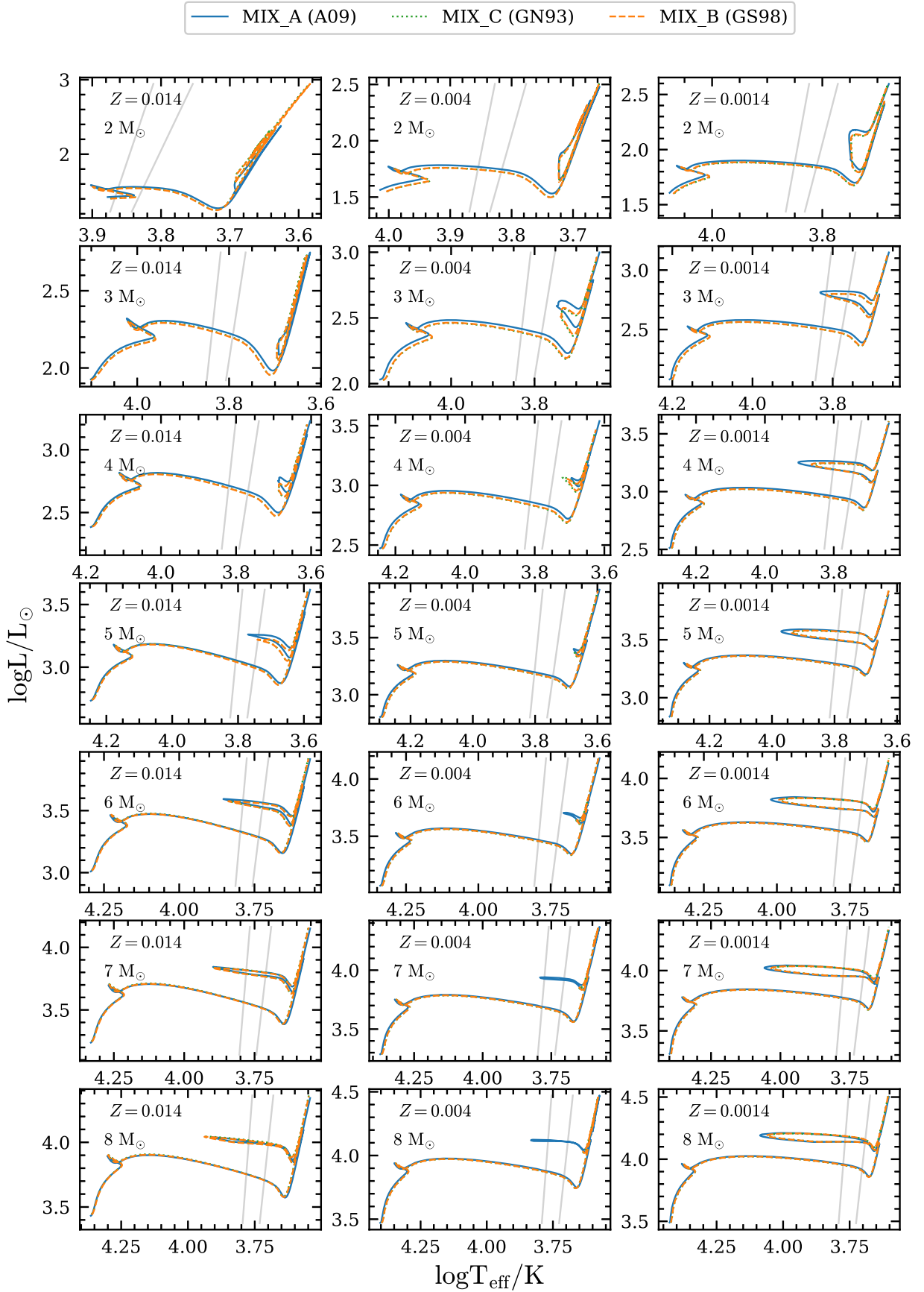


**Figure 20.** Tracks for 2–8  $M_{\odot}$  (rows) and  $Z = 0.014$ , 0.004, and 0.0014 (columns) and different solar mixtures of heavy elements (line style and color) with convective core overshooting.

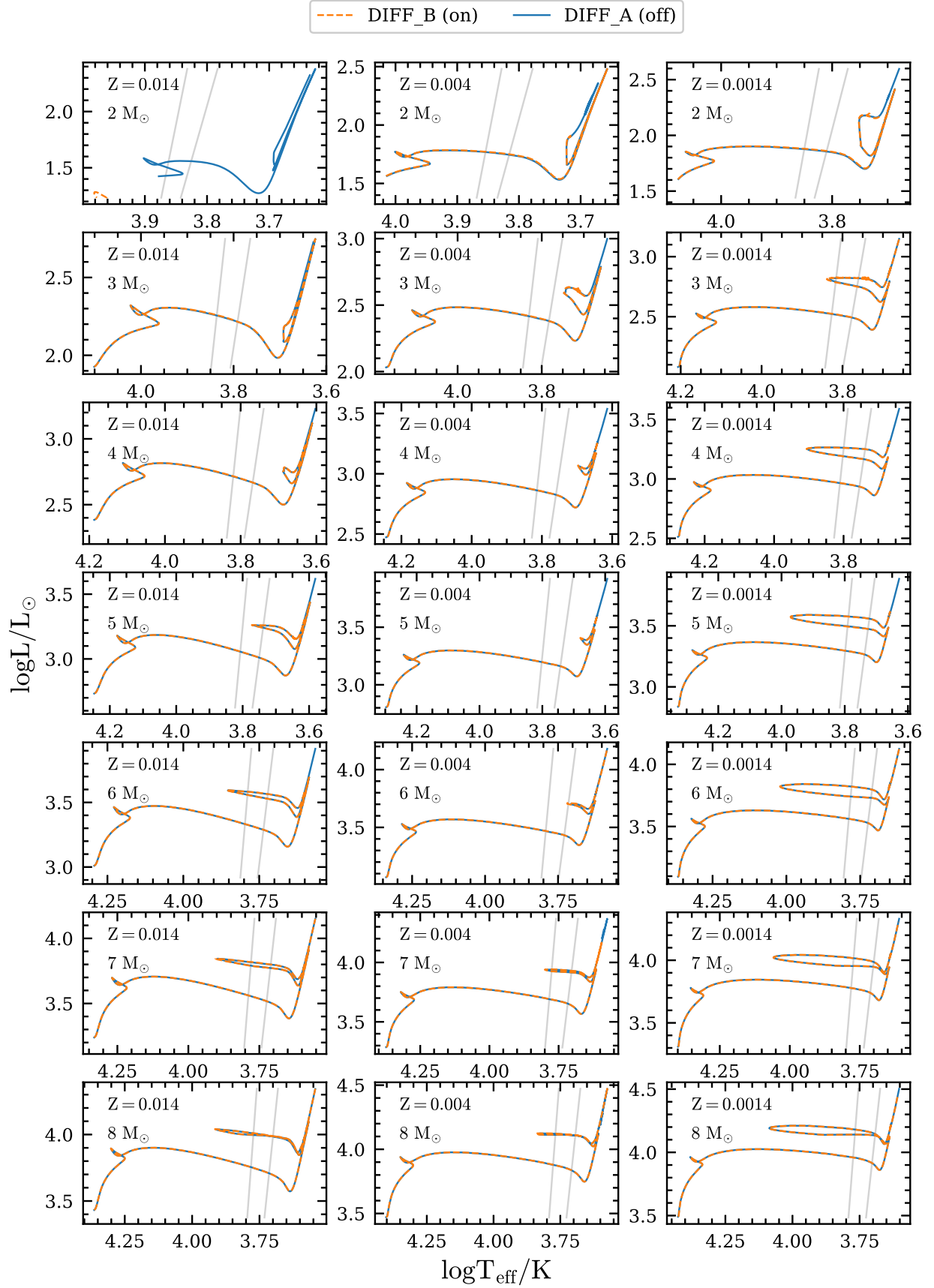


**Figure 21.** Tracks for 2–8  $M_{\odot}$  (rows) and  $Z = 0.014$ , 0.004, and 0.0014 (columns) and atomic diffusion included or not (line style and color) with convective core overshooting.



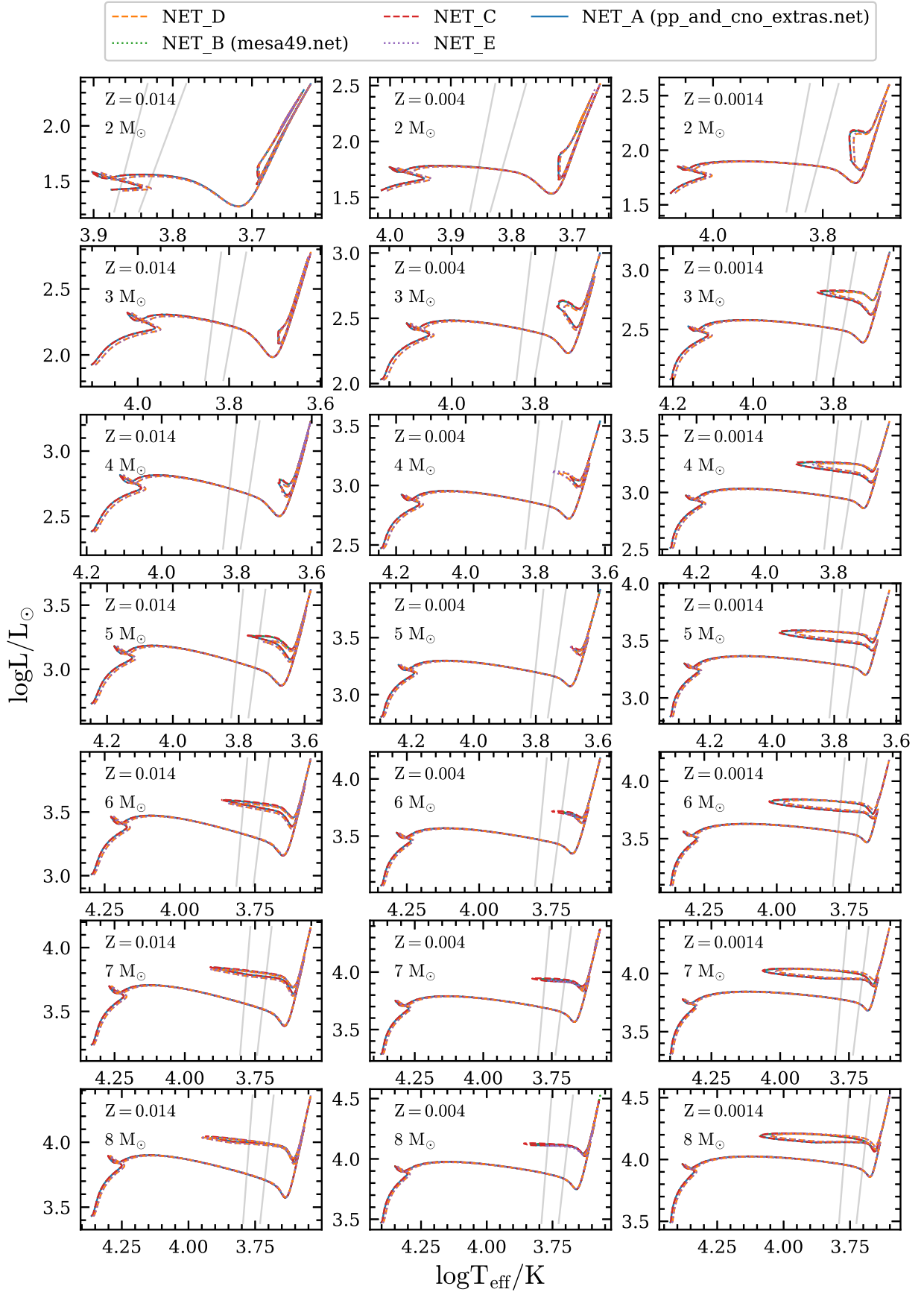


**Figure 22.** Tracks for 2–8  $M_{\odot}$  (rows) and  $Z = 0.014$ ,  $0.004$ , and  $0.0014$  (columns) and different nuclear reaction rates and nuclear net settings (line style and color) with convective core overshooting.

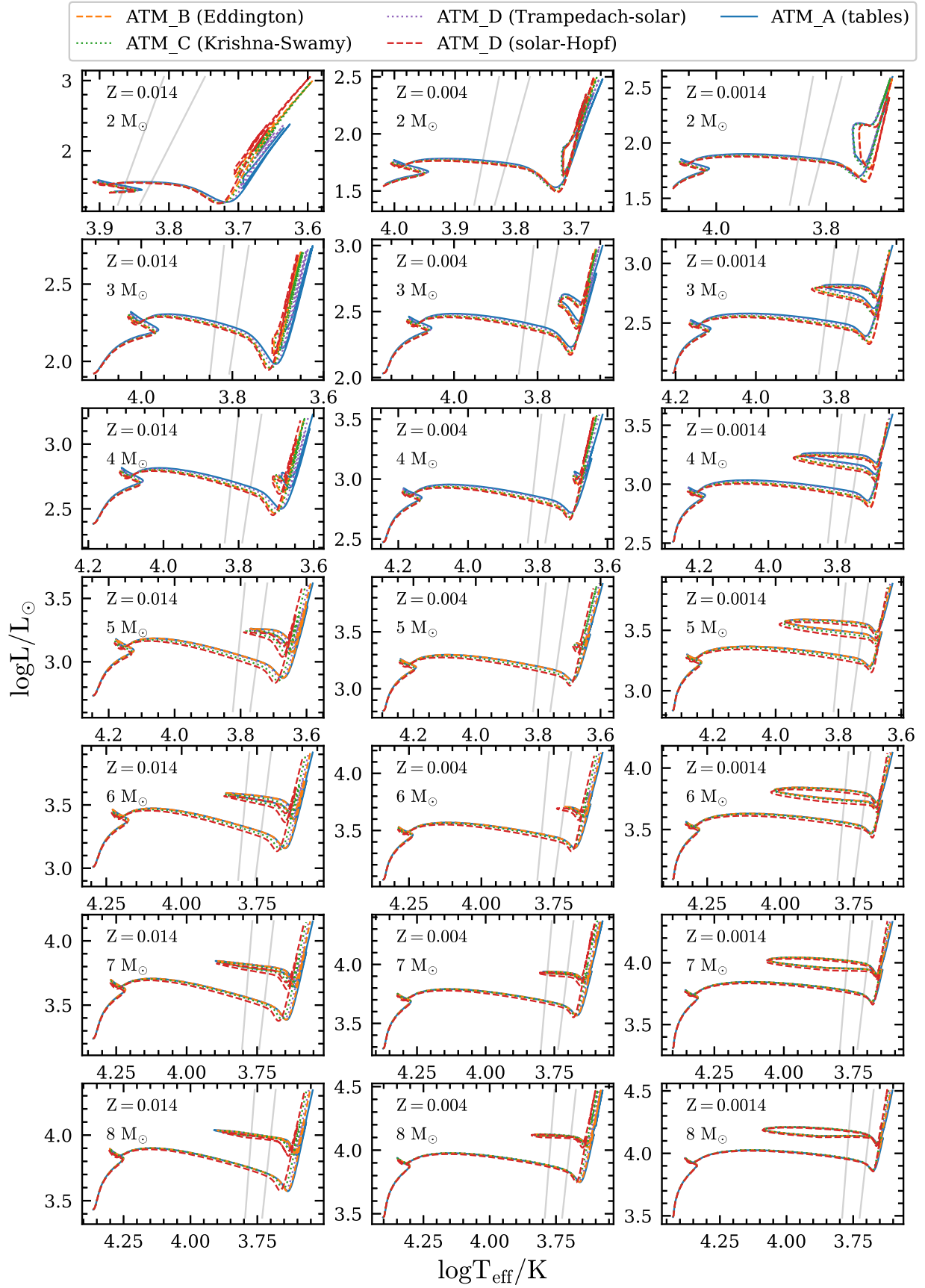


**Figure 23.** Tracks for 2–8  $M_{\odot}$  (rows) and  $Z = 0.014$ , 0.004, and 0.0014 (columns) and different atmosphere settings (line style and color) with convective core overshooting.

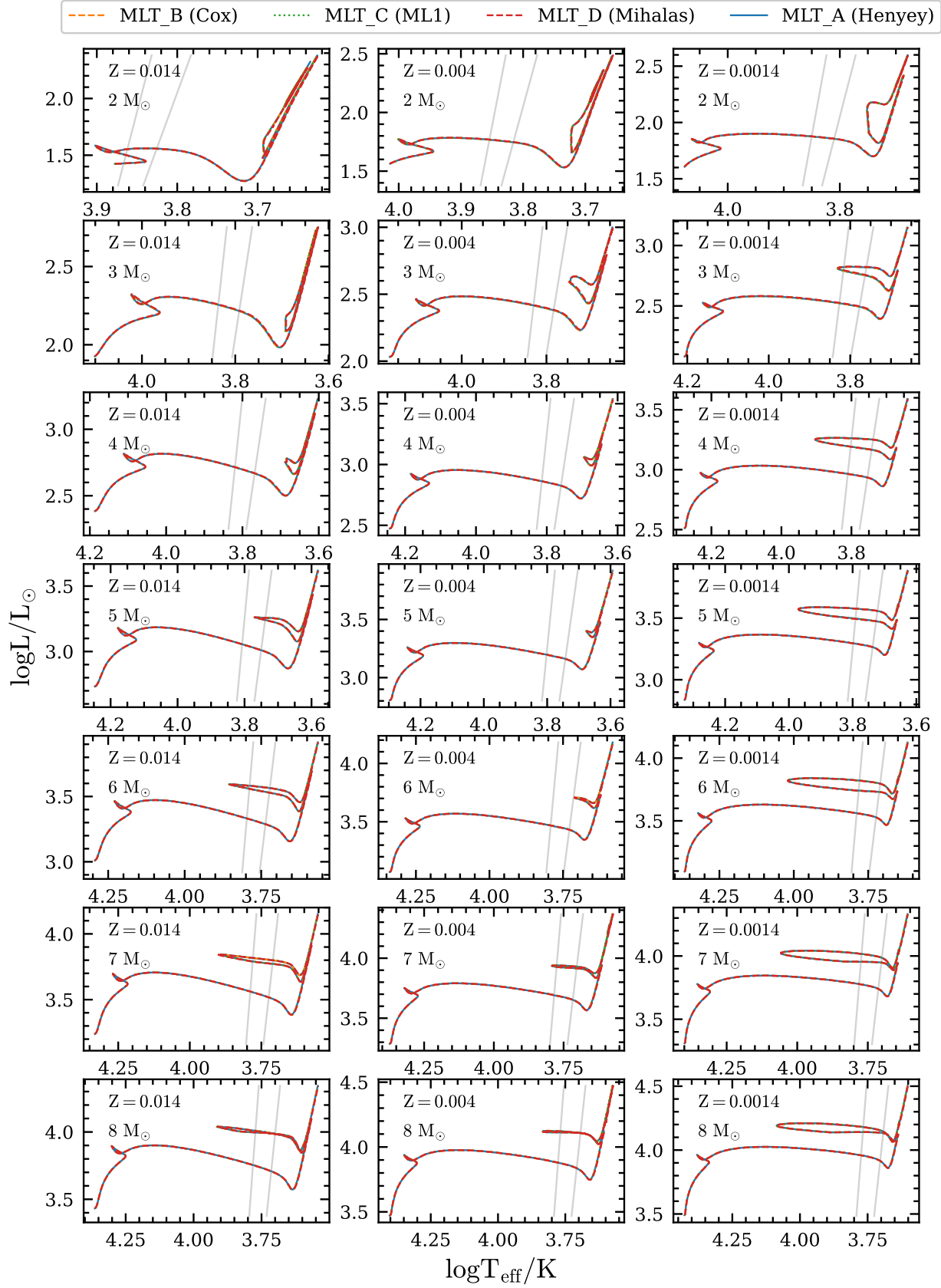


**Figure 24.** Tracks for  $2\text{--}8 M_{\odot}$  (rows) and  $Z = 0.014$ ,  $0.004$ , and  $0.0014$  (columns) and different MLT settings (line style and color) with convective core overshooting.

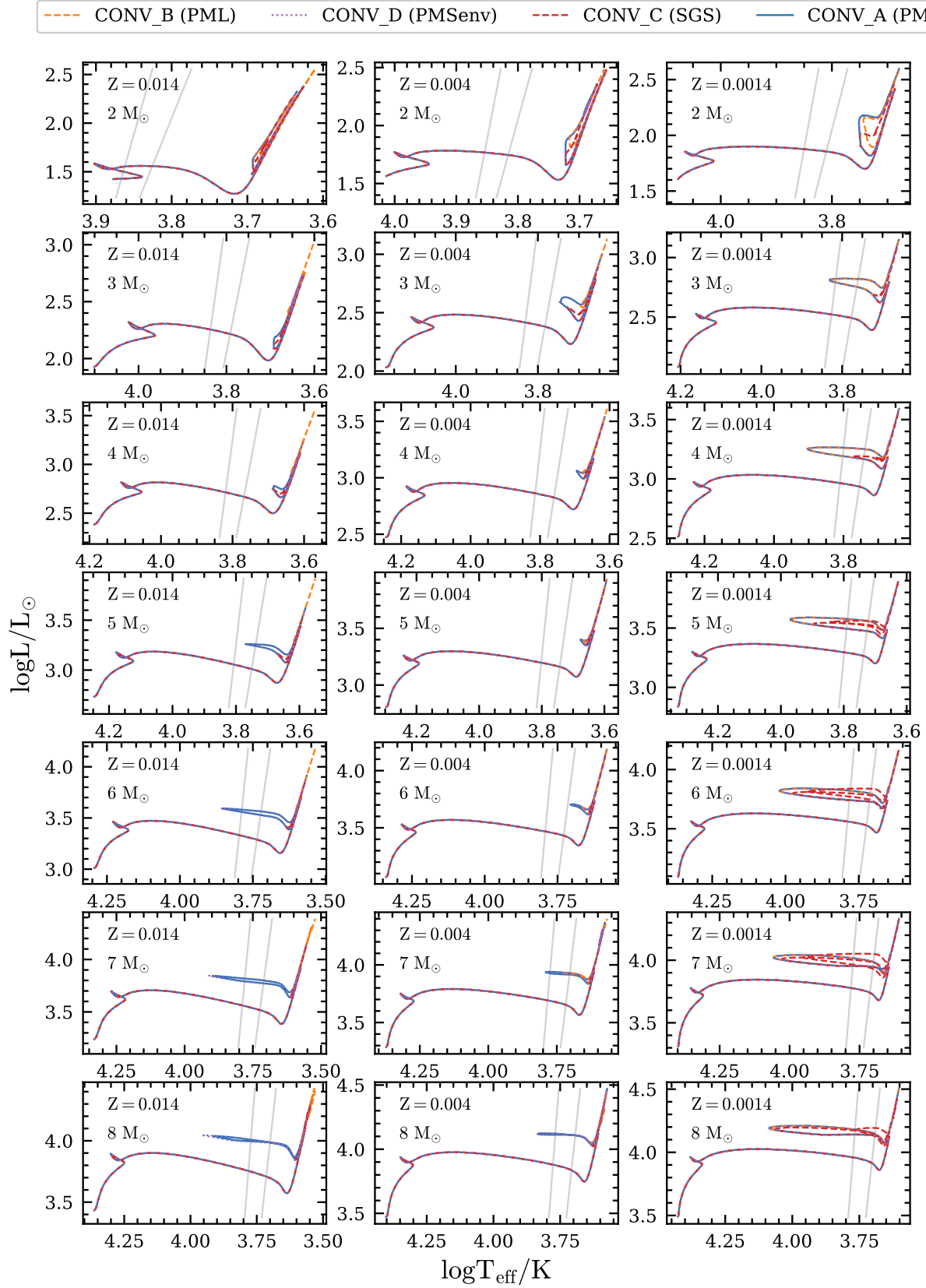


**Figure 25.** Tracks for  $2\text{--}8 M_{\odot}$  (rows) and  $Z = 0.014, 0.004$ , and  $0.0014$  (columns) and different schemes for calculating boundaries of convective regions (line style and color) with convective core overshooting.



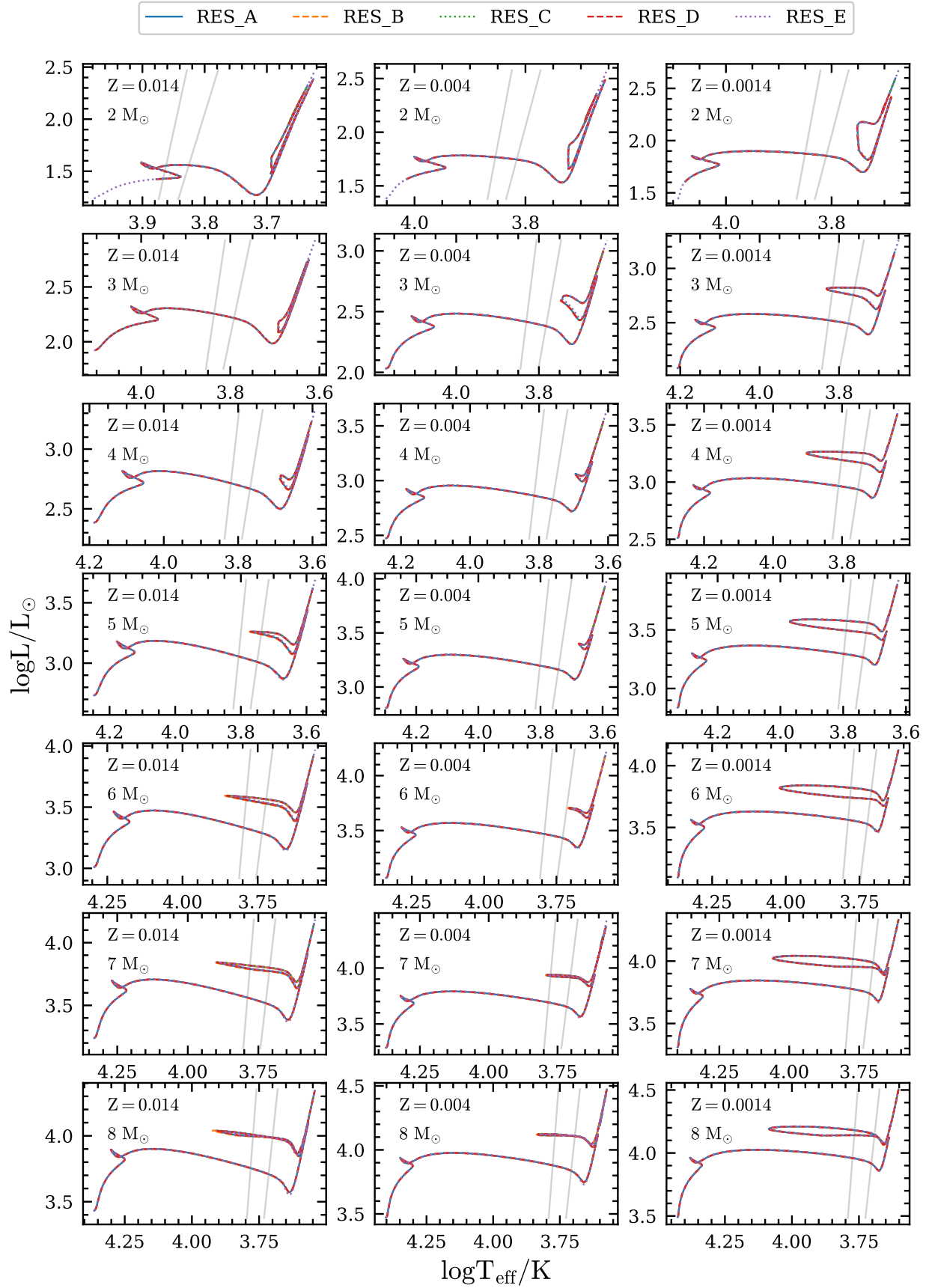


**Figure 26.** Tracks for  $2\text{--}8 M_{\odot}$  (rows) and  $Z = 0.014, 0.004$ , and  $0.0014$  (columns) and different resolution settings (line style and color) as in Table 2 with convective core overshooting.

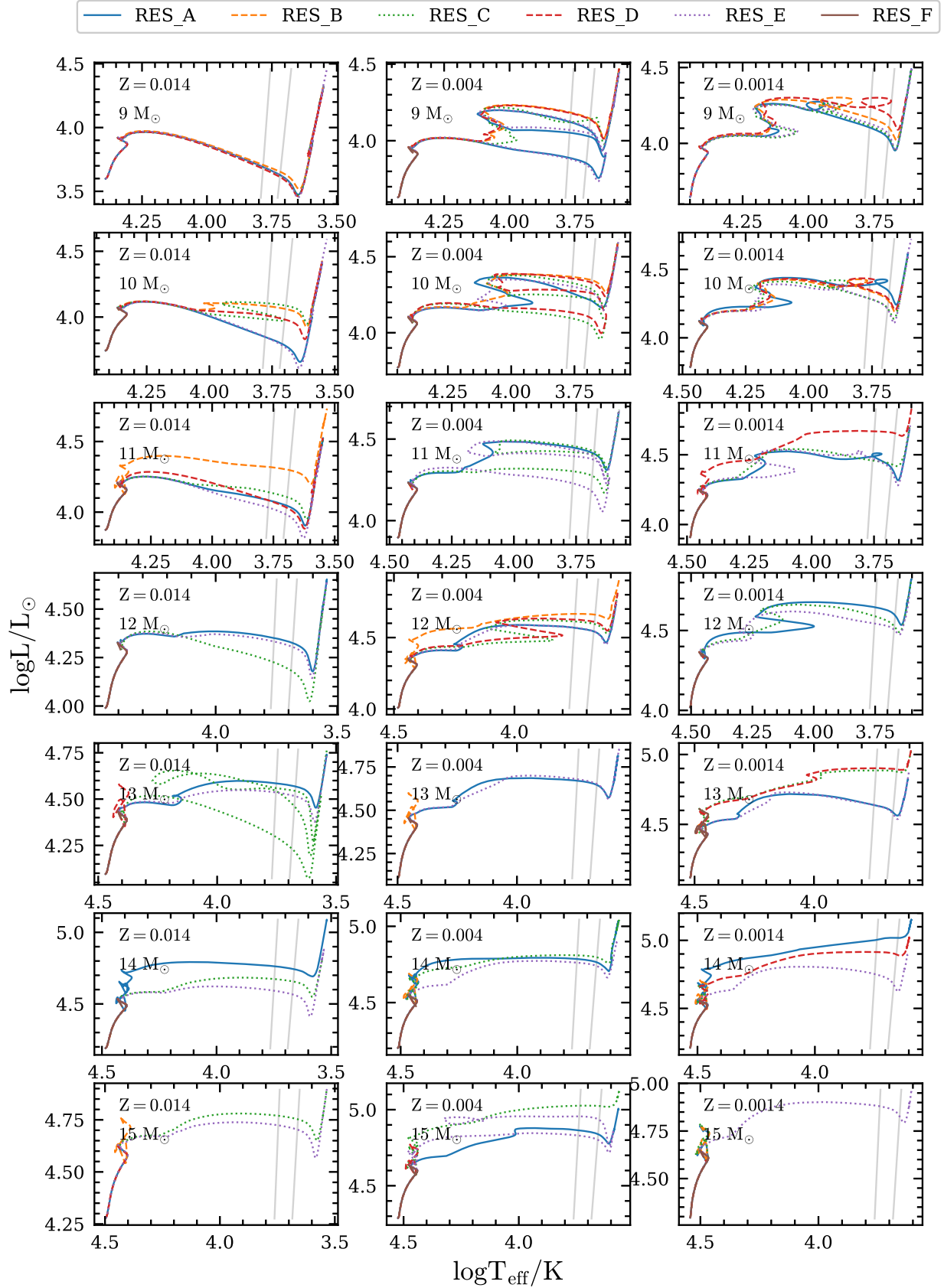


**Figure 27.** Tracks for 9–15  $M_{\odot}$  (rows) and  $Z = 0.014$ ,  $0.004$ , and  $0.0014$  (columns) and different resolution settings (line style and color) as in Table 2.

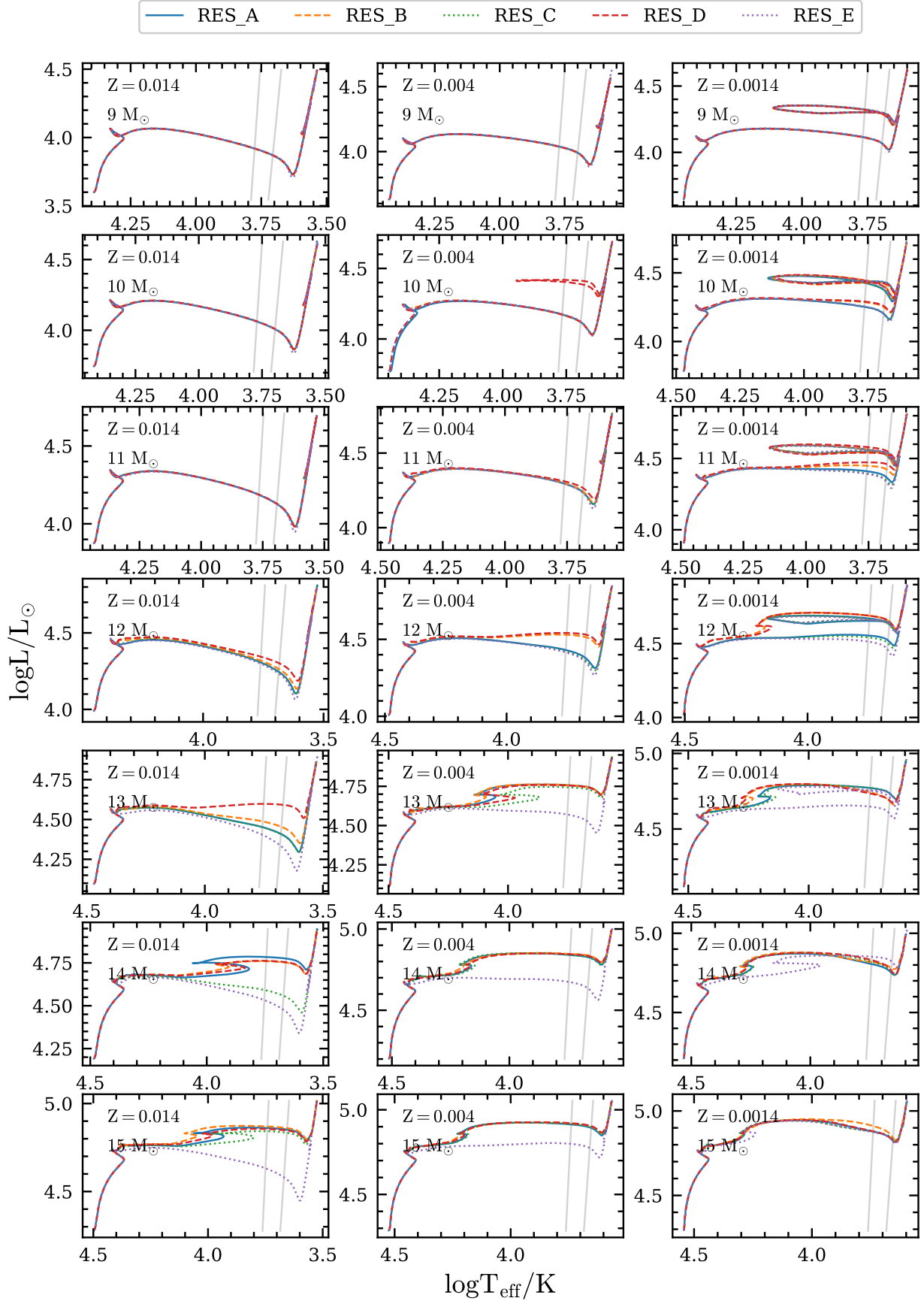


**Figure 28.** Tracks for 9–15  $M_{\odot}$  (rows) and  $Z = 0.014$ , 0.004, and 0.0014 (columns) and different resolution settings (line style and color) as in Table 2 with convective core overshooting.

## Appendix C

### Tables

In Appendix C we provide Tables 8–17 containing the reference, maximal, and minimal values of logarithms of age,

effective temperature, and luminosity together with the set corresponding to the extreme value. We present the tables for models first without and then later with overshooting. Each table corresponds to a given evolutionary stage.

**Table 8**  
Comparison of Physical Quantities (Nuclear Ages, Effective Temperatures, Luminosities; All in Logarithms) of Models 2–8  $M_{\odot}$  at TAMS

Mass	Z	log age <sup>ref</sup>	log age <sup>max</sup>	log age <sup>min</sup>	log $T_{\text{eff}}^{\text{ref}}$	log $T_{\text{eff}}^{\text{max}}$	log $T_{\text{eff}}^{\text{min}}$	log $L^{\text{ref}}$	log $L^{\text{max}}$	log $L^{\text{min}}$
2.0	0.0014	8.76151	8.77015	8.75952	4.06721	4.0685	4.05764	1.73978	1.74381	1.73351
			NET_E	CONV_B		INT_B	NET_E		RES_E	MIX_C
2.0	0.004	8.82421	8.83195	8.82112	4.00795	4.00878	3.99665	1.66051	1.66508	1.64696
			NET_E	CONV_B		CONV_B	MIX_C		RES_E	MIX_C
2.0	0.014	8.95149	8.96172	8.93954	3.91538	3.92016	3.90461	1.48295	1.49218	1.47131
			NET_D	MIX_C		INT_B	NET_D		INT_B	NET_E
3.0	0.0014	8.33653	8.34257	8.3348	4.16385	4.16492	4.1551	2.39126	2.39596	2.38668
			NET_E	CONV_B		INT_B	NET_E		RES_E	MIX_B
3.0	0.004	8.38258	8.38929	8.38097	4.11289	4.11335	4.10341	2.32897	2.33377	2.31896
			NET_E	CONV_B		RES_D	NET_D		RES_E	MIX_C
3.0	0.014	8.4783	8.48683	8.46465	4.03285	4.03675	4.023	2.19327	2.19994	2.18364
			NET_E	MIX_C		INT_B	NET_E		INT_B	NET_E
4.0	0.0014	8.05646	8.06074	8.05414	4.23101	4.23191	4.2228	2.82949	2.83225	2.82589
			NET_D	CONV_B		INT_B	NET_E		RES_E	MIX_C
4.0	0.004	8.08919	8.09483	8.08651	4.18668	4.18711	4.17771	2.78068	2.78328	2.77369
			NET_D	CONV_B		CONV_B	NET_E		RES_E	MIX_C
4.0	0.014	8.1585	8.16637	8.14314	4.11737	4.12055	4.10778	2.67744	2.68223	2.66983
			NET_D	MIX_C		INT_B	NET_E		INT_B	NET_E
5.0	0.0014	7.85237	7.85575	7.84924	4.28213	4.28288	4.27425	3.14901	3.15038	3.14585
			NET_D	CONV_B		INT_B	NET_E		RES_E	NET_E
5.0	0.004	7.87523	7.87977	7.87216	4.2427	4.2429	4.23427	3.11009	3.1113	3.10552
			NET_D	CONV_B		RES_D	NET_E		RES_E	NET_E
5.0	0.014	7.9229	7.93031	7.90723	4.18139	4.18409	4.17221	3.03177	3.03651	3.02452
			NET_E	MIX_C		INT_B	NET_D		MIX_C	NET_D
6.0	0.0014	7.6957	7.69813	7.69254	4.32375	4.32449	4.31618	3.4001	3.40382	3.39756
			NET_E	CONV_B		INT_B	NET_E		RES_E	NET_E
6.0	0.004	7.71118	7.71487	7.70815	4.28791	4.28809	4.28002	3.36539	3.36866	3.36192
			NET_E	CONV_B		INT_B	NET_D		RES_E	NET_E
6.0	0.014	7.74256	7.74938	7.7265	4.23244	4.23472	4.22379	3.30187	3.30813	3.2964
			NET_D	MIX_C		INT_B	NET_D		MIX_C	NET_D
7.0	0.0014	7.57042	7.57267	7.56714	4.35917	4.35976	4.35169	3.61941	3.62356	3.61486
			NET_D	CONV_B		INT_B	NET_E		RES_E	CONV_B
7.0	0.004	7.58123	7.58416	7.57791	4.32621	4.32638	4.31853	3.58856	3.59359	3.58434
			NET_D	MIX_C		INT_B	NET_E		RES_E	CONV_B
7.0	0.014	7.6004	7.60625	7.58383	4.27553	4.27769	4.26728	3.53157	3.54045	3.52778
			NET_D	MIX_C		INT_B	NET_D		MIX_C	CONV_B
8.0	0.0014	7.46794	7.46971	7.46472	4.38817	4.38886	4.38072	3.81045	3.81508	3.8048
			NET_D	CONV_B		INT_B	NET_D		RES_E	RES_D
8.0	0.004	7.47506	7.47785	7.47149	4.35765	4.35783	4.34988	3.78411	3.7881	3.77912
			NET_D	MIX_C		INT_B	NET_E		RES_E	CONV_B
8.0	0.014	7.48501	7.4903	7.46822	4.31136	4.31321	4.30302	3.73607	3.7463	3.73099
			NET_D	MIX_C		INT_B	NET_E		MIX_C	CONV_B

**Note.** Columns mark mass, initial metal abundance, nuclear age of the reference model, maximal and minimal values of nuclear age for a given mass and Z with corresponding set in the subrow, effective temperature of the reference model, maximal and minimal values of effective temperature for a given mass and Z with corresponding set in the subrow, log of luminosity (log  $L$ ) of the reference model, and maximal and minimal values of log  $L$  for a given mass and Z with corresponding set in the subrow. Luminosity is given in solar units and effective temperature in kelvin.



**Table 9**  
Comparison of Physical Quantities (Nuclear Ages, Effective Temperatures, Luminosities; All in Logarithms) of Models 2–8  $M_{\odot}$  at the tRGB

Mass	Z	log age <sup>ref</sup>	log age <sup>max</sup>	log age <sup>min</sup>	log $T_{\text{eff}}^{\text{ref}}$	log $T_{\text{eff}}^{\text{max}}$	log $T_{\text{eff}}^{\text{min}}$	log $L^{\text{ref}}$	log $L^{\text{max}}$	log $L^{\text{min}}$
2.0	0.0014	8.83484	8.83757	8.83272	3.62684	3.63846	3.62552	3.20242	3.20844	3.16884
			MIX_B	CONV_B		ATM_C	MLT_D		MIX_B	CONV_B
2.0	0.004	8.89128	8.89611	8.88819	3.5899	3.61861	3.58846	3.27021	3.27815	3.17956
			MIX_B	CONV_B		ATM_C	MLT_D		RES_D	CONV_B
2.0	0.014	9.01528	9.02083	9.0059	3.53733	3.56137	3.53586	3.35199	3.35636	3.33746
			NET_D	MIX_C		ATM_C	MLT_D		RES_D	CONV_B
3.0	0.0014	8.35877	8.364	8.35771	3.70572	3.70724	3.70345	2.43734	2.47131	2.43172
			NET_E	CONV_B		ATM_B	NET_D		NET_D	CONV_B
3.0	0.004	8.40429	8.41017	8.40328	3.6826	3.68907	3.67995	2.45942	2.49431	2.45542
			NET_D	RES_D		ATM_C	NET_E		NET_E	CONV_B
3.0	0.014	8.49879	8.50651	8.4862	3.645	3.66124	3.64267	2.45713	2.48518	2.45479
			NET_D	MIX_C		ATM_C	NET_D		NET_D	RES_E
4.0	0.0014	8.07223	8.07611	8.07049	3.69919	3.70091	3.69333	2.7909	2.81848	2.78359
			NET_E	CONV_B		ATM_B	ATM_D		NET_D	CONV_B
4.0	0.004	8.10507	8.11023	8.10301	3.67507	3.68279	3.67239	2.79299	2.82346	2.78254
			NET_E	CONV_B		ATM_C	NET_D		NET_D	CONV_B
4.0	0.014	8.17417	8.18134	8.15942	3.63793	3.65781	3.63542	2.77408	2.80359	2.76687
			NET_E	MIX_C		ATM_B	NET_D		NET_D	CONV_B
5.0	0.0014	7.86437	7.86733	7.8619	3.69108	3.69354	3.6881	3.09612	3.12121	3.08537
			NET_E	CONV_B		ATM_E	NET_D		NET_D	CONV_B
5.0	0.004	7.88723	7.8915	7.88476	3.6652	3.67842	3.66261	3.09065	3.1174	3.07987
			NET_E	CONV_B		ATM_D	NET_D		NET_D	CONV_B
5.0	0.014	7.93563	7.94247	7.92023	3.62789	3.64566	3.62517	3.06198	3.09339	3.05206
			NET_E	MIX_C		ATM_C	NET_D		NET_D	CONV_B
6.0	0.0014	7.70506	7.70701	7.70244	3.6828	3.68586	3.6793	3.36113	3.38493	3.34971
			NET_E	CONV_B		ATM_E	NET_D		NET_D	CONV_B
6.0	0.004	7.72042	7.72392	7.71777	3.6549	3.6657	3.65228	3.35126	3.37617	3.34145
			NET_E	CONV_B		ATM_C	NET_D		NET_D	CONV_B
6.0	0.014	7.75268	7.75914	7.73672	3.61718	3.6356	3.61455	3.32001	3.34981	3.31029
			NET_E	MIX_C		ATM_C	NET_D		NET_E	CONV_B
7.0	0.0014	7.57833	7.57963	7.576	3.67519	3.67859	3.67091	3.59055	3.61316	3.57805
			NET_D	CONV_B		ATM_E	NET_D		NET_D	CONV_B
7.0	0.004	7.58826	7.59108	7.585	3.64443	3.65691	3.64202	3.58356	3.6055	3.57313
			NET_D	MIX_C		ATM_C	NET_D		NET_D	CONV_B
7.0	0.014	7.60823	7.61386	7.59169	3.60662	3.62573	3.6042	3.55132	3.57809	3.54017
			NET_E	MIX_C		ATM_C	NET_D		NET_D	CONV_B
8.0	0.0014	7.47373	7.47549	7.4679	3.96413	4.3846	3.85683	3.8947	3.9095	3.81699
			RES_D	RES_B		RES_B	CONV_B		RES_D	RES_B
8.0	0.004	7.48064	7.48324	7.47738	3.63813	3.65224	3.63357	3.75839	3.79867	3.71835
			NET_E	MIX_C		ATM_C	NET_E		NET_E	RES_D
8.0	0.014	7.49109	7.49626	7.47433	3.59689	3.61651	3.59465	3.75662	3.7812	3.74478
			NET_E	MIX_C		ATM_C	NET_D		NET_D	CONV_B

**Note.** Columns mark mass, initial metal abundance, nuclear age of the reference model, maximal and minimal values of nuclear age for a given mass and Z with corresponding set in the subrow, effective temperature of the reference model, maximal and minimal values of effective temperature for a given mass and Z with corresponding set in the subrow, log of luminosity (log  $L$ ) of the reference model, and maximal and minimal values of log  $L$  for a given mass and Z with corresponding set in the subrow.

**Table 10**  
Comparison of Physical Quantities (Nuclear Ages, Effective Temperatures, Luminosities; All in Logarithms) of Models 2–8  $M_{\odot}$  at mChEB

Mass	Z	log age <sup>ref</sup>	log age <sup>max</sup>	log age <sup>min</sup>	log $T_{\text{eff}}^{\text{ref}}$	log $T_{\text{eff}}^{\text{max}}$	log $T_{\text{eff}}^{\text{min}}$	log $L^{\text{ref}}$	log $L^{\text{max}}$	log $L^{\text{min}}$
2.0	0.0014	8.86437	8.86807	8.85184	3.74423	3.74528	3.73834	2.1557	2.16132	2.09264
			NET_E	CONV_C		INT_B	NET_D		INT_B	CONV_C
2.0	0.004	8.91826	8.92339	8.90646	3.71541	3.71703	3.71378	1.94127	1.94433	1.90551
			MIX_B	CONV_C		ATM_D	NET_D		RES_D	CONV_C
2.0	0.014	9.03581	9.04264	9.02717	3.68267	3.6947	3.68147	1.78727	1.79591	1.77724
			NET_E	CONV_C		ATM_C	NET_D		ATM_C	CONV_C
3.0	0.0014	8.43694	8.44208	8.41381	3.90473	3.90851	3.8454	2.64836	2.65279	2.55016
			NET_E	CONV_C		INT_B	CONV_C		INT_B	CONV_C
3.0	0.004	8.48485	8.49003	8.4574	3.78592	3.78739	3.71977	2.45062	2.45274	2.20648
			NET_E	CONV_C		DIFF_B	CONV_C		NET_C	CONV_C
3.0	0.014	8.58734	8.59737	8.55293	3.70619	3.71459	3.68686	1.97198	2.05288	1.91301
			NET_E	CONV_C		ATM_C	CONV_B		CONV_B	CONV_C
4.0	0.0014	8.13482	8.13985	8.1192	3.99822	4.0022	3.95663	3.07498	3.07767	3.017
			NET_E	CONV_C		INT_B	CONV_C		INT_B	CONV_C
4.0	0.004	8.17144	8.17521	8.15165	3.75321	3.76201	3.70049	2.84975	2.85546	2.68808
			NET_E	CONV_C		CONV_B	CONV_C		NET_C	CONV_C
4.0	0.014	8.23734	8.24451	8.2174	3.72978	3.7382	3.66657	2.61909	2.63447	2.42583
			NET_E	CONV_C		ATM_B	CONV_B		ATM_B	CONV_C
5.0	0.0014	7.9157	7.92021	7.90593	4.06212	4.06658	4.02838	3.39231	3.39538	3.36001
			NET_E	CONV_C		CONV_B	NET_D		RES_E	CONV_C
5.0	0.004	7.94368	7.94759	7.93009	3.86448	3.87736	3.71937	3.23798	3.24329	3.1237
			NET_E	CONV_C		CONV_B	CONV_C		NET_C	CONV_C
5.0	0.014	7.99036	7.99626	7.97599	3.65784	3.67267	3.65001	2.85341	2.90532	2.83194
			NET_E	MIX_C		ATM_C	CONV_C		CONV_B	MIX_B
6.0	0.0014	7.74936	7.7527	7.74233	4.10939	4.11339	4.07794	3.64759	3.65054	3.62659
			NET_E	CONV_C		CONV_B	NET_D		RES_E	CONV_C
6.0	0.004	7.76926	7.77246	7.76019	3.94358	3.955	3.8647	3.53348	3.53826	3.48402
			NET_E	CONV_C		CONV_B	NET_D		NET_C	CONV_C
6.0	0.014	7.80164	7.80696	7.78598	3.63811	3.65529	3.63389	3.17659	3.20145	3.14216
			NET_E	MIX_C		ATM_C	CONV_C		CONV_B	NET_E
7.0	0.0014	7.61712	7.62007	7.61176	4.14647	4.15001	4.11576	3.85765	3.85974	3.84304
			NET_E	CONV_C		CONV_B	NET_D		RES_E	CONV_C
7.0	0.004	7.63152	7.63425	7.62492	3.99836	4.008	3.93072	3.76964	3.77288	3.73999
			NET_E	CONV_C		CONV_B	NET_D		RES_E	CONV_C
7.0	0.014	7.65211	7.65678	7.6361	3.62516	3.64257	3.62199	3.42371	3.45319	3.39133
			NET_E	MIX_C		ATM_C	CONV_C		CONV_B	NET_E
8.0	0.0014	7.51034	7.51806	7.50622	4.1763	4.19107	4.14053	4.04059	4.0559	4.03035
			RES_B	CONV_C		RES_D	NET_D		RES_B	CONV_C
8.0	0.004	7.52035	7.52405	7.51517	4.03307	4.05328	3.95683	3.96336	3.9729	3.93901
			RES_B	CONV_C		RES_D	NET_D		RES_B	NET_D
8.0	0.014	7.53067	7.53533	7.51426	3.61516	3.63292	3.61033	3.62617	3.67084	3.59042
			NET_E	MIX_C		ATM_C	CONV_B		CONV_B	NET_E

**Note.** Columns mark mass, initial metal abundance, nuclear age of the reference model, maximal and minimal values of nuclear age for a given mass and Z with corresponding set in the subrow, effective temperature of the reference model, maximal and minimal values of effective temperature for a given mass and Z with corresponding set in the subrow, log of luminosity (log  $L$ ) of the reference model, and maximal and minimal values of log  $L$  for a given mass and Z with corresponding set in the subrow.

**Table 11**  
Comparison of Physical Quantities (Nuclear Ages, Effective Temperatures, Luminosities; All in Logarithms) of Models 2–8  $M_{\odot}$  at eCHeB

Mass	Z	log age <sup>ref</sup>	log age <sup>max</sup>	log age <sup>min</sup>	log $T_{\text{eff}}^{\text{ref}}$	log $T_{\text{eff}}^{\text{max}}$	log $T_{\text{eff}}^{\text{min}}$	log $L^{\text{ref}}$	log $L^{\text{max}}$	log $L^{\text{min}}$
2.0	0.0014	8.88948	8.89551	8.87369	3.7083	3.71448	3.70075	2.25525	2.33363	2.16175
			NET_E	CONV_C		CONV_C	RES_E		RES_E	CONV_C
2.0	0.004	8.94506	8.95164	8.92841	3.69092	3.69814	3.67705	2.14725	2.30503	2.08203
			NET_E	CONV_C		ATM_C	RES_E		RES_E	CONV_C
2.0	0.014	9.05948	9.06734	9.04561	3.65798	3.67213	3.64455	2.06587	2.22187	2.01731
			NET_E	CONV_C		ATM_C	RES_E		RES_E	CONV_C
3.0	0.0014	8.47261	8.4788	8.45001	3.71391	3.74024	3.70389	2.60513	2.63487	2.58724
			NET_E	CONV_C		CONV_C	RES_E		RES_E	MIX_C
3.0	0.004	8.52846	8.5349	8.50073	3.6941	3.7081	3.68214	2.4428	2.54775	2.30119
			NET_E	CONV_C		CONV_C	RES_E		RES_E	CONV_C
3.0	0.014	8.64988	8.66219	8.61242	3.67385	3.69059	3.66308	2.16732	2.28622	2.04978
			NET_E	CONV_C		DIFF_B	RES_E		RES_E	DIFF_B
4.0	0.0014	8.1684	8.17423	8.1483	3.78125	3.9279	3.73525	3.08383	3.09932	3.04857
			NET_E	CONV_C		CONV_C	NET_D		CONV_C	MIX_C
4.0	0.004	8.21221	8.21692	8.18747	3.68004	3.68917	3.66571	2.86125	2.97118	2.76612
			NET_E	CONV_C		CONV_C	RES_E		RES_E	CONV_C
4.0	0.014	8.28486	8.29386	8.25678	3.65888	3.67743	3.64154	2.61273	2.77282	2.48397
			NET_E	CONV_C		ATM_B	CONV_B		CONV_B	CONV_C
5.0	0.0014	7.94925	7.95432	7.93074	3.88809	4.01757	3.76284	3.42182	3.43504	3.37454
			NET_E	CONV_C		CONV_C	RES_E		CONV_C	RES_E
5.0	0.004	7.98234	7.98716	7.96272	3.67656	3.68567	3.66072	3.15273	3.23044	3.14462
			NET_E	CONV_C		ATM_D	RES_E		RES_E	CONV_B
5.0	0.014	8.03473	8.04039	8.00902	3.64584	3.65866	3.62486	2.94775	3.13086	2.90871
			NET_E	CONV_C		ATM_C	CONV_B		CONV_B	CONV_C
6.0	0.0014	7.78199	7.78602	7.76596	3.95015	4.03424	3.86619	3.68119	3.70511	3.66349
			NET_E	CONV_C		CONV_C	RES_E		CONV_C	RES_E
6.0	0.004	7.8065	7.81078	7.78865	3.68525	3.69093	3.65074	3.44005	3.48297	3.40549
			NET_E	CONV_C		CONV_B	NET_D		CONV_C	RES_E
6.0	0.014	7.84304	7.84924	7.82025	3.61504	3.63619	3.6093	3.37588	3.43281	3.23444
			NET_E	CONV_C		MIX_B	RES_E		RES_E	CONV_C
7.0	0.0014	7.64874	7.65263	7.63553	3.99276	4.03797	3.91621	3.89081	3.91977	3.87919
			NET_E	CONV_C		CONV_C	RES_E		CONV_C	MIX_C
7.0	0.004	7.66732	7.6714	7.65124	3.69976	3.72249	3.64719	3.70363	3.71797	3.60755
			NET_E	CONV_C		CONV_B	NET_D		CONV_B	MIX_C
7.0	0.014	7.69176	7.69773	7.67213	3.60292	3.62896	3.59768	3.61902	3.67032	3.45605
			NET_E	CONV_C		MIX_B	RES_E		RES_E	MIX_B
8.0	0.0014	7.54087	7.5498	7.53201	4.0213	4.03651	3.9356	4.07619	4.10308	4.06197
			RES_B	CONV_C		RES_D	RES_E		RES_B	CONV_B
8.0	0.004	7.55442	7.55827	7.54127	3.76709	3.80194	3.63738	3.93486	3.95261	3.83761
			RES_D	CONV_C		NET_B	NET_D		NET_B	MIX_C
8.0	0.014	7.57083	7.57533	7.55158	3.60101	3.65761	3.58869	3.75272	3.86621	3.61473
			NET_E	CONV_C		NET_C	CONV_B		CONV_B	MIX_B

**Note.** Columns mark mass, initial metal abundance, nuclear age of the reference model, maximal and minimal values of nuclear age for a given mass and Z with corresponding set in the subrow, effective temperature of the reference model, maximal and minimal values of effective temperature for a given mass and Z with corresponding set in the subrow, log of luminosity (log  $L$ ) of the reference model, and maximal and minimal values of log  $L$  for a given mass and Z with corresponding set in the subrow.

**Table 12**  
Comparison of Physical Quantities (Nuclear Ages, Effective Temperatures, Luminosities; All in Logarithms) of Models 2–8  $M_{\odot}$  at mIS

Mass	Z	log age <sup>ref</sup>	log age <sup>max</sup>	log age <sup>min</sup>	log $T_{\text{eff}}^{\text{ref}}$	log $T_{\text{eff}}^{\text{max}}$	log $T_{\text{eff}}^{\text{min}}$	log $L^{\text{ref}}$	log $L^{\text{max}}$	log $L^{\text{min}}$
2.0	0.0014	...	...	...	...	...	...	...	...	...
2.0	0.004	...	...	...	...	...	...	...	...	...
2.0	0.014	...	...	...	...	...	...	...	...	...
3.0	0.0014	8.40723	8.4231 NET_D	8.40449 INT_B	3.80561	3.80578 RES_C	3.80446 NET_D	2.51022	2.53853 NET_D	2.50612 RES_C
3.0	0.004	...	...	...	...	...	...	...	...	...
3.0	0.014	...	...	...	...	...	...	...	...	...
4.0	0.0014	8.09593	8.10827 NET_D	8.09346 CONV_B	3.79055	3.79081 CONV_B	3.78967 NET_D	2.87939	2.90078 NET_D	2.8729 CONV_B
4.0	0.004	8.17689	8.19703 NET_D	8.17485 CONV_B	3.78959	3.78986 CONV_B	3.78798 NET_D	2.88725	2.92622 NET_D	2.88074 CONV_B
4.0	0.014	...	...	...	...	...	...	...	...	...
5.0	0.0014	7.87629	7.88528 NET_D	7.87303 CONV_B	3.77786	3.77818 CONV_B	3.77736 NET_D	3.1903	3.20243 NET_D	3.18237 CONV_B
5.0	0.004	7.93438	7.94798 NET_D	7.93138 CONV_B	3.77783	3.77821 CONV_B	3.77682 NET_D	3.17206	3.1964 NET_D	3.16272 CONV_B
5.0	0.014	...	...	...	...	...	...	...	...	...
6.0	0.0014	7.71227	7.71916 NET_D	7.70894 CONV_B	3.7666	3.76694 CONV_B	3.76627 NET_D	3.46623	3.47425 NET_D	3.45794 CONV_B
6.0	0.004	7.75431	7.7647 NET_D	7.75135 CONV_B	3.7672	3.76756 CONV_B	3.76661 NET_D	3.42939	3.44379 NET_D	3.42067 CONV_B
6.0	0.014	...	...	...	...	...	...	...	...	...
7.0	0.0014	7.58318	7.58933 NET_D	7.57962 CONV_B	3.75685	3.75721 CONV_B	3.75653 NET_D	3.70508	3.71287 NET_D	3.6963 CONV_B
7.0	0.004	7.61674	7.62559 NET_D	7.61375 CONV_B	3.75715	3.75751 CONV_B	3.7567 NET_D	3.67275	3.68366 NET_D	3.66403 CONV_B
7.0	0.014	...	...	...	...	...	...	...	...	...
8.0	0.0014	...	...	...	...	...	...	...	...	...
8.0	0.004	7.50595	7.51456 NET_D	7.50274 NET_B	3.74849	3.74948 MIX_C	3.7479 NET_D	3.88259	3.89678 NET_D	3.85857 MIX_C
8.0	0.014	...	...	...	...	...	...	...	...	...

**Note.** Columns mark mass, initial metal abundance, nuclear age of the reference model, maximal and minimal values of nuclear age for a given mass and Z with corresponding set in the subrow, effective temperature of the reference model, maximal and minimal values of effective temperature for a given mass and Z with corresponding set in the subrow, log of luminosity (log  $L$ ) of the reference model, and maximal and minimal values of log  $L$  for a given mass and Z with corresponding set in the subrow.



**Table 13**Comparison of Physical Quantities (Nuclear Ages, Effective Temperatures, Luminosities; All in Logarithms) of Models 2–8  $M_{\odot}$  with Convective Core Overshooting ( $f = 0.02$ ) at TAMS

Mass	Z	log age <sup>ref</sup>	log age <sup>max</sup>	log age <sup>min</sup>	log $T_{\text{eff}}^{\text{ref}}$	log $T_{\text{eff}}^{\text{max}}$	log $T_{\text{eff}}^{\text{min}}$	log $L^{\text{ref}}$	log $L^{\text{max}}$	log $L^{\text{min}}$
2.0	0.0014	8.85468	8.8632	8.83315	4.06355	4.0649	4.05402	1.84982	1.85208	1.8024
			NET_D	ATM_C		INT_B	NET_D		MLT_D	ATM_C
2.0	0.004	8.91711	8.92631	8.89656	4.00023	4.00231	3.9891	1.76722	1.77007	1.72063
			NET_E	ATM_C		ATM_B	MIX_C		MLT_D	ATM_C
2.0	0.014	9.04623	9.05599	9.02426	3.90175	3.9076	3.89116	1.58251	1.59174	1.53865
			NET_E	ATM_C		INT_B	NET_E		INT_B	ATM_C
3.0	0.0014	8.4349	8.44068	8.41577	4.16181	4.16384	4.15315	2.52505	2.52832	2.48172
			NET_E	ATM_D		ATM_D	NET_D		MLT_D	ATM_D
3.0	0.004	8.48015	8.48686	8.46115	4.10773	4.11069	4.09818	2.45911	2.46229	2.41554
			NET_D	ATM_D		ATM_D	NET_E		MLT_D	ATM_D
3.0	0.014	8.57405	8.58271	8.55569	4.02248	4.02716	4.01231	2.31695	2.32481	2.2758
			NET_D	ATM_D		ATM_D	NET_E		INT_B	ATM_D
4.0	0.0014	8.15366	8.15737	8.13694	4.2311	4.23338	4.22274	2.97361	2.97533	2.93469
			NET_D	ATM_D		ATM_D	NET_D		RES_C	ATM_D
4.0	0.004	8.18657	8.19139	8.16929	4.18449	4.1875	4.1755	2.92275	2.9243	2.8828
			NET_D	ATM_D		ATM_D	NET_D		RES_C	ATM_D
4.0	0.014	8.25446	8.2619	8.23525	4.11104	4.11517	4.1009	2.81444	2.82006	2.773
			NET_E	MIX_C		ATM_D	NET_D		INT_B	ATM_D
5.0	0.0014	7.94478	7.94767	7.93239	4.28236	4.28453	4.27441	3.30122	3.30313	3.27327
			NET_E	ATM_D		ATM_D	NET_E		RES_C	ATM_D
5.0	0.004	7.96866	7.97263	7.95488	4.24156	4.24423	4.23283	3.26179	3.26348	3.22999
			NET_D	ATM_D		ATM_D	NET_D		RES_C	ATM_D
5.0	0.014	8.01687	8.02304	7.99925	4.17785	4.18136	4.16814	3.17904	3.18326	3.14297
			NET_E	MIX_C		ATM_D	NET_D		INT_B	ATM_D
6.0	0.0014	7.7834	7.78562	7.77464	4.32213	4.324	4.31435	3.56317	3.56453	3.54374
			NET_D	ATM_D		ATM_D	NET_D		RES_C	ATM_D
6.0	0.004	7.80034	7.80364	7.79026	4.28543	4.2878	4.27704	3.52987	3.53153	3.50765
			NET_E	ATM_D		ATM_D	NET_D		RES_C	ATM_D
6.0	0.014	7.83312	7.83866	7.81699	4.22889	4.23195	4.21943	3.46353	3.47032	3.43596
			NET_D	MIX_C		ATM_D	NET_E		MIX_C	ATM_D
7.0	0.0014	7.65364	7.6555	7.64823	4.35422	4.35562	4.34653	3.7796	3.78111	3.76788
			NET_D	ATM_D		ATM_D	NET_D		RES_C	ATM_D
7.0	0.004	7.66592	7.66867	7.65915	4.32035	4.32226	4.31216	3.75176	3.7534	3.73726
			NET_E	ATM_D		ATM_D	NET_E		RES_C	ATM_D
7.0	0.014	7.68706	7.69202	7.67072	4.26901	4.27171	4.25973	3.69822	3.70698	3.67848
			NET_D	MIX_C		ATM_D	NET_E		MIX_C	ATM_D
8.0	0.0014	7.54676	7.54839	7.54442	4.38062	4.38139	4.37302	3.96325	3.96477	3.95858
			NET_D	ATM_D		ATM_D	NET_D		RES_C	ATM_D
8.0	0.004	7.55564	7.55803	7.55199	4.34882	4.35006	4.34074	3.93994	3.94156	3.93247
			NET_D	ATM_D		ATM_D	NET_D		ATM_C	ATM_D
8.0	0.014	7.56786	7.57228	7.5513	4.30124	4.30339	4.29212	3.89576	3.90552	3.88331
			NET_D	MIX_C		ATM_D	NET_D		MIX_C	ATM_D

**Note.** Columns mark mass, initial metal abundance, nuclear age of the reference model, maximal and minimal values of nuclear age for a given mass and Z with corresponding set in the subrow, effective temperature of the reference model, maximal and minimal values of effective temperature for a given mass and Z with corresponding set in the subrow, log of luminosity (log  $L$ ) of the reference model, and maximal and minimal values of log  $L$  for a given mass and Z with corresponding set in the subrow.

**Table 14**Comparison of Physical Quantities (Nuclear Ages, Effective Temperatures, Luminosities; All in Logarithms) of Models 2–8  $M_{\odot}$  with Convective Core Overshooting ( $f = 0.02$ ) at the tRGB

Mass	Z	log age <sup>ref</sup>	log age <sup>max</sup>	log age <sup>min</sup>	log $T_{\text{eff}}^{\text{ref}}$	log $T_{\text{eff}}^{\text{max}}$	log $T_{\text{eff}}^{\text{min}}$	log $L^{\text{ref}}$	log $L^{\text{max}}$	log $L^{\text{min}}$
2.0	0.0014	8.86547	8.8731	8.85058	3.687	3.68917	3.68455	2.41516	2.4501	2.40381
			NET_D	ATM_C		ATM_E	ATM_B		NET_D	RES_E
2.0	0.004	8.92832	8.93669	8.91376	3.65697	3.67251	3.65426	2.48037	2.5151	2.47982
			NET_D	ATM_C		ATM_C	NET_D		NET_D	MLT_C
2.0	0.014	9.05797	9.06704	9.04941	3.62579	3.63596	3.58342	2.3793	3.06356	2.3578
			NET_E	ATM_C		ATM_E	MIX_B		ATM_C	ATM_E
3.0	0.0014	8.43922	8.44491	8.42183	3.68376	3.68908	3.68159	2.79677	2.8258	2.71541
			NET_E	ATM_D		ATM_C	NET_E		NET_D	ATM_D
3.0	0.004	8.48475	8.49133	8.46752	3.65923	3.67839	3.65685	2.78924	2.81866	2.71718
			NET_E	ATM_D		ATM_D	NET_D		NET_D	ATM_D
3.0	0.014	8.57914	8.58757	8.56243	3.62362	3.65613	3.62087	2.74797	2.77611	2.68661
			NET_E	MIX_C		ATM_D	CONV_B		NET_D	ATM_D
4.0	0.0014	8.15669	8.16041	8.14096	3.67231	3.67925	3.67027	3.18334	3.20708	3.10082
			NET_E	ATM_D		ATM_C	NET_D		NET_D	ATM_D
4.0	0.004	8.18982	8.19463	8.1736	3.64575	3.66893	3.64353	3.17104	3.19621	3.09112
			NET_E	ATM_D		ATM_D	NET_D		NET_D	ATM_D
4.0	0.014	8.25821	8.26554	8.23942	3.61081	3.64554	3.6081	3.12035	3.15114	3.04659
			NET_D	MIX_C		ATM_D	NET_D		NET_D	ATM_D
5.0	0.0014	7.94733	7.95025	7.93551	3.66196	3.66963	3.65996	3.4861	3.50715	3.42331
			NET_E	ATM_D		ATM_D	NET_D		NET_D	ATM_D
5.0	0.004	7.97137	7.97533	7.95826	3.63328	3.659	3.63113	3.47836	3.50139	3.4102
			NET_E	ATM_D		ATM_D	NET_D		NET_D	ATM_D
5.0	0.014	8.0199	8.02602	8.00252	3.59708	3.63282	3.59475	3.43717	3.46294	3.36378
			NET_D	MIX_C		ATM_D	NET_D		NET_D	ATM_D
6.0	0.0014	7.78557	7.78778	7.77709	3.65267	3.6622	3.65069	3.73639	3.75534	3.69217
			NET_E	ATM_D		ATM_D	NET_D		NET_D	ATM_D
6.0	0.004	7.80264	7.80594	7.79291	3.62282	3.64959	3.62084	3.72975	3.75052	3.68072
			NET_E	ATM_D		ATM_D	NET_D		NET_D	ATM_D
6.0	0.014	7.8357	7.84119	7.81962	3.58557	3.62052	3.58337	3.69425	3.71812	3.63569
			NET_D	MIX_C		ATM_D	NET_D		NET_D	ATM_D
7.0	0.0014	7.65552	7.65738	7.65023	3.64475	3.6558	3.64278	3.94464	3.96223	3.91743
			NET_D	ATM_D		ATM_D	NET_E		NET_D	ATM_D
7.0	0.004	7.66791	7.67065	7.6613	3.61401	3.6411	3.61223	3.94218	3.96032	3.91014
			NET_E	ATM_D		ATM_D	NET_D		NET_D	ATM_D
7.0	0.014	7.68926	7.69421	7.67296	3.57578	3.60934	3.57368	3.91116	3.93371	3.86992
			NET_E	MIX_C		ATM_D	NET_D		NET_D	ATM_D
8.0	0.0014	7.54839	7.55003	7.54609	3.63794	3.65016	3.63604	4.12261	4.13891	4.11053
			NET_E	ATM_D		ATM_D	NET_D		NET_D	ATM_D
8.0	0.004	7.55738	7.55976	7.55377	3.60676	3.63363	3.60509	4.12302	4.13982	4.10633
			NET_E	ATM_D		ATM_D	NET_D		NET_D	ATM_D
8.0	0.014	7.56976	7.57417	7.55325	3.56752	3.59968	3.56558	4.0973	4.11759	4.05855
			NET_E	MIX_C		ATM_D	NET_D		NET_D	CONV_D

**Note.** Columns mark mass, initial metal abundance, nuclear age of the reference model, maximal and minimal values of nuclear age for a given mass and Z with corresponding set in the subrow, effective temperature of the reference model, maximal and minimal values of effective temperature for a given mass and Z with corresponding set in the subrow, log of luminosity (log  $L$ ) of the reference model, and maximal and minimal values of log  $L$  for a given mass and Z with corresponding set in the subrow.

**Table 15**

Comparison of Physical Quantities (Nuclear Ages, Effective Temperatures, Luminosities; All in Logarithms) of Models 2–8  $M_{\odot}$  with Convective Core Overshooting ( $f = 0.02$ ) at mChEB

Mass	Z	log age <sup>ref</sup>	log age <sup>max</sup>	log age <sup>min</sup>	log $T_{\text{eff}}^{\text{ref}}$	log $T_{\text{eff}}^{\text{max}}$	log $T_{\text{eff}}^{\text{min}}$	log $L^{\text{ref}}$	log $L^{\text{max}}$	log $L^{\text{min}}$
2.0	0.0014	8.92145	8.92805	8.89994	3.75119	3.75224	3.7398	2.08223	2.08978	1.97441
			NET_E	CONV_C		INT_B	ATM_B		INT_B	CONV_C
2.0	0.004	8.9886	8.99675	8.96492	3.723	3.72431	3.71624	1.80055	1.85049	1.72543
			NET_E	CONV_C		ATM_E	CONV_B		CONV_B	CONV_C
2.0	0.014	9.11912	9.12879	9.07706	3.69314	3.7068	3.6901	1.58817	1.72932	1.54961
			NET_E	ATM_C		ATM_C	CONV_B		ATM_C	CONV_C
3.0	0.0014	8.47275	8.4776	8.46267	3.73848	3.76902	3.70991	2.72466	2.73173	2.62656
			NET_E	CONV_C		ATM_D	CONV_C		INT_B	CONV_C
3.0	0.004	8.51843	8.5248	8.5075	3.74698	3.75076	3.69127	2.5896	2.59254	2.43055
			NET_E	CONV_C		ATM_C	CONV_B		MLT_D	CONV_C
3.0	0.014	8.61824	8.62716	8.60333	3.69245	3.71258	3.65824	2.14177	2.41056	2.10557
			NET_E	CONV_C		ATM_D	CONV_B		CONV_B	ATM_D
4.0	0.0014	8.18339	8.18693	8.17346	3.77968	3.8307	3.69977	3.18265	3.18733	3.10543
			NET_E	ATM_D		ATM_D	CONV_C		INT_B	CONV_C
4.0	0.004	8.2164	8.22075	8.20593	3.67459	3.68784	3.66767	2.9918	3.0264	2.94517
			NET_E	ATM_D		ATM_D	CONV_C		CONV_B	ATM_D
4.0	0.014	8.28517	8.29251	8.26935	3.68613	3.70881	3.63129	2.75159	2.94694	2.67383
			NET_E	MIX_C		ATM_D	CONV_B		CONV_B	CONV_C
5.0	0.0014	7.97082	7.97354	7.96244	3.87374	3.90573	3.77496	3.5192	3.52136	3.48863
			NET_E	ATM_D		ATM_D	CONV_C		INT_B	CONV_C
5.0	0.004	7.99467	7.99836	7.98549	3.65671	3.6749	3.65253	3.34846	3.36257	3.31126
			NET_E	ATM_D		ATM_D	CONV_C		CONV_B	ATM_D
5.0	0.014	8.04291	8.04877	8.02675	3.65221	3.70874	3.61396	3.09809	3.30555	3.05883
			NET_E	MIX_C		NET_E	CONV_B		CONV_B	ATM_D
6.0	0.0014	7.80686	7.80913	7.80057	3.94393	3.96706	3.87134	3.78102	3.78247	3.76293
			NET_E	ATM_D		ATM_D	NET_D		INT_B	ATM_D
6.0	0.004	7.82404	7.82723	7.81675	3.64437	3.66567	3.64117	3.6168	3.628	3.59149
			NET_E	ATM_D		ATM_D	CONV_C		CONV_B	ATM_D
6.0	0.014	7.85697	7.86213	7.84135	3.62721	3.6575	3.60062	3.38725	3.58195	3.36323
			NET_E	MIX_C		ATM_D	CONV_B		CONV_B	ATM_D
7.0	0.0014	7.67516	7.67704	7.67103	3.99397	4.00861	3.92749	3.99122	3.99278	3.97979
			NET_E	ATM_D		ATM_D	NET_D		RES_C	ATM_D
7.0	0.004	7.68782	7.69043	7.6826	3.63416	3.65744	3.63163	3.83662	3.84762	3.82284
			NET_E	ATM_D		ATM_D	CONV_C		CONV_B	ATM_D
7.0	0.014	7.70929	7.71388	7.69323	3.61119	3.64196	3.58976	3.63961	3.8096	3.62385
			NET_E	MIX_C		ATM_D	CONV_B		CONV_B	NET_D
8.0	0.0014	7.56682	7.56856	7.56492	4.03089	4.03968	3.96788	4.16619	4.16796	4.15993
			NET_E	ATM_D		ATM_D	NET_D		ATM_C	CONV_C
8.0	0.004	7.57599	7.57833	7.57299	3.62532	3.64991	3.6235	4.02326	4.0343	4.01912
			NET_E	MIX_C		ATM_D	CONV_C		CONV_B	ATM_D
8.0	0.014	7.58871	7.59283	7.57238	3.59922	3.62955	3.58088	3.85104	4.00093	3.8314
			NET_E	MIX_C		ATM_D	CONV_B		CONV_B	NET_E

**Note.** Columns mark mass, initial metal abundance, nuclear age of the reference model, maximal and minimal values of nuclear age for a given mass and Z with corresponding set in the subrow, effective temperature of the reference model, maximal and minimal values of effective temperature for a given mass and Z with corresponding set in the subrow, log of luminosity (log  $L$ ) of the reference model, and maximal and minimal values of log  $L$  for a given mass and Z with corresponding set in the subrow.

**Table 16**

Comparison of Physical Quantities (Nuclear Ages, Effective Temperatures, Luminosities; All in Logarithms) of Models 2–8  $M_{\odot}$  with Convective Core Overshooting ( $f = 0.02$ ) at eChEB

Mass	Z	log age <sup>ref</sup>	log age <sup>max</sup>	log age <sup>min</sup>	log $T_{\text{eff}}^{\text{ref}}$	log $T_{\text{eff}}^{\text{max}}$	log $T_{\text{eff}}^{\text{min}}$	log $L^{\text{ref}}$	log $L^{\text{max}}$	log $L^{\text{min}}$
2.0	0.0014	8.95063	8.9583	8.93184	3.71087	3.7174	3.70367	2.19974	2.26992	2.07699
			NET_E	CONV_C		CONV_C	ATM_C		RES_E	CONV_C
2.0	0.004	9.02605	9.03286	9.00261	3.69407	3.7171	3.68675	2.07981	2.1677	1.89953
			NET_E	CONV_C		DIFF_B	RES_E		RES_E	DIFF_B
2.0	0.014	9.15788	9.1655	9.10425	3.66609	3.68619	3.65102	1.93767	2.12356	1.93113
			NET_E	ATM_C		ATM_C	RES_E		RES_E	CONV_C
3.0	0.0014	8.4948	8.49979	8.48083	3.69931	3.70392	3.68714	2.74858	2.83895	2.68705
			NET_E	CONV_C		ATM_C	RES_E		RES_E	ATM_D
3.0	0.004	8.54365	8.5511	8.52731	3.68399	3.69676	3.66861	2.6021	2.74135	2.49759
			NET_E	CONV_C		CONV_C	CONV_B		CONV_B	CONV_C
3.0	0.014	8.65439	8.66489	8.62958	3.66392	3.68952	3.63424	2.33482	2.66267	2.24296
			NET_E	CONV_B		ATM_D	CONV_B		CONV_B	CONV_C
4.0	0.0014	8.2039	8.20759	8.19168	3.68218	3.69692	3.6736	3.19305	3.25088	3.12312
			NET_E	CONV_C		CONV_C	RES_E		RES_E	ATM_D
4.0	0.004	8.23741	8.24204	8.22431	3.65352	3.67105	3.64167	3.14722	3.25746	3.03974
			NET_E	CONV_C		ATM_D	RES_E		RES_E	MIX_C
4.0	0.014	8.31128	8.31985	8.29548	3.6425	3.6729	3.60813	2.83176	3.18092	2.71981
			NET_E	CONV_C		ATM_D	CONV_B		CONV_B	CONV_C
5.0	0.0014	7.99098	7.99402	7.98071	3.6748	3.68252	3.66353	3.48703	3.55257	3.44046
			NET_E	CONV_C		ATM_D	NET_D		NET_D	ATM_D
5.0	0.004	8.0153	8.01916	8.00431	3.63295	3.6569	3.62665	3.52815	3.58612	3.42927
			NET_E	CONV_C		ATM_D	RES_E		RES_E	CONV_C
5.0	0.014	8.06591	8.07272	8.05166	3.62304	3.65556	3.59153	3.22258	3.52335	3.11663
			NET_E	MIX_C		ATM_D	CONV_B		CONV_B	CONV_C
6.0	0.0014	7.82674	7.82923	7.81786	3.67122	3.67916	3.65288	3.71809	3.80757	3.70468
			NET_E	CONV_C		ATM_D	NET_D		NET_D	ATM_D
6.0	0.004	7.84457	7.84791	7.83481	3.6212	3.64702	3.61651	3.78896	3.83184	3.71644
			NET_E	CONV_C		ATM_D	RES_E		RES_E	CONV_C
6.0	0.014	7.87928	7.88498	7.86455	3.60807	3.64108	3.57916	3.51907	3.78565	3.43741
			NET_E	MIX_C		ATM_D	CONV_B		CONV_B	CONV_C
7.0	0.0014	7.69433	7.69666	7.68701	3.66931	3.67581	3.64425	3.9151	4.0122	3.91462
			NET_E	CONV_C		ATM_D	NET_D		NET_D	MLT_D
7.0	0.004	7.70787	7.71075	7.69935	3.61201	3.63864	3.60869	4.00044	4.0312	3.95123
			NET_E	CONV_C		ATM_D	RES_E		RES_E	CONV_C
7.0	0.014	7.73059	7.73579	7.71528	3.59645	3.62914	3.56971	3.75476	3.99678	3.71229
			NET_E	MIX_C		ATM_D	CONV_B		CONV_B	CONV_C
8.0	0.0014	7.58563	7.58778	7.57954	3.66581	3.67048	3.63633	4.08246	4.1906	4.07551
			NET_E	CONV_C		ATM_D	NET_D		NET_D	RES_E
8.0	0.004	7.59553	7.59807	7.58824	3.60443	3.63121	3.6017	4.18018	4.20494	4.14946
			NET_E	CONV_C		ATM_D	RES_E		RES_E	CONV_C
8.0	0.014	7.60925	7.61414	7.59367	3.58747	3.62007	3.56238	3.94702	4.17089	3.92876
			NET_E	MIX_C		ATM_D	CONV_B		CONV_B	ATM_D

**Note.** Columns mark mass, initial metal abundance, nuclear age of the reference model, maximal and minimal values of nuclear age for a given mass and Z with corresponding set in the subrow, effective temperature of the reference model, maximal and minimal values of effective temperature for a given mass and Z with corresponding set in the subrow, log of luminosity (log  $L$ ) of the reference model, and maximal and minimal values of log  $L$  for a given mass and Z with corresponding set in the subrow.








**Table 17**Comparison of Physical Quantities (Nuclear Ages, Effective Temperatures, Luminosities; All in Logarithms) of Models 2–8  $M_{\odot}$  with Convective Core Overshooting ( $f = 0.02$ ) at mIS

Mass	Z	log age <sup>ref</sup>	log age <sup>max</sup>	log age <sup>min</sup>	log $T_{\text{eff}}^{\text{ref}}$	log $T_{\text{eff}}^{\text{max}}$	log $T_{\text{eff}}^{\text{min}}$	log $L^{\text{ref}}$	log $L^{\text{max}}$	log $L^{\text{min}}$
2.0	0.0014	...	...	...	...	...	...	...	...	...
2.0	0.004	...	...	...	...	...	...	...	...	...
2.0	0.014	...	...	...	...	...	...	...	...	...
3.0	0.0014	8.47918	8.48844 NET_D	8.46574 ATM_D	3.79483	3.79716 ATM_D	3.79415 NET_D	2.77438	2.79098 NET_D	2.7172 ATM_D
3.0	0.004	...	...	...	...	...	...	...	...	...
3.0	0.014	...	...	...	...	...	...	...	...	...
4.0	0.0014	8.18332	8.19072 NET_D	8.17038 ATM_D	3.77819	3.78033 ATM_D	3.77753 NET_D	3.18208	3.19844 NET_D	3.12971 ATM_D
4.0	0.004	...	...	...	...	...	...	...	...	...
4.0	0.014	...	...	...	...	...	...	...	...	...
5.0	0.0014	7.96648	7.97249 NET_D	7.95556 ATM_D	3.76577	3.76746 ATM_D	3.76521 NET_D	3.48659	3.50018 NET_D	3.44507 ATM_D
5.0	0.004	...	...	...	...	...	...	...	...	...
5.0	0.014	...	...	...	...	...	...	...	...	...
6.0	0.0014	7.8001	7.80504 NET_D	7.79174 ATM_D	3.75557	3.75678 ATM_D	3.75517 NET_D	3.73638	3.74619 NET_D	3.70685 ATM_D
6.0	0.004	...	...	...	...	...	...	...	...	...
6.0	0.014	...	...	...	...	...	...	...	...	...
7.0	0.0014	7.66772	7.67207 NET_D	7.66221 ATM_D	3.74672	3.74748 ATM_D	3.74647 NET_D	3.95332	3.95946 NET_D	3.9348 ATM_D
7.0	0.004	7.6953	7.70096 NET_E	7.68906 ATM_D	3.74693	3.74768 ATM_D	3.74677 RES_E	3.92029	3.92404 RES_E	3.90212 ATM_D
7.0	0.014	...	...	...	...	...	...	...	...	...
8.0	0.0014	7.55939	7.5634 NET_D	7.55658 ATM_D	3.7391	3.73951 ATM_D	3.73889 NET_D	4.14008	4.14513 NET_D	4.12997 ATM_D
8.0	0.004	7.58343	7.58995 NET_E	7.57865 ATM_D	3.73899	3.73959 ATM_D	3.73891 RES_E	4.11256	4.11457 RES_E	4.09799 ATM_D
8.0	0.014	...	...	...	...	...	...	...	...	...

**Note.** Columns mark mass, initial metal abundance, nuclear age of the reference model, maximal and minimal values of nuclear age for a given mass and Z with corresponding set in the subrow, effective temperature of the reference model, maximal and minimal values of effective temperature for a given mass and Z with corresponding set in the subrow, log of luminosity (log  $L$ ) of the reference model, and maximal and minimal values of log  $L$  for a given mass and Z with corresponding set in the subrow.

## ORCID iDs

O. Ziółkowska  <https://orcid.org/0000-0002-0696-2839>  
R. Smolec  <https://orcid.org/0000-0001-7217-4884>  
A. Thoul  <https://orcid.org/0000-0002-8107-118X>  
R. Singh Rathour  <https://orcid.org/0000-0002-7448-4285>  
V. Hodge  <https://orcid.org/0000-0002-3643-0366>

## References

- Alongi, M., Bertelli, G., Bressan, A., & Chiosi, C. 1991, *A&A*, **244**, 95  
Anders, E. H., Jermyn, A. S., Lecoanet, D., & Brown, B. P. 2022a, *ApJ*, **926**, 169  
Anders, E. H., Jermyn, A. S., Lecoanet, D., et al. 2022b, *ApJL*, **928**, L10  
Anderson, R. I., Saio, H., Ekström, S., Georgy, C., & Meynet, G. 2016, *A&A*, **591**, A8  
Angulo, C., Arnould, M., Rayet, M., et al. 1999, *NuPhA*, **656**, 3  
Asplund, M., Grevesse, N., Sauval, A. J., & Scott, P. 2009, *ARA&A*, **47**, 481  
Bailey, J. E., Nagayama, T., Loisel, G. P., et al. 2015, *Natur*, **517**, 56  
Ball, W. H. 2021, *RNAAS*, **5**, 7  
Böhm-Vitense, E. 1958, *ZA*, **46**, 108  
Bono, G., Caputo, F., & Castellani, V. 2006, *MmSAI*, **77**, 207  
Bono, G., Castellani, V., & Marconi, M. 2002, *ApJL*, **565**, L83  
Bressan, A., Marigo, P., Girardi, L., et al. 2012, *MNRAS*, **427**, 127  
Buldgen, G., Eggenberger, P., Noels, A., et al. 2023, *A&A*, **669**, L9  
Buldgen, G., Noels, A., Baturin, V. A., et al. 2024, *A&A*, **681**, A57  
Caputo, F., Bono, G., Fiorentino, G., Marconi, M., & Musella, I. 2005, *ApJ*, **629**, 1021  
Caputo, F., Castellani, V., Chieffi, A., Pulone, L., & Tornambe, A., J. 1989, *ApJ*, **340**, 241  
Cassisi, S., Castellani, V., Degl'Innocenti, S., Piotto, G., & Salaris, M. 2001, *A&A*, **366**, 578  
Cassisi, S., Salaris, M., & Irwin, A. W. 2003, *ApJ*, **588**, 862  
Castelli, F., & Kurucz, R. L. 2003, in *IAU Symp 210, Modelling of Stellar Atmospheres*, ed. N. Piskunov, W. W. Weiss, & D. F. Gray (San Francisco, CA: ASP), A20  
Catelan, M., & Smith, H. A. 2015, in *Pulsating Stars*, ed. M. Catelan & H. A. Smith (Weinheim: Wiley-VCH)  
Choi, J., Dotter, A., Conroy, C., et al. 2016, *ApJ*, **823**, 102  
Christensen-Dalsgaard, J., di Mauro, M. P., Houdek, G., & Pijpers, F. 2009, *A&A*, **494**, 205  
Colgan, J., Kilcrease, D. P., Magee, N. H., et al. 2016, *ApJ*, **817**, 116  
Connelly, J. N., Bizzarro, M., Krot, A. N., et al. 2012, *Sci*, **338**, 651  
Constantino, T., & Baraffe, I. 2018, *A&A*, **618**, A177  
Constantino, T., Campbell, S. W., & Lattanzio, J. C. 2017, *MNRAS*, **472**, 4900  
Constantino, T., Campbell, S. W., Lattanzio, J. C., & van Duijneveldt, A. 2016, *MNRAS*, **456**, 3866  
Cox, J. P., & Giuli, R. T. 1968, *Principles of Stellar Structure* (New York: Gordon and Breach)  
Csörnyei, G., Szabados, L., Molnár, L., et al. 2022, *MNRAS*, **511**, 2125  
Cyburt, R. H., Amthor, A. M., Ferguson, R., et al. 2010, *ApJS*, **189**, 240  
Daszyńska-Daszkiewicz, J., Walczak, P., Pamyatnykh, A., Szewczuk, W., & Niewiadomski, W. 2023a, *ApJL*, **942**, L38  
Daszyńska-Daszkiewicz, J., Walczak, P., Szewczuk, W., & Niewiadomski, W. 2023b, *MNRAS*, **526**, 1951  
Dorman, B., & Rood, R. T. 1993, *ApJ*, **409**, 387  
Dotter, A., Chaboyer, B., Jevremović, D., et al. 2008, *ApJS*, **178**, 89  
Dotter, A., Conroy, C., Cargile, P., & Asplund, M. 2017, *ApJ*, **840**, 99  
Ekström, S., Georgy, C., Eggenberger, P., et al. 2012, *A&A*, **537**, A146

- Espinoza-Arancibia, F., Catelan, M., Hajdu, G., et al. 2022, *MNRAS*, **517**, 1538
- Ferguson, J. W., Alexander, D. R., Allard, F., et al. 2005, *ApJ*, **623**, 585
- Gabriel, M., Noels, A., Montalbán, J., & Miglio, A. 2014, *A&A*, **569**, A63
- Georgy, C., Ekström, S., Granada, A., et al. 2013, *A&A*, **553**, A24
- Grevesse, N., & Noels, A. 1993, in Symp. in Honour of Hubert Reeves' 60th Birthday: Origin and Evolution of the Elements, ed. N. Prantzos, E. Vangioni-Flam, & M. Casse, **15**
- Grevesse, N., & Sauval, A. J. 1998, *SSRv*, **85**, 161
- Guzik, J. A., Farag, E., Ostrowski, J., et al. 2021, in ASP Conf. Ser. 529, RR Lyrae/Cepheid 2019: Frontiers of Classical Pulsators, ed. K. Kinemuchi et al. (San Francisco, CA: ASP), **79**
- Harris, C. R., Millman, K. J., van der Walt, S. J., et al. 2020, *Natur*, **585**, 357
- Hauschildt, P. H., Allard, F., & Baron, E. 1999a, *ApJ*, **512**, 377
- Hauschildt, P. H., Allard, F., Ferguson, J., Baron, E., & Alexander, D. R. 1999b, *ApJ*, **525**, 871
- Heney, L., Vardya, M. S., & Bodenheimer, P. 1965, *ApJ*, **142**, 841
- Herwig, F. 2000, *A&A*, **360**, 952
- Higl, J., & Weiss, A. 2017, *A&A*, **608**, A62
- Hodé, V., Smolec, R., Moskalik, P., Singh Rathour, R., & Ziółkowska, O. 2024, *A&A*, **683**, A233
- Hunter, J. D. 2007, *CSE*, **9**, 90
- Iglesias, C. A. 2015, *MNRAS*, **450**, 2
- Iglesias, C. A., & Rogers, F. J. 1993, *ApJ*, **412**, 752
- Iglesias, C. A., & Rogers, F. J. 1996, *ApJ*, **464**, 943
- Jermyn, A. S., Bauer, E. B., Schwab, J., et al. 2023, *ApJS*, **265**, 15
- Jermyn, A. S., Schwab, J., Bauer, E., Timmes, F. X., & Potekhin, A. Y. 2021, *ApJ*, **913**, 72
- Keller, S. C., & Wood, P. R. 2006, *ApJ*, **642**, 834
- Kervella, P., Thévenin, F., Morel, P., et al. 2004, *A&A*, **413**, 251
- Komatsu, E., Smith, K. M., Dunkley, J., et al. 2011, *ApJS*, **192**, 18
- Krishna Swamy, K. S. 1966, *ApJ*, **145**, 174
- Kunz, R., Fey, M., Jaeger, M., et al. 2002, *ApJ*, **567**, 643
- Magg, E., Bergemann, M., Serenelli, A., et al. 2022, *A&A*, **661**, A140
- Marchant, P. 2019, Kippenhahn plotter for MESA, v1.0.0, Zenodo, doi:10.5281/zenodo.2602098
- Marchant, P. 2020, orlo/mkipp: New updates, v1.1, Zenodo, doi:10.5281/zenodo.4269885
- McKinney, W. 2010, in Proc. 9th Python in Science Conf., ed. S. van der Walt & J. Millman (SciPy), **56**
- Mihalas, D. 1978, *Stellar Atmospheres* (New York: W. H. Freeman)
- Miller, C. L., Neilson, H. R., Evans, N. R., Engle, S. G., & Guinan, E. 2020, *ApJ*, **896**, 128
- Morel, P., Provost, J., Pichon, B., Lebreton, Y., & Thévenin, F. 2010, *A&A*, **520**, A41
- Moskalik, P., & Dziembowski, W. A. 2005, *A&A*, **434**, 1077
- Natale, G., Marconi, M., & Bono, G. 2008, *ApJL*, **674**, L93
- Neilson, H. R., & Blinn, H. 2021, in ASP Conf. Ser. 529, RR Lyrae/Cepheid 2019: Frontiers of Classical Pulsators, ed. K. Kinemuchi et al. (San Francisco, CA: ASP), **72**
- Ostrowski, J., Baran, A. S., Sanjayan, S., & Sahoo, S. K. 2021, *MNRAS*, **503**, 4646
- Paxton, B. 2021, Modules for Experiments in Stellar Astrophysics (MESA), v21.12.1, Zenodo, doi:10.5281/zenodo.5798242
- Paxton, B., Bildsten, L., Dotter, A., et al. 2011, *ApJS*, **192**, 3
- Paxton, B., Cantiello, M., Arras, P., et al. 2013, *ApJS*, **208**, 4
- Paxton, B., Marchant, P., Schwab, J., et al. 2015, *ApJS*, **220**, 15
- Paxton, B., Schwab, J., Bauer, E. B., et al. 2018, *ApJS*, **234**, 34
- Paxton, B., Smolec, R., Schwab, J., et al. 2019, *ApJS*, **243**, 10
- Pietrinferni, A., Hidalgo, S., Cassisi, S., et al. 2021, *ApJ*, **908**, 102
- Pietrzyński, G., Thompson, I. B., Gieren, W., et al. 2010, *Natur*, **468**, 542
- Potekhin, A. Y., & Chabrier, G. 2010, *CoPP*, **50**, 82
- Prša, A., Harmanec, P., Torres, G., et al. 2016, *AJ*, **152**, 41
- Renzini, A., & Fusi Pecci, F. 1988, *ARA&A*, **26**, 199
- Rodríguez-Segovia, N., Hajdu, G., Catelan, M., et al. 2022, *MNRAS*, **509**, 2885
- Rogers, F. J., & Nayfonov, A. 2002, *ApJ*, **576**, 1064
- Sánchez Arias, J. P., Németh, P., de Almeida, E. S. D. G., et al. 2023, *Galax*, **11**, 93
- Sandage, A., & Tammann, G. A. 1969, *ApJ*, **157**, 683
- Saumon, D., Chabrier, G., & van Horn, H. M. 1995, *ApJS*, **99**, 713
- Schaller, G., Schaerer, D., Meynet, G., & Maeder, A. 1992, *A&AS*, **96**, 269
- Serenelli, A. M., Basu, S., Ferguson, J. W., & Asplund, M. 2009, *ApJL*, **705**, L123
- Smolec, R., & Moskalik, P. 2008, *AcA*, **58**, 193
- Soszyński, I. 2024, in IAU Symp. 376, Period–Luminosity Relations in the Local Group of Galaxies, ed. R. de Grijs, P. A. Whitelock, & M. Catelan (Cambridge: Cambridge Univ. Press), **48**
- Southworth, J. 2015, in ASP Conf. Ser. 496, Living Together: Planets, Host Stars and Binaries, ed. S. M. Rucinski, G. Torres, & M. Zejda (San Francisco, CA: ASP), **164**
- Spada, F., Demarque, P., Kim, Y. C., Boyajian, T. S., & Brewer, J. M. 2017, *ApJ*, **838**, 161
- Stassun, K. G., Hebb, L., López-Morales, M., & Prša, A. 2009, in IAU Symp. 258, The Ages of Stars, ed. E. E. Mamajek, D. R. Soderblom, & R. F. G. Wyse (Cambridge: Cambridge Univ. Press), **161**
- Stobie, R. S. 1969, *MNRAS*, **144**, 511
- The pandas development team 2022, pandas-dev/pandas: Pandas v1.4.2, Zenodo, doi:10.5281/zenodo.6408044
- Timmes, F. X., & Swesty, F. D. 2000, *ApJS*, **126**, 501
- Tognelli, E., Prada Moroni, P. G., & Degl'Innocenti, S. 2011, *A&A*, **533**, A109
- Townsend, R. 2022, MESA SDK for Linux, v22.6.1, Zenodo, doi:10.5281/zenodo.7457681
- Trampedach, R., Stein, R. F., Christensen-Dalsgaard, J., Nordlund, Å., & Asplund, M. 2014, *MNRAS*, **442**, 805
- Ułaczyk, K., Szymański, M. K., Udalski, A., et al. 2013, *AcA*, **63**, 159
- Valle, G., Dell'Omodarme, M., Prada Moroni, P. G., & Degl'Innocenti, S. 2018, *A&A*, **615**, A62
- VandenBerg, D. A., Bergbusch, P. A., & Dowler, P. D., 2014 Victoria Regina Models: Stellar Evolutionary Tracks, Astrophysics Source Code Library, ascl:1404.010
- Weiss, A., Serenelli, A., Kitsikis, A., Schlattl, H., & Christensen-Dalsgaard, J. 2005, *A&A*, **441**, 1129
- Wolf, B., & Schwab, J. 2017, wmwolf/py\_mesa\_reader: Interact with MESA Output, v0.3.0, Zenodo, doi:10.5281/zenodo.826958
- Wood, P. R., Arnold, S., & Sebo, K. M. A. 1997, *ApJL*, **485**, L25
- Xu, Y., Takahashi, K., Goriely, S., et al. 2013, *NuPhA*, **918**, 61
- Yoon, S. C., & Langer, N. 2005, *A&A*, **435**, 967